Eur. Phys. J. C manuscript No.
(will be inserted by the editor)

Higgs Physics at the CLIC Electron-Positron Linear Collider

H. Abramowicz[24], A. Abusleme[22], K. Afanaciev[20], G. Alexander[24], N. Alipour Tehrani[9], C. Balázs[2], Y. Benhammou[24], M. Benoit[10], B. Bilki[4], J.-J. Blaising[16], M. Boland[2], M. Boronat[23,29], O. Borysov[24], I. Božović-Jelisavčić[25], M. Buckland[17], P. Burrows[21], T. Charles[2], W. Daniluk[12], D. Dannheim[9], M. Demarteau[4], M.A. Díaz[22], G. Eigen[5], K. Elsener[9], U. Felzmann[2], M. Firlej[3], E. Firu[14], T. Fiutowski[3], T. Frisson[9], J. Fuster[23,29], M. Gabriel[19], F. Gaede[9,26], I. García[23,29], V. Ghenescu[14], J. Goldstein[7], S. Green[8], C. Grefe[9,⋆], M. Hauschild[9], C. Hawkes[6], M. Idzik[3], G. Kačarević[25], S. Kananov[24], W. Klempt[9], B. Krupa[12], S. Kulis[9], T. Laštovička[13], T. Lesiak[12], A. Levy[24], I. Levy[24], L. Linssen[9], S. Lukić[25,⋆], V. Makarenko[20], J. Marshall[8], K. Mei[8], G. Milutinović-Dumbelović[25], J. Moroń[3], A. Moszczyński[12], D. Moya[23,28], A. Münnich[9], A.T. Neagu[14], N. Nikiforou[9], K. Nikolopoulos[6], M. Pandurović[25], B. Pawlik[12], I. Peric[15], M. Petric[9], S.G. Poss[9], T. Preda[14], D. Protopopescu[11], R. Rassool[2], S. Redford[9,⋆], J. Repond[4], A. Robson[11], P. Roloff[9,⋆], E. Ros[23,29], O. Rosenblat[24], A. Ruiz-Jimeno[23,28], A. Sailer[9], W.-D. Schlatter[9], D. Schulte[9], N. Shumeiko[20], E. Sicking[9], F. Simon[19,⋆], R. Simoniello[9], P. Sopicki[12], S. Stapnes[9], J. Strube[9], K.P. Świentek[3], M. Szalay[19], M. Tesař[19], M. Thomson[8,⋆], J. Trenado[23,27], U.I. Uggerhøj[1], N. van der Kolk[19], E. van der Kraaij[5], I. Vila[23,28], M.A. Vogel Gonzalez[22], M. Vos[23,29], J. Vossebeld[17], M. Watson[6], N. Watson[6], H. Weerts[4], J. Wells[18], L. Weuste[19], A. Winter[6], T. Wojtoń[12], L. Xia[4], B. Xu[8], L. Zawiejski[12], I.-S. Zgura[14]

[1]Aarhus University, Aarhus, Denmark
[2]Australian Collaboration for Accelerator Science (ACAS)
[3]Faculty of Physics and Applied Computer Science, AGH University of Science and Technology, Cracow, Poland
[4]Argonne National Laboratory, Argonne, USA
[5]Department of Physics and Technology, University of Bergen, Bergen, Norway
[6]School of Physics and Astronomy, University of Birmingham, United Kingdom
[7]University of Bristol, Bristol, United Kingdom
[8]University of Cambridge, Cambridge, United Kingdom
[9]CERN, Geneva, Switzerland
[10]Département de Physique Nucléaire et Corpusculaire (DPNC), Université de GenÃšve, Geneva, Switzerland
[11]University of Glasgow, Glasgow, United Kingdom
[12]The Henryk Niewodniczański Institute of Nuclear Physics Polish Academy of Sciences , Cracow, Poland
[13]Institute of Physics of the Academy of Sciences of the Czech Republic, Prague, Czech Republic
[14]Institute of Space Science, Bucharest, Romania
[15]Karlsruher Institut für Technologie (KIT), Institut für Prozessdatenverarbeitung und Elektronik (IPE), Karlsruhe, Germany
[16]Laboratoire d'Annecy-le-Vieux de Physique des Particules, Annecy-le-Vieux, France
[17]University of Liverpool, Liverpool, United Kingdom
[18]Physics Department, University of Michigan, Ann Arbor, Michigan, USA
[19]Max-Planck-Institut für Physik, Munich, Germany
[20]National Scientific and Educational Centre of Particle and High Energy Physics, Belarusian State University, Minsk, Belarus
[21]Oxford University, Oxford, United Kingdom
[22]Pontificia Universidad Católica de Chile, Santiago, Chile
[23]Spanish Network for Future Linear Colliders
[24]Raymond & Beverly Sackler School of Physics & Astronomy, Tel Aviv University, Tel Aviv, Israel
[25]Vinča Institute of Nuclear Sciences, University of Belgrade, Belgrade, Serbia
[26]DESY, Hamburg, Germany
[27]University of Barcelona, Barcelona, Spain
[28]IFCA, CSIC-University of Cantabria, Santander, Spain
[29]IFIC, CSIC-University of Valencia, Valencia, Spain

Received: date / Accepted: date

Abstract The Compact Linear Collider (CLIC) is an option for a future e^+e^- collider operating at centre-of-mass energies up to 3 TeV, providing sensitivity to a wide range of new physics phenomena and precision physics measurements at the energy frontier. This paper presents the Higgs physics reach of CLIC operating in three energy stages, $\sqrt{s}$ = 350 GeV, 1.4 TeV and 3 TeV. The initial stage of operation allows the study of Higgsstrahlung ($e^+e^- \to HZ$) and WW-fusion ($e^+e^- \to H\nu_e\bar{\nu}_e$), resulting in precise measurements of $\sigma(HZ)$, the Higgs total decay width Γ_H, and model-independent determinations of the Higgs couplings. Operation at $\sqrt{s} >$ 1 TeV provides high-statistics samples of Higgs bosons produced through WW-fusion, providing tight constraints on the Higgs boson couplings. Studies of the rarer processes $e^+e^- \to t\bar{t}H$ and $e^+e^- \to HH\nu_e\bar{\nu}_e$ would provide measurements of the top Yukawa coupling and the Higgs boson self-coupling. This paper presents detailed studies of the precision achievable with Higgs measurements at CLIC and describes the interpretation of these measurements in a global fit.

1 Introduction

The discovery of a 126 GeV Higgs boson [1, 2] at the LHC provided confirmation of the electroweak symmetry breaking mechanism [3–8] of the Standard Model (SM). However, it is not yet known if the observed Higgs boson is the fundamental singlet scalar of the SM or is either a more complex object or part of an extended Higgs sector. Precise studies of the properties of the Higgs boson at the LHC and future colliders are essential to understand its true nature.

The Compact Linear Collider (CLIC) is a TeV-scale high-luminosity linear e^+e^- collider that is currently under development at CERN. It is based on a novel two-beam acceleration technique providing accelerating gradients of 100 MV/m. Recent implementation studies for CLIC have converged towards a staged approach offering a unique physics programme spanning several decades. In this scheme, CLIC would provide high-luminosity e^+e^- collisions from a few hundred GeV to 3 TeV. The nominal centre-of-mass energy of the first energy stage is chosen to be $\sqrt{s}$ = 350 GeV. At this centre-of-mass energy, the Higgsstrahlung and WW-fusion processes have significant cross sections, giving access to precise measurement of absolute values of Higgs couplings to both fermions and bosons. Another advantage of operating the first stage of CLIC at $\sqrt{s} \sim 350$ GeV is that it enables a programme of precision top quark physics, including a scan of the $t\bar{t}$ cross section close to the production threshold. In practice, the centre-of-mass energy of the second stage of CLIC operation would be motivated by both the machine design and the results from the LHC. Here it is assumed that the second CLIC energy stage has $\sqrt{s} = 1.4$ TeV and that the ultimate CLIC centre-of-mass energy is 3 TeV. In addition to direct and indirect searches for Beyond the Standard Model (BSM) phenomena, these higher energy stages of operation provide a rich potential for Higgs physics beyond that accessible at lower energies, such as the direct measurement of the top Yukawa coupling and a direct probe of the Higgs potential through the measurement of the Higgs self-coupling λ. Furthermore, rare Higgs boson decays become accessible due to the higher integrated luminosities at higher energies and the increasing cross section for Higgs production in WW-fusion.

*Corresponding Editors: clicdp-higgs-paper-editors@cern.ch

The following sections describe: the experimental conditions at CLIC; an overview of Higgs production at CLIC; the Monte Carlo samples, detector simulation and event reconstruction used for the subsequent studies; Higgs production at $\sqrt{s}$ = 350 GeV; Higgs production in WW-fusion at $\sqrt{s} >$ 1 TeV; Higgs production in ZZ-fusion; the measurement of the top Yukawa coupling; double Higgs production; measurements of the Higgs boson mass; and conclude with a discussion of the resulting measurement precisions on the Higgs couplings obtained in a combined fit to the foreseen CLIC results.

2 Experimental Environment at CLIC

The experimental environment at CLIC is characterised by challenging conditions imposed by the CLIC accelerator technology, by detector concepts optimised for the precise reconstruction of complex final states in the multi-TeV region in an environment with high beam-induced background levels and by the operation in several energy stages to maximise the physics potential.

2.1 Accelerator and Beam Conditions

The CLIC accelerator design is based on a two-beam acceleration scheme. It uses a high-intensity drive beam to efficiently generate radio frequency (RF) power at 12 GHz. The RF power is used to accelerate the main particle beam that runs parallel to the drive beam. CLIC uses normal-conducting accelerator structures, operated at room temperature. These structures permit high accelerating gradients, while the short pulse duration discussed below limits ohmic losses to tolerable levels. The initial drive beams and the main electron/positron beams are generated in the central complex and are then injected at the ends of the two linac arms. The feasibility of the CLIC accelerator has been demonstrated through prototyping, simulations and large-scale tests, as described in the Conceptual Design Report [9]. In particular, the two-beam acceleration at gradients exceeding 100 MV/m has been demonstrated in the CLIC test facility, CTF3. High luminosities are achieved by very small beam emittances, which are generated in the injector complex and maintained during transport to the interaction point.

CLIC is operated with bunch trains with a repetition rate of 50 Hz. Each bunch train consists of 312 individual bunches, with 0.5 ns between bunch crossings at the interaction point. The average number of hard interactions (i.e. high $|q^2|$) in a single bunch train crossing is much less than one, where q is the four-momentum scale of the interaction. However, for CLIC operation at $\sqrt{s} > 1\,\text{TeV}$, the highly-focussed intense beams lead to significant beamstrahlung (radiation of photons from electrons/positrons in the electric field of the other beam). Beamstrahlung results in high rates of incoherent electron–positron pairs and low-Q^2 t-channel multi-peripheral $\gamma\gamma \to$ hadron events, where Q is the negative of the four-momentum of the virtual space-like photon. In addition, the energy loss through beamstrahlung generates a long lower-energy tail to the luminosity spectrum that extends well below the nominal centre-of-mass energy. Both the CLIC detector design and the event reconstruction techniques employed are optimised to mitigate the influence of these backgrounds, which are most severe at the higher CLIC energies.

The baseline machine design allows for up to $\pm 80\,\%$ electron polarisation, but no positron polarisation. Most studies presented in this paper are performed for zero beam polarisation and are subsequently scaled to account for the increased cross sections with left-handed polarisation for the electron beam.

2.2 Detectors at CLIC

The detector concepts used for the CLIC physics studies, described here and elsewhere, are based on the SiD [10, 11] and ILD [11, 12] detector concepts for the International Linear Collider (ILC). They were initially adapted for the CLIC 3 TeV operation, which constitutes the most challenging environment for the detectors. For most sub-detector systems, the 3 TeV detector design is suitable at all energy stages. The only exception being the inner tracking detectors and the vertex detector, where the lower backgrounds at $\sqrt{s} = 350\,\text{GeV}$ enable detectors to be deployed with a smaller inner radius.

The key performance parameters of the CLIC detector concepts with respect to the Higgs programme are:

– excellent track-momentum resolution, required for a precise reconstruction of leptonic Z decays in HZ events;
– precise impact parameter resolution to provide accurate vertex reconstruction, enabling flavour-tagging with clean b-, c- and light-quark jet separation;
– jet-energy resolution $\sigma_E/E \lesssim 3.5\%$ for jet energies in the range 100 GeV to 1 TeV, required for the reconstruction of hadronic Z decays in HZ events and the separation of $\mathrm{W} \to \mathrm{q}\overline{\mathrm{q}}$, $\mathrm{Z} \to \mathrm{q}\overline{\mathrm{q}}$ and $\mathrm{H} \to \mathrm{q}\overline{\mathrm{q}}$ based on the reconstructed di-jet invariant mass;
– detector coverage for electrons extending to very low angles with respect to the beam axis, to maximise background rejection for WW-fusion events.

The main design driver for the CLIC (and ILC) detector concepts is the required jet-energy resolution. As a result, the CLIC detector concepts [13], CLIC_SiD and CLIC_ILD, are based on fine-grained electromagnetic and hadronic calorimeters (ECAL and HCAL), optimised for particle-flow analysis techniques. In the particle-flow approach, the aim is to reconstruct the individual final-state visible particles within a jet using information from the tracking chambers combined with that from the highly granular calorimeters [14, 15]. In addition, particle-flow event reconstruction provides a powerful tool for the rejection of beam-induced backgrounds [13]. The CLIC detector concepts employ strong central solenoid magnets, located outside the HCAL, providing an axial magnetic field of 5 T in CLIC_SiD and 4 T in CLIC_ILD. The CLIC_SiD concept employs central silicon-strip tracking detectors, whereas CLIC_ILD assumes a large central gaseous Time Projection Chamber. In both concepts, the central tracking system is augmented with silicon-pixel and silicon-strip based inner tracking detectors. The two detector concepts are shown schematically in Figure 1 and are described in detail in [13].

2.3 Assumed Staged Running Scenario

The studies presented in this paper are based on a particular staging scenario for CLIC, which assumes a three-stage implementation. The first stage provides a centre-of-mass energy above 350 GeV to reach the top-pair production threshold. The second stage extends up to $\sqrt{s} = 1.4\,\text{TeV}$. This was chosen because it is the energy that can be reached with a single CLIC drive-beam complex. The third stage reaches $\sqrt{s} = 3\,\text{TeV}$, the ultimate energy of CLIC. At each stage, four to five years of running with a fully commissioned machine are foreseen, providing integrated luminosities of $500\,\text{fb}^{-1}$, $1.5\,\text{ab}^{-1}$ and $2\,\text{ab}^{-1}$ at 350 GeV, 1.4 TeV and 3 TeV, respectively.

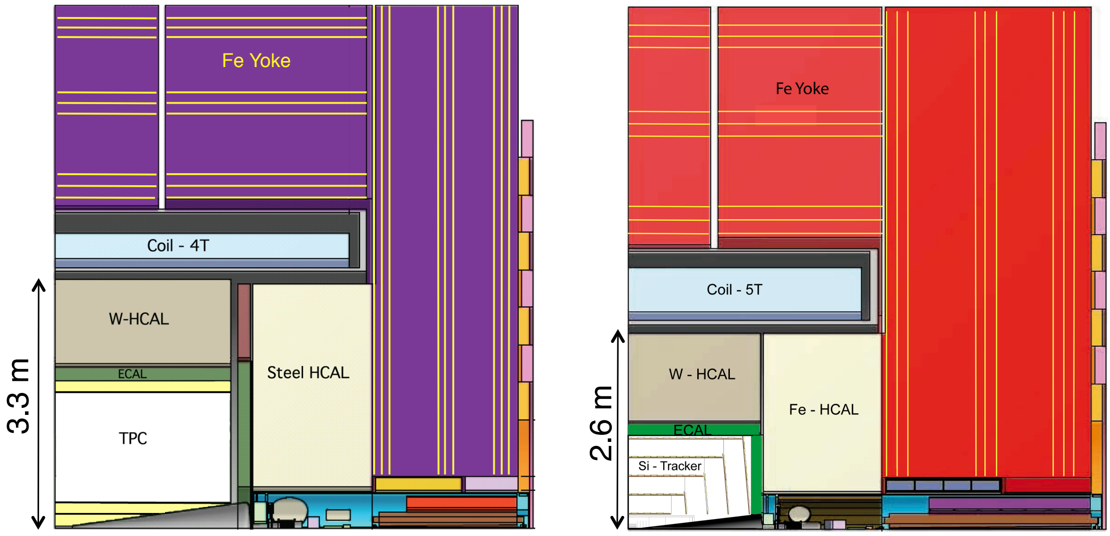

Fig. 1: Longitudinal cross section (to scale) of the top right quadrant of the CLIC_ILD (left) and CLIC_SiD (right) detector concepts for CLIC.

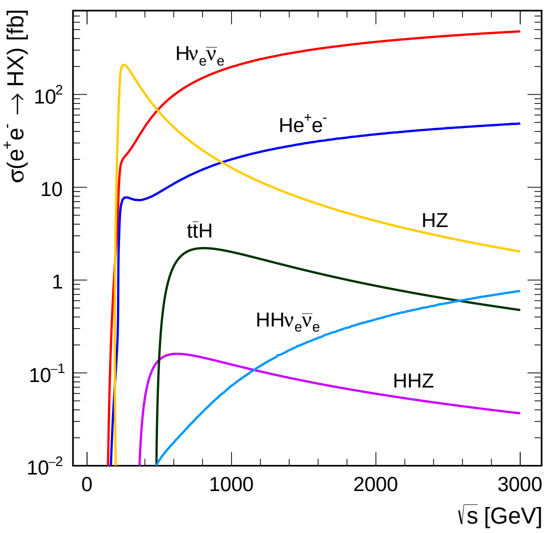

Fig. 2: The centre-of-mass dependencies of the cross sections for the main Higgs production processes at an e^+e^- collider for $m_H = 126\,\text{GeV}$. The values shown correspond to unpolarised beams and do not include the effect of beamstrahlung.

3 Overview of Higgs Production at CLIC

A high-energy e^+e^- collider, such as CLIC (or the ILC), provides a clean experimental environment to study the properties of the Higgs boson with high precision. The evolution of the leading-order e^+e^- Higgs production cross sections with centre-of-mass energy is shown in Figure 2 for a Higgs boson mass of 126 GeV.

The Feynman diagrams for the three highest cross section Higgs production processes at CLIC are shown in Figure 3. In the initial stage of CLIC operation at $\sqrt{s} \approx 350\,\text{GeV}$, the Higgsstrahlung process ($e^+e^- \to ZH$) has the largest cross section, but the WW-fusion process ($e^+e^- \to H\nu_e\bar{\nu}_e$) is also significant. The combined study of these *two* processes probes the Higgs boson properties (width and branching ratios) in a *model-independent* manner. In the higher energy stages of CLIC operation ($\sqrt{s} = 1.4\,\text{TeV}$ and 3 TeV), Higgs production is dominated by the WW-fusion process, with the ZZ-fusion process ($e^+e^- \to He^+e^-$) also becoming significant. Here the relatively large WW-fusion cross section, combined with the high luminosity of CLIC, results in large data samples, allowing precise $\mathcal{O}(1\,\%)$ measurements of the couplings of the Higgs boson to both fermions and gauge bosons. In addition to the main Higgs production processes, rarer processes such as $e^+e^- \to t\bar{t}H$ and $e^+e^- \to HH\nu_e\bar{\nu}_e$, shown in Figure 4, provide access to the top Yukawa coupling and the Higgs trilinear self-coupling as determined by the parameter λ in the Higgs potential. In all cases, the Higgs production cross sections can be increased with polarised electron (and positron) beams.

Table 1 compares the expected numbers of ZH, $H\nu_e\bar{\nu}_e$ and He^+e^- events for the three main CLIC centre-of-mass energy stages. These numbers account for the effect of beamstrahlung and initial state radiation (ISR), which result in a tail in the distribution of the effective centre-of-mass energy $\sqrt{s'}$. The impact of beamstrahlung on the expected numbers of events is relatively small. For example, it results in an approximately 10 % reduction in the numbers of $H\nu_e\bar{\nu}_e$ events at $\sqrt{s} > 1\,\text{TeV}$ (compared to the beam spectrum with ISR

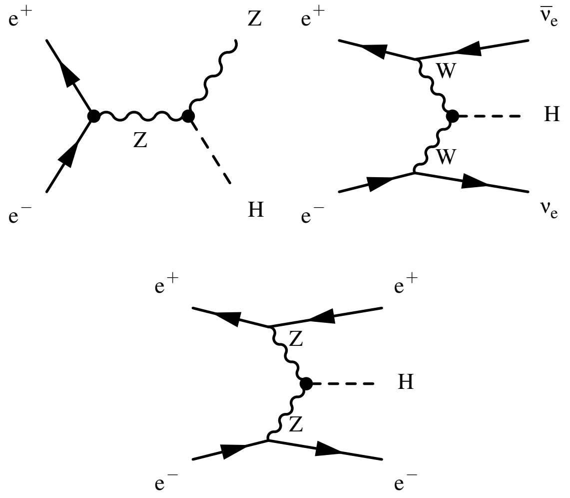

Fig. 3: The three highest cross section Higgs production processes at CLIC.

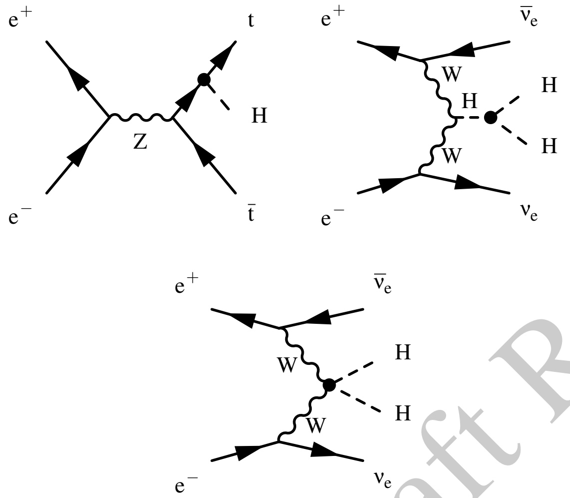

Fig. 4: The main processes at CLIC involving the top Yukawa coupling g_{Htt}, the Higgs boson trilinear self-coupling λ and the quartic coupling g_{HHWW}.

alone), because the cross section rises relatively slowly with $\sqrt{s}$.

The polar angle distributions for single Higgs production for the CLIC centre-of-mass energies are shown in Figure 5. Most Higgs bosons produced at 350 GeV can be reconstructed in the central parts of the detectors while good capabilities of the detectors in the forward regions are crucial at 1.4 and 3 TeV.

A SM Higgs boson with mass of $m_{\mathrm{H}} = 126\,\mathrm{GeV}$ has a wide range of decay modes, as listed in Table 2, providing the possibility to test the SM predictions for the couplings of the Higgs to both gauge bosons and to fermions[16]. All the modes listed in Table 2 are accessible at CLIC.

$\sqrt{s} =$	350 GeV	1.4 TeV	3 TeV
$\mathscr{L}_{\mathrm{int}}$	500 fb^{-1}	1.5 ab^{-1}	2 ab^{-1}
$\sigma(\mathrm{e}^+\mathrm{e}^- \to \mathrm{ZH})$	133 fb	8 fb	2 fb
$\sigma(\mathrm{e}^+\mathrm{e}^- \to \mathrm{H}\nu_\mathrm{e}\bar{\nu}_\mathrm{e})$	34 fb	276 fb	477 fb
$\sigma(\mathrm{e}^+\mathrm{e}^- \to \mathrm{He}^+\mathrm{e}^-)$	7 fb	28 fb	48 fb
# ZH events	68,000	20,000	11,000
# $\mathrm{H}\nu_\mathrm{e}\bar{\nu}_\mathrm{e}$ events	17,000	370,000	830,000
# $\mathrm{He}^+\mathrm{e}^-$ events	3,700	37,000	84,000

Table 1: The leading-order Higgs *unpolarised* cross sections for the Higgsstrahlung, WW-fusion, and ZZ-fusion processes for $m_{\mathrm{H}} = 126\,\mathrm{GeV}$ at the three centre-of-mass energies discussed in this document. The quoted cross sections include the effects of ISR but do not include the effects of beamstrahlung. Also listed are the numbers of expected events *including* the effects of the CLIC beamstrahlung spectrum and ISR. The cross sections and expected numbers do not account for the possible enhancements from polarised beams.

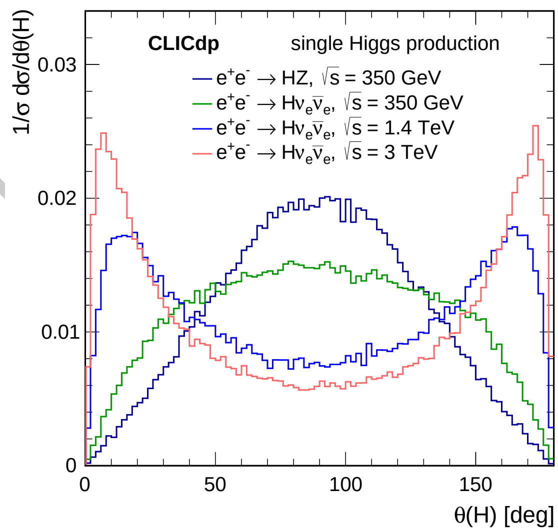

Fig. 5: Polar angle distributions for single Higgs production at various centre-of-mass energies. All distributions include the effects of the CLIC beamstrahlung spectrum and ISR. All distributions are normalised to unity.

3.1 Motivation for $\sqrt{s} = 350\,\mathrm{GeV}$ CLIC Operation

The choice of the CLIC energy stages is motivated by the desire to pursue a programme of precision Higgs physics and to operate the machine above 1 TeV at the earliest possible time; no CLIC operation is foreseen below the top-pair production threshold. From the perspective of Higgs physics, lower-energy operation is partly motivated by the *direct* and *model-independent* measurement of the coupling of the Higgs boson to the Z, which can be obtained from the

Decay mode	Branching ratio
$H \to b\bar{b}$	56.1 %
$H \to WW^*$	23.1 %
$H \to gg$	8.5 %
$H \to \tau^+\tau^-$	6.2 %
$H \to c\bar{c}$	2.8 %
$H \to ZZ^*$	2.9 %
$H \to \gamma\gamma$	0.23 %
$H \to Z\gamma$	0.16 %
$H \to \mu^+\mu^-$	0.021 %
Γ_H	4.2 MeV

Table 2: The largest SM Higgs decay modes and branching ratios for $m_H = 126\,\text{GeV}$.

Polarisation	Enhancement factor		
$P(e^-) : P(e^+)$	$e^+e^- \to ZH$	$e^+e^- \to H\nu_e\bar{\nu}_e$	$e^+e^- \to Ze^+e^-$
unpolarised	1.00	1.00	1.00
$-80\% : \quad 0\%$	1.12	1.80	1.12
$-80\% : +30\%$	1.40	2.34	1.17
$-80\% : -30\%$	0.83	1.26	1.07
$+80\% : \quad 0\%$	0.88	0.20	0.88
$+80\% : +30\%$	0.69	0.26	0.92
$+80\% : -30\%$	1.08	0.14	0.84

Table 3: The dependence of the event rates for the *s*-channel $e^+e^- \to ZH$ process and the pure *t*-channel $e^+e^- \to H\nu_e\bar{\nu}_e$ and $e^+e^- \to Ze^+e^-$ processes for three example beam polarisations. The scale factors assume an effective weak mixing angle given by $\sin^2\theta_W^{eff} = 0.23146$. The numbers are only approximate as they do not account for interference between $e^+e^- \to HZ \to H\nu_e\bar{\nu}_e$ and $e^+e^- \to H\nu_e\bar{\nu}_e$.

recoil mass distribution in $HZ \to He^+e^-$, $HZ \to H\mu^+\mu^-$ and $HZ \to Hq\bar{q}$ production (see Sections 5.1.1 and 5.1.3). These measurements play a central role in the determination of the Higgs couplings at a linear collider. Thus, it might seem surprising that no significant CLIC running is considered at $\sqrt{s} = 250$ GeV, which is close to the maximum of the Higgsstrahlung cross section (see Section 2). There are three reasons why 250 GeV operation is not considered a priority. Firstly, the reduction in cross section in going to $\sqrt{s} = 350\,\text{GeV}$ is, in part, compensated by the increased instantaneous luminosity achievable at a higher centre-of-mass energy; the instantaneous luminosity scales approximately linearly with the centre-of-mass energy, $\mathscr{L} \propto \gamma_e$, where γ_e is the Lorentz factor for the beam electrons/positrons. For this reason the precision on the coupling g_{HZZ} at 350 GeV is comparable to that achievable at 250 GeV for the same period of operation. Secondly, the additional boost of the Z and H at $\sqrt{s} = 350\,\text{GeV}$ provides greater separation between the final-state jets from Z and H decays. Consequently, the measurements of $\sigma(HZ) \times BR(H \to X)$ can be more precise at $\sqrt{s} = 350\,\text{GeV}$. Thirdly, and most importantly, measurements of the Higgsstrahlung cross section alone are not sufficient to provide truly model-independent measurements of the Higgs boson couplings; knowledge of the total decay width Γ_H is also required. This can be inferred from the measurements of the cross sections for the WW-fusion processes. Initial operation of CLIC at $\sqrt{s} \approx 350\,\text{GeV}$, where the $e^+e^- \to H\nu_e\bar{\nu}_e$ fusion cross section is significant, provides constraints on the Higgs coupling to the W boson and, by inference, provides a determination of the Higgs width Γ_H. For the above reasons, the preferred option for the first stage of CLIC operation is $\sqrt{s} \approx 350$ GeV and operation at $\sqrt{s} \sim 250$ GeV is not foreseen. Furthermore, at $\sqrt{s} \approx 350$ GeV, detailed studies of the top-pair production process can be performed in the initial stage of CLIC operation. Finally, it is worth noting that a similar Higgs boson mass precision can be obtained from the recoil mass distribution in $HZ \to H\mu^+\mu^-$ at $\sqrt{s} = 250\,\text{GeV}$ or from the direct reconstruction of the Higgs decay products in, for example, $H \to q\bar{q}$ decays at $\sqrt{s} = 350\,\text{GeV}$ and higher.

3.2 Impact of Beam Polarisation

The majority of CLIC Higgs physics studies have been performed assuming unpolarised e^+ and e^- beams. However, for the baseline CLIC design, the electron beam can be polarised up to ±80 %. There is the possibility of positron polarisation at a lower level, although this is not in the baseline CLIC machine design. For an electron polarisation of P_- and positron polarisation of P_+, the relative fractions of collisions in the different helicity states are

$$e^-_R e^+_R : \tfrac{1}{4}(1+P_-)(1+P_+) \; , \; e^-_R e^+_L : \tfrac{1}{4}(1+P_-)(1-P_+)$$
$$e^-_L e^+_R : \tfrac{1}{4}(1-P_-)(1+P_+) \; , \; e^-_L e^+_L : \tfrac{1}{4}(1-P_-)(1-P_+) \, .$$

By selecting different beam polarisations it is possible to enhance/suppress different physical processes. The chiral nature of the weak coupling to fermions results in significant possible enhancements in WW-fusion Higgs production, as indicated in Table 3. The potential gains for the *s*-channel Higgsstrahlung process, $e^+e^- \to ZH$, are less significant, and the $e^+e^- \to He^+e^-$ cross section dependence on the polarisation is even smaller. In practice, the balance between operation with different beam polarisations will depend on the CLIC physics programme taken as a whole, including the searches for and potential measurements of BSM particle production.

3.3 Overview of Higgs Measurements at $\sqrt{s} = 350$ GeV

The Higgsstrahlung process provides the opportunity to study the couplings of the Higgs boson in a *model-independent* manner. This is unique to an electron-positron collider. The clean experimental environment, and the relatively low SM cross sections for background processes, allow $e^+e^- \to ZH$ events to be selected based solely on the measurement of the four-momentum of the Z through its decay products. The most distinct event topologies occur for $Z \to e^+e^-$ and $Z \to \mu^+\mu^-$ decays, which can be identified by requiring that the di-lepton invariant mass is consistent with m_Z. The four-momentum of the system recoiling against the Z can be obtained from $E_{rec} = \sqrt{s} - E_Z$ and $\mathbf{p}_{rec} = -\mathbf{p}_Z$. In $e^+e^- \to ZH$ events, the invariant mass of this recoiling system will peak at m_H, allowing the ZH events to be selected based only on the observation of the leptons from the Z decay, providing a model-independent measurement of the Higgs coupling to the Z boson (see Section 5.1.1). A slightly less clean, but more precise, measurement is obtained from the recoil mass analysis for $Z \to q\overline{q}$ decays (see Section 5.1.3). The recoil-mass studies provide an absolute measurement of the total ZH production cross section and a model-independent measurement of the coupling of the Higgs to the Z boson, g_{HZZ}. The combination of the leptonic and hadronic decay channels allows g_{HZZ} to be determined with a precision of 0.8 %. In addition, the recoil mass from $Z \to q\overline{q}$ decays provides a direct search for possible Higgs decays to invisible final states, and can be used to constrain the invisible decay width of the Higgs, Γ_{invis}.

By identifying the individual final states for different Higgs decay modes, precise measurements of the Higgs boson branching fractions can be made. Because of the high flavour-tagging efficiencies [13] achievable at CLIC, the $H \to b\overline{b}$ and $H \to c\overline{c}$ decays can be cleanly separated. Neglecting the Higgs decays into light quarks, the branching ratio of $H \to gg$ can also be inferred and $H \to \tau^+\tau^-$ decays can be identified.

Although the cross section is lower, the t-channel WW-fusion process $e^+e^- \to H\nu_e\overline{\nu}_e$ is an important part of the CLIC Higgs physics programme at $\sqrt{s} \approx 350$ GeV. Because the final state consists of the Higgs boson decay products alone, the direct reconstruction of the invariant mass of the Higgs boson or, in the case of $H \to WW^*$, its decay products, plays a central role in the event selection. The combination of Higgs production and decay data from Higgsstrahlung and WW-fusion processes provides a model-independent extraction of Higgs couplings.

3.3.1 Extraction of Higgs Couplings

At the LHC, only *relative* measurements of the couplings of the Higgs boson can be inferred from the data. At an electron-positron collider *absolute* measurements of the couplings can be determined using the total $e^+e^- \to ZH$ cross section from the recoil mass analyses. This allows the coupling of the Higgs boson to the Z to be determined with a precision of better than 1 % in an essentially model-independent manner. Once the coupling to the Z is known, the Higgs coupling to the W can be determined from, for example, the ratios of Higgsstrahlung to WW-fusion cross sections,

$$\frac{\sigma(e^+e^- \to ZH) \times BR(H \to b\overline{b})}{\sigma(e^+e^- \to \nu_e\overline{\nu}_e H) \times BR(H \to b\overline{b})} \propto \left(\frac{g_{HZZ}}{g_{HWW}}\right)^2 .$$

In order to determine absolute measurements of the other Higgs couplings, the Higgs total decay width needs to be inferred from the data. For a Higgs boson mass of around 126 GeV, the total Higgs decay width in the SM (Γ_H) is less than 5 MeV and cannot be measured directly. However, given that the absolute couplings of the Higgs boson to the Z and W can be obtained as described above, the total decay width of the Higgs boson can be determined from $H \to WW^*$ or $H \to ZZ^*$ decays. For example, the measurement of the Higgs decay to WW^* in the WW-fusion process determines

$$\sigma(H\nu_e\overline{\nu}_e) \times BR(H \to WW^*) \propto \frac{g^4_{HWW}}{\Gamma_H} ,$$

and thus the total width can be determined utilising the model-independent measurement of g_{HWW}. In practice, a fit (see Section 11) is performed to all of the experimental measurements involving the Higgs boson couplings.

3.4 Overview of Higgs Measurements at $\sqrt{s} > 1$ TeV

For CLIC operation above 1 TeV, the large numbers of Higgs bosons produced in the WW-fusion process allow relative couplings of the Higgs boson to the W and Z bosons to be determined at the $\mathcal{O}(1\,\%)$ level. These measurements provide a strong test of the SM prediction for $g_{HWW}/g_{HZZ} = \cos^2\theta_W$, where θ_W is the weak-mixing angle. Furthermore, the exclusive Higgs decay modes can be studied with significantly higher precision than at $\sqrt{s} = 350$ GeV. For example, CLIC operating at 3 TeV would yield a statistical precision of 1.5 % on the ratio g_{Hcc}/g_{Hbb}, providing a direct comparison of the SM coupling predictions for up-type (charge $+2/3$) and down-type (charge $-1/3$) quarks. In the context of the model-independent measurements of the Higgs branching ratios, the measurement of $\sigma(\mathrm{H}\nu_e\bar{\nu}_e) \times BR(\mathrm{H} \to \mathrm{WW}^*)$ is particularly important. For CLIC operation at $\sqrt{s} \approx 1.4$ TeV, the large number of events allows this cross section to be determined with a precision of 1.5 % (see Section 6.3). When combined with the measurements at $\sqrt{s} \approx 350$ GeV, this places strong constraints on Γ_H.

Although the WW-fusion process has the largest cross section for Higgs production above 1 TeV, other processes are also important. For example, measurements of the ZZ-fusion process provide further constraints on the g_{HZZ} coupling. Furthermore, CLIC operation at $\sqrt{s} = 1.4$ TeV enables a determination of the top Yukawa coupling from the process $\mathrm{e}^+\mathrm{e}^- \to \mathrm{t\bar{t}H} \to \mathrm{bW^+\bar{b}W^-H}$ with a precision of 4.5 % (see Section 8). Finally, the self-coupling of the Higgs boson at the HHH vertex is measurable in 1.4 TeV and 3 TeV operation. In the SM, the Higgs boson originates from a doublet of complex scalar fields ϕ described by the potential

$$V(\phi) = \mu^2\phi^\dagger\phi + \lambda(\phi^\dagger\phi)^2,$$

where μ and λ are the parameters of the Higgs potential. After spontaneous symmetry breaking, this form of the potential gives rise to a trilinear Higgs self-coupling of strength proportional to λv, where v is the vacuum expectation value of the Higgs potential. The measurement of the strength of the Higgs self-coupling therefore provides direct access to the coupling λ assumed in the Higgs mechanism. This measurement is an essential part of experimentally establishing the Higgs mechanism as described by the SM. For $m_\mathrm{H} = 126$ GeV, the measurement of the Higgs boson self-coupling at the LHC will be extremely challenging even with 3000 fb^{-1} of data (see for example [17]). At a linear collider, the trilinear Higgs self-coupling can be measured through the $\mathrm{e}^+\mathrm{e}^- \to \mathrm{ZHH}$ and $\mathrm{e}^+\mathrm{e}^- \to \mathrm{HH}\nu_e\bar{\nu}_e$ processes. The achievable precision has been studied for the $\mathrm{e}^+\mathrm{e}^- \to \mathrm{ZHH}$ process at $\sqrt{s} = 500$ GeV in the context of the ILC, where the results show that a very large integrated luminosity is required [18]. For this reason, the most favourable channel for the measurement of the Higgs self-coupling is the $\mathrm{e}^+\mathrm{e}^- \to \mathrm{HH}\nu_e\bar{\nu}_e$ process at $\sqrt{s} \geq 1$ TeV. Here the sensitivity increases with increasing centre-of-mass energy and the measurements of the Higgs boson self-coupling (see Section 9) form a central part of the CLIC Higgs physics programme; ultimately a precision of approximately 10 % on λ can be achieved.

4 Monte Carlo, Detector Simulation and Event Reconstruction

The results presented in this paper are based on detailed Monte Carlo (MC) simulation studies consisting of: a full set of SM background processes; full GEANT4 [19, 20] based simulations of the CLIC detector concepts; and a full reconstruction of the simulated events.

4.1 Event Generation

Because of the presence of beamstrahlung photons in the colliding electron and positron beams, it is necessary to generate MC event samples for $\mathrm{e}^+\mathrm{e}^-$, $\mathrm{e}^+\gamma$, $\gamma\mathrm{e}^-$ and $\gamma\gamma$ interactions. The main physics backgrounds, with up to six particles in the final state, were generated using the WHIZARD 1.95 [21] program. In all cases the expected energy spectra for the CLIC beams, including the effects from beamstrahlung and the intrinsic machine energy spread, were used for the initial-state electrons, positrons and beamstrahlung photons. In addition, low-Q^2 processes with quasi-real photons were described using the Weizsäcker-Williams approximation as implemented in WHIZARD. The process of fragmentation and hadronisation was simulated using PYTHIA 6.4 [22] with a parameter set that was tuned to OPAL $\mathrm{e}^+\mathrm{e}^-$ data recorded at LEP (see [13] for details). The decays of τ leptons were simulated using TAUOLA [23]. The mass of the Higgs boson was taken to be 126 GeV[1] and the decays of the Higgs boson were simulated using PYTHIA with the branching fractions listed in [16]. The events from the different Higgs production channels were simulated separately. To avoid double counting, the Higgs boson mass was set to 12 TeV in the generation of the background samples. Monte Carlo samples for the measurement of the top Yukawa coupling measurement (see Section 8) with eight final-state fermions were obtained using the PHYSSIM [24] package; again PYTHIA was used for fragmentation, hadronisation and the Higgs boson decays.

4.2 Simulation and Reconstruction

The GEANT4 detector simulation toolkits MOKKA [25] and SLIC [26] were used to simulate the detector response to the generated events in the CLIC_ILD and CLIC_SiD concepts, respectively. The `QGSP_BERT` physics list was used to model the hadronic interactions of particles in the detectors. The digitisation, namely the translation of the raw simulated energy deposits into detector signals, and the event reconstruction were performed using the MARLIN [27] and `org.lcsim` [28] software packages. Particle flow reconstruction was performed using PANDORAPFA [29, 30]. Vertex reconstruction and heavy-flavour-tagging is performed using the LCFIPLUS program [31]. The detailed training of

[1] A Higgs boson of 125 GeV was used in the generation of $\mathrm{e}^+\mathrm{e}^- \to \mathrm{t\bar{t}H}$.

the neutral network classifiers was performed separately for the centre-of-mass energy and the final state of interest.

Because of the 0.5 ns bunch spacing in the CLIC beams, the pile-up of beam-induced backgrounds can impact the event reconstruction and needs to be accounted for. Realistic levels of pile-up from the most important beam-induced background, the $\gamma\gamma \to$ hadrons process, was included in all the simulated event samples to ensure that the impact on the event reconstruction was correctly modelled. The $\gamma\gamma \to$ hadrons events were simulated separately and a randomly chosen subset corresponding to 60 bunch crossings was superimposed on the physics event before the digitisation step [32]. For the $\sqrt{s} = 350$ GeV samples, where the background rates are lower, 300 bunch crossings were overlaid on the physics event. The impact of the background is small at $\sqrt{s} = 350$ GeV, and is most significant at $\sqrt{s} = 3$ TeV, where approximately 1.2 TeV of energy is deposited in the calorimeters in a time window of 10 ns. A dedicated reconstruction algorithm was developed to identify and remove approximately 90 % of this out-of-time background, using criteria based on the reconstructed transverse momentum p_{T} of the particle and the mean calorimeter cluster time. A more detailed description can be found in [13].

Jet finding was performed using the FASTJET [33] package. Because of the presence of pile-up from $\gamma\gamma \to$ hadrons, it was found that the `ee_kt` (Durham) algorithm employed at LEP was not optimal for CLIC. Instead the hadron-collider inspired k_t algorithm, with the distance parameter R based on $\Delta\eta$ and $\Delta\phi$, was found to give better performance since it increases distances in the forward region, thus reducing the clustering of the (predominantly low transverse momentum) background particles together with those from the hard e^+e^- interaction. The particles clustered into the beam jets are likely to have originated from beam-beam backgrounds, and are removed from the event. As a result of using the R-based k_t algorithm, the impact of the pile-up from $\gamma\gamma \to$ hadrons is largely mitigated, even without the timing cuts described above. Further details are given in [13]. The choice of R was optimised separately for different analyses. In many of the following studies events are forced into a particular N-jet topology. For example, if an event is forced into a two-jet topology, y_{23} is the k_t value at which the event would be reconstructed as three jets. These "y-cut" variables are widely used in a number of event selections, allowing events to be categorised into topologically different final states. In several studies it was found to be advantageous first to apply the hadron-collider inspired k_t algorithm to remove the background clustered in the beam jets and then to recluster the remaining event using `ee_kt` (Durham) algorithm.

The event simulation and reconstruction of the large data samples used in this study was performed using the ILCDIRAC [34] grid submission tools.

5 Higgs Production at $\sqrt{s}$ =350 GeV

The study of the Higgsstrahlung process is central to the precision Higgs physics programme at any future electron-positron collider. This section describes the physics potential from studies of $e^+e^- \to HZ$ at $\sqrt{s} = 350$ GeV and, in particular, focuses on the *model-independent* measurements of HZ production from the kinematic properties of the Z decay products. These measurements provide a precise determination of the coupling of the Higgs to the Z boson. They also provide sensitivity to possible BSM Higgs decay modes to invisible (stable neutral) final states. In addition, studies of exclusive Higgs decay modes probe the couplings of the Higgs boson to fermions.

5.1 Recoil Mass Measurements of $e^+e^- \to HZ$

In the process $e^+e^- \to HZ$, it is possible to efficiently identify $Z \to e^+e^-$ and $Z \to \mu^+\mu^-$ decays, with a selection efficiency that is essentially independent of the H decay mode. The four-momentum of the system (the Higgs boson) recoiling against the Z can be obtained from $E_{rec} = \sqrt{s} - E_{\mathrm{Z}}$ and $\mathbf{p}_{rec} = -\mathbf{p}_{\mathrm{Z}}$, and the *recoil mass*, m_{rec}, will peak sharply around m_{H}. The recoil mass analysis for leptonic decays of the Z is described in Section 5.1.1. Whilst these measurements provide a clean model-independent probe of HZ production, they are limited by the relatively small leptonic branching ratios of the Z. Studies of HZ production with $Z \to q\bar{q}$ are inherently less clean, but are statistically more powerful. Despite the challenges related to the reconstruction of hadronic Z decays in the presence of different Higgs decay modes, a precise and nearly model-independent probe of HZ production can be obtained by analysing the recoil mass in hadronic Z decays, as detailed in Section 5.1.3. When all these measurements are taken together, a model-independent measurement of the g_{HZZ} coupling constant with a precision of < 1 % can be inferred.

5.1.1 Leptonic Decays: $Z \to e^+e^-$ and $Z \to \mu^+\mu^-$

The signature for $e^+e^- \to ZH$ production with $Z \to e^+e^-$ or $Z \to \mu^+\mu^-$ is a pair of oppositely charged high-p_{T} leptons, with an invariant mass consistent with that of the Z boson, $m_{\ell\ell} \sim m_{\mathrm{Z}}$, and a recoil mass, calculated from the four-momenta of the leptons alone, consistent with the Higgs mass, $m_{\mathrm{rec}} \sim m_{\mathrm{H}}$. Consequently, the $\mu^+\mu^-X$ and e^+e^-X final states, where X represents any decay mode of the Higgs boson, can be identified using the properties of the observed leptons alone. Backgrounds from two-fermion final states $e^+e^- \to \ell^+\ell^-$ ($\ell = e, \mu, \tau$) are trivial to remove. The dominant backgrounds are from four-fermion processes with final states consisting of a pair of oppositely-charged leptons and any other possible fermion pair. For both the $\mu^+\mu^- X$ and $e^+e^- X$ channels, the total four-fermion cross section is approximately one thousand times greater than the signal cross section.

The event selection, consisting of a set of preselection cuts and a multivariate analysis, was studied using fully simulated MC events. The preselection required at least one negatively and one positively charged lepton of the lepton flavour of interest (muons or electrons) with an invariant mass loosely consistent with the mass of the Z boson, $40 < m_{\ell\ell} < 126\,\text{GeV}$. For signal events the lepton identification efficiencies are 99 % for muons and 90 % for electrons. Backgrounds from two-fermion processes were essentially eliminated by requiring that the di-lepton system had a large transverse momentum, $p_T > 60\,\text{GeV}$. Four-fermion backgrounds are suppressed by requiring that the *recoil mass* lies between $95 < m_{\text{rec}} < 290\,\text{GeV}$. The lower bound suppresses $e^+e^- \to ZZ$ production. The upper bound is significantly greater than the Higgs boson mass, to allow for the possibility of ZH production with ISR or significant Beamstrahlung, which in the recoil mass analysis results in a tail to the recoil mass distribution since the effective centre-of-mass energy of the e^+e^- collision, $\sqrt{s'}$, is lower than $\sqrt{s}$, which means that the energy (and consequently the mass) of the recoiling system, $E_{\text{rec}} = \sqrt{s} - E_Z$, is over-estimated.

Events passing the preselection cuts were categorised using a multivariate analysis using seven discriminating variables: the transverse momentum (p_T) and invariant mass ($m_{\ell\ell}$) of the candidate Z as reconstructed from the di-lepton system; the cosine of the polar angle ($|\cos\theta|$) of the candidate Z; the acollinearity and acoplanarity of the leptons; the imbalance between the transverse momenta of the two selected leptons ($p_{T1} - p_{T2}$); and the transverse momentum of the highest energy photon in the event. The event selection employed a Boosted Decision Tree (BDT) as implemented in TMVA [35]. The resulting selection efficiencies are summarised in Table 4.

Process	σ/fb	$\varepsilon_{\text{presel}}$	ε_{BDT}	N_{BDT}
$HZ; Z \to \mu^+\mu^-)$	4.6	83.8 %	54.1 %	1253
$\mu^+\mu^- f\bar{f}$	4753	0.8 %	<0.01 %	1905
$HZ; Z \to \mu^+\mu^-)$	4.6	73.3 %	37.1 %	858
$e^+e^- f\bar{f}$	4847	1.2 %	<0.1 %	1558

Table 4: Preselection and selection efficiencies for the ZH signal and most important background processes in the leptonic recoil mass analysis. Numbers of events correspond to $500\,\text{fb}^{-1}$ at $\sqrt{s} = 350\,\text{GeV}$.

A fit to the recoil mass distribution of the selected events (in both the $Z \to e^+e^-$ and $Z \to \mu^+\mu^-$ channels) can be used to extract measurements of the ZH production cross section and the Higgs boson mass. The shape of the background contribution was parameterised using a fourth order polynomial and the shape of the signal distribution was modelled using *Simplified Kernel Estimation* [36–38], which provided a description of the ZH recoil mass distribution in which the Higgs mass subsequently could be varied. To determine the accuracy with which the Higgs mass and the number of signal events (and hence the HZ production cross section) can be measured, 1000 simulated data samples were produced. Each test sample was created by adding the high statistics selected signal sample (scaled to the correct normalisation) to the smooth fourth-order polynomial background, then applying Poissonian fluctuations to individual bins of the resulting smooth distribution to create a representative $500\,\text{fb}^{-1}$ data sample. Each of the 1000 simulated data samples created in this way was fitted allowing the Higgs mass, the signal normalisation and the background normalisation to vary. Figure 6a displays the results of fitting a typical test sample for the $\mu^+\mu^- X$ channel, while figure Figure 6b displays the results for the $e^+e^- X$ channel. In the $e^+e^- X$ channel fits were performed with and without applying an algorithm to recover Bremsstrahlung photons. The resulting measurement precisions for the ZH cross section and the Higgs boson mass are summarised in Table 5. With $\mathscr{L}_{\text{int}} = 500\,\text{fb}^{-1}$ of data at $\sqrt{s} = 350\,\text{GeV}$, the combined precision on the Higgs boson mass is 110 MeV and the combined precision on the ZH cross section is

$$\frac{\Delta\sigma(\text{ZH})}{\sigma(\text{ZH})} = 3.8\,\%\,.$$

Channel	Quantity	Precision
$\mu^+\mu^- X$	m_H	122 MeV
	$\sigma(\text{ZH})$	4.72 %
$e^+e^- X$	m_H	278 MeV
	$\sigma(\text{ZH})$	7.21 %
$e^+e^- X$	m_H	359 MeV
+ Bremstrahlung recovery	$\sigma(\text{ZH})$	6.60 %

Table 5: Summary of measurement precisions ($\mathscr{L}_{\text{int}} = 500\,\text{fb}^{-1}$ at $\sqrt{s} = 350\,\text{GeV}$) from the leptonic recoil mass analyses in the $\mu^+\mu^- X$ and $e^+e^- X$ channels.

5.1.2 Invisible Higgs Decays

The above recoil mass analysis of leptonic decays of the Z boson in $e^+e^- \to ZH$ events provides a measurement of the

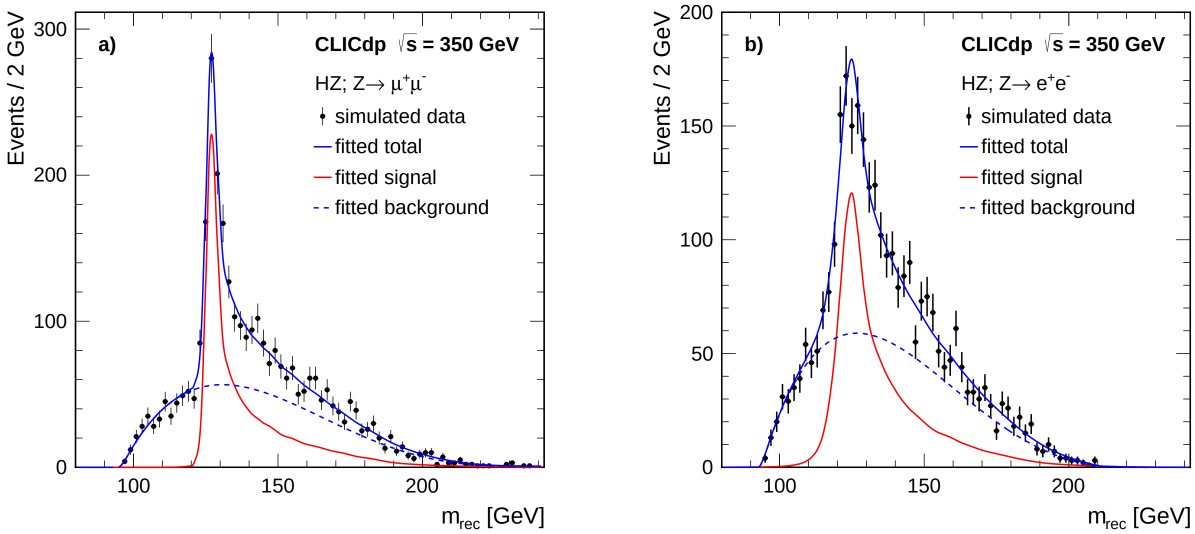

Fig. 6: Results of fitting example test samples corresponding to $\mathscr{L}_{\text{int}} = 500\,\text{fb}^{-1}$ at $\sqrt{s} = 350\,\text{GeV}$ for (a) the $\mu^+\mu^- X$ channel and (b) the $e^+e^- X$ channel (with Bremstrahlung recovery).

Higgstrahlung cross section, independent of the Higgs boson decay model. The recoil mass technique can also be used to search for BSM decays modes of the Higgs boson into long-lived neutral "invisible" final states. At an e^+e^- collider a search for invisible Higgs decays is possible by identification of $e^+e^- \to ZH$ events with a visible $Z \to q\bar{q}$ decay and missing energy. Such events would typically produce a clear two-jet topology with invariant mass consistent with m_Z, significant missing energy and a recoil mass corresponding to the Higgs mass.

To identify candidate invisible Higgs decays, a loose preselection is imposed requiring: i) a clear two-jet topology, defined by $\log_{10} y_{23} < -2.0$ and $\log_{10} y_{34} < -3.0$, where the y-cut variables are defined in Section 4.2; ii) a di-jet invariant mass consistent with the Z mass, $84\,\text{GeV} < m_{q\bar{q}} < 104\,\text{GeV}$; and iii) the reconstructed momentum of the candidate Z boson pointing away from the beam direction, $|\cos\theta_Z| < 0.7$. After the preselection, a BDT multivariate analysis technique was applied using the TMVA package [35] to further separate invisible Higgs signal from the SM background. In addition to $m_{q\bar{q}}$, $|\cos\theta_Z|$ and $\log_{10} y_{23}$, four other discriminating variables were employed: m_{rec}, the recoil mass of the invisible system recoiling against the observed Z boson; $|\cos\theta_q|$, the decay angle of one of the quarks in the Z rest frame, relative to the direction of flight of the Z boson; p_T, the magnitude of the transverse momentum of the Z boson; E_{vis}, the visible energy in the event. As an example, Figure 7 shows the recoil mass distribution for the simulated invisible Higgs decays and the total SM background.

Figure 8 shows the BDT classifier distributions for simulated invisible Higgs decays (for the case of a 100 % *BR* to

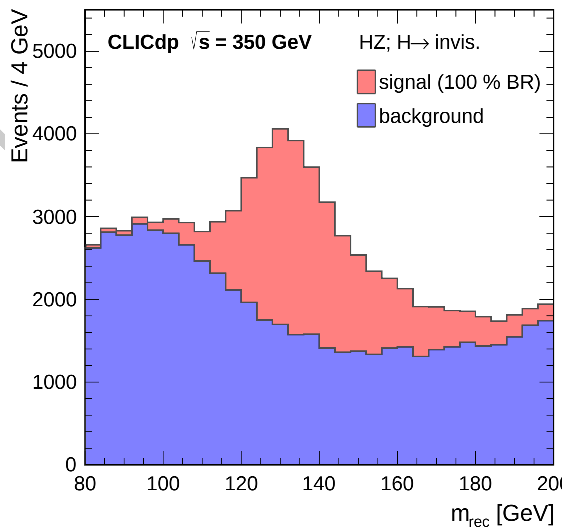

Fig. 7: The reconstructed recoil mass distribution for the invisible Higgs analysis showing the $H \to$ invis. signal (for a $100\,\%$ *BR*) and all SM backgrounds for $500\,\text{fb}^{-1}$ at $\sqrt{s} = 350\,\text{GeV}$.

invisible final states) and the sum of all SM background processes. Reasonable separation is achieved. The optimal BDT cut, minimising the statistical uncertainty on the cross section for invisible Higgs decays was found at a BDT value of 0.088. In the case where the branching ratio to BSM invisible final states is zero (or very small), the uncertainty on the invisible branching ratio is determined by the statistical

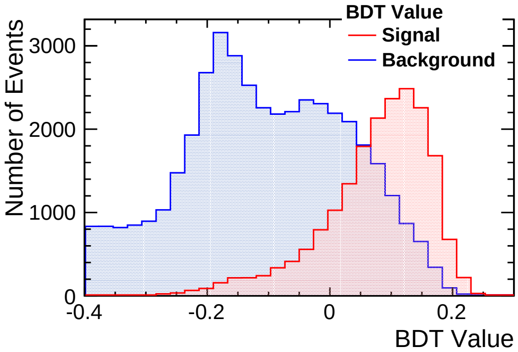

Fig. 8: The expected BDT distribution for the invisible Higgs analysis for $\mathrm{H} \to \mathrm{invis.}$ signal and all SM backgrounds for $500\,\mathrm{fb}^{-1}$ at $\sqrt{s} = 350\,\mathrm{GeV}$.

Process	σ/fb	$\varepsilon_{\mathrm{presel}}$	$\varepsilon_{\mathrm{BDT}>0.088}$	$N_{\mathrm{BDT}>0.088}$
$\mathrm{q\bar{q}}\ell\nu$	5914	<0.7 %	<0.1 %	900
$\mathrm{q\bar{q}}\nu\bar{\nu}$	325	16.7 %	1.5 %	2414
ZH (SM decays)	93.4	0.2 %	<0.1 %	21
$\mathrm{H} \to \mathrm{invis.}$		41.0 %	20.7 %	9956

Table 6: Summary of the invisible Higgs decay event selection at $\sqrt{s} = 350\,\mathrm{GeV}$, giving the raw cross sections, preselection efficiency, overall selection efficiency for a BDT cut of BDT > 0.088 and the expected numbers of events passing the event selection for an integrated luminosity of $500\,\mathrm{fb}^{-1}$. For the invisible Higgs decay signal the number of selected events corresponds to a *BR* of 100 %. Contributions from all other backgrounds are found to be negligibly small.

fluctuations on the background after the event selection:

$$\Delta BR(\mathrm{H} \to \mathrm{invis.}) = \frac{\sqrt{b}}{s(100\,\%)}, \quad (1)$$

where b is the expected number of selected SM background events and $s(100\,\%)$ is the expected number of invisible Higgs decays in the case where $BR(\mathrm{H} \to \mathrm{invis.}) = 100\,\%$. Table 6 summarises the invisible Higgs decay event selection; the dominant background processes arise from the the final states $\mathrm{q\bar{q}}\ell\nu$ and $\mathrm{q\bar{q}}\nu\bar{\nu}$. The resulting one sigma uncertainty on $BR(\mathrm{H} \to \mathrm{invis.})$ is 0.57 % (in the case where the invisible Higgs branching ratio is small) and the corresponding 90 % C.L. upper limit ($500\,\mathrm{fb}^{-1}$ at $\sqrt{s}$=350 GeV) on the invisible Higgs branching ratio in the modified frequentist approach [39] is:

$$BR(\mathrm{H} \to \mathrm{invis.}) < 0.97\,\% \quad \text{at } 90\,\%\ \text{C.L.}$$

It should be noted that the SM Higgs decay chain $\mathrm{H} \to \mathrm{ZZ}^* \to \nu\bar{\nu}\nu\bar{\nu}$ has a combined branching ratio of 0.1 % and is not measurable.

5.1.3 Hadronic Decays: $Z \to q\bar{q}$

In the process $\mathrm{e^+e^-} \to \mathrm{HZ}$ it is possible to cleanly identify $\mathrm{Z} \to \mathrm{e^+e^-}$ and $\mathrm{Z} \to \mu^+\mu^-$ decays regardless of the decay mode of the Higgs boson and, consequently, the selection efficiency is almost independent of the Higgs decay mode. In contrast, for $\mathrm{Z} \to \mathrm{q\bar{q}}$ decays, the selection efficiency will show a stronger dependence on the Higgs decay mode. For example, $\mathrm{e^+e^-} \to (\mathrm{H} \to \mathrm{b\bar{b}})(\mathrm{Z} \to \mathrm{q\bar{q}})$ events will consist of four jets and the reconstruction of the Z boson will be complicated by ambiguities in associations of particles with jets and the three-fold ambiguity in associating four jets to the hadronic decays of the Z and H. For this reason, it is much more difficult to construct a selection based only on the reconstructed $\mathrm{Z} \to \mathrm{q\bar{q}}$ decay that has a selection efficiency independent of the Higgs decay mode. The strategy adopted is to: i) first reject events consistent with a number of clear background topologies using the information from the whole event; and then ii) identify $\mathrm{e^+e^-} \to \mathrm{H}(\mathrm{Z} \to \mathrm{q\bar{q}})$ events solely based on the properties from the candidate $\mathrm{Z} \to \mathrm{q\bar{q}}$ decay.

The $\mathrm{H}(\mathrm{Z} \to \mathrm{q\bar{q}})$ event selection proceeds in three separate stages. In the first stage, to allow for possible BSM invisible Higgs decay modes, events are divided into candidate visible Higgs decays and candidate invisible Higgs decays, in both cases produced along with a $\mathrm{Z} \to \mathrm{q\bar{q}}$. Events are categorised as potential visible Higgs decays if they are not compatible with a clear two-jet topology:

– $\log_{10}(y_{23}) > -2.0$ or $\log_{10}(y_{34}) > -3.0$.

All other events are considered as candidates for an invisible Higgs decay analysis, based on that described in Section 5.1.2, although with looser requirements to make the overall analysis more inclusive.

Preselection cuts then reduce the backgrounds from large cross section processes such as $\mathrm{e^+e^-} \to \mathrm{q\bar{q}}$ and $\mathrm{e^+e^-} \to \mathrm{q\bar{q}q\bar{q}}$. The preselection variables are formed by forcing each event into three, four and five jets. In each case, the best candidate for being a hadronically decaying Z boson is chosen as the jet pair giving the di-jet invariant mass ($m_{\mathrm{q\bar{q}}}$) closest to m_{Z}, only considering jets with more than three charged particles. The invariant mass of the system recoiling against the candidate hadronically decaying gauge boson, m_{rec}, is calculated assuming $E_{\mathrm{rec}} = \sqrt{s} - E_{\mathrm{q\bar{q}}}$ and $\mathbf{p}_{\mathrm{rec}} = -\mathbf{p}_{\mathrm{q\bar{q}}}$. In addition, the invariant mass of all the visible particles not originating from the candidate $\mathrm{Z} \to \mathrm{q\bar{q}}$ decay, m_{vis} is calculated. It is important to note that m_{vis} is only used to reject specific background topologies in the preselection and is not used in the main selection as it will depend strongly on the type of Higgs decay. The preselection cuts are

– $70\,\mathrm{GeV} < m_{\mathrm{q\bar{q}}} < 110\,\mathrm{GeV}$ and $80\,\mathrm{GeV} < m_{\mathrm{rec}} < 200\,\mathrm{GeV}$;

– the background from $e^+e^- \to q\bar{q}$ is suppressed by removing events with overall $p_T < 20\,\mathrm{GeV}$ and either $|\cos\theta_{mis}| > 0.90$ or $\log_{10} y_{34} > -2.5$

– events with little missing transverse momentum ($p_T < 20\,\mathrm{GeV}$) are forced into four jets and are rejected if the reconstructed di-jet invariant masses (and particle types) are consistent with the expectations for $e^+e^- \to q\bar{q}\ell\ell$, $e^+e^- \to ZZ \to q\bar{q}q\bar{q}$, $e^+e^- \to WW \to q\bar{q}q\bar{q}$.

The final step in the event selection is a multivariate analysis. In order not to bias the event selection efficiencies for different Higgs decay modes, only variables relating to the candidate $Z \to q\bar{q}$ decay are used in the selection. Forcing the event into four jets is the right approach for $H(Z \to q\bar{q})$ for Higgs decays to two-body final states, but not necessarily for final states such as $H \to WW^* \to q\bar{q}q\bar{q}$, where there is the chance that one of the jets from the WW^* decay will be merged with one of the jets from the $Z \to q\bar{q}$, potentially biasing the selection against $H \to WW^*$ decays. To mitigate this effect, the Z candidate for the event selection can either be formed from the four-jet topology as described above, or can be formed from a jet pair after forcing the event into a five-jet topology. The latter case is only used when $\log_{10} y_{45} > -3.5$ and the five-jet reconstruction gives a better Z and H candidates than the four-jet reconstruction. Attempting to reconstruct events in the six-jet topology is not found to improve the overall analyses. Having chosen the best candidate Z in the event (from either the four-jet or five-jet reconstruction), it is used to form variables for the multivariate selection; information about the remainder of the event is not used.

A relative likelihood selection is used to classify all events passing the preselection cuts. Two event categories are considered: the $e^+e^- \to ZH \to q\bar{q}H$ signal and all non-Higgs background processes. The relative likelihood for an event being signal is defined as

$$\mathscr{L} = \frac{L_{\mathrm{signal}}}{L_{\mathrm{signal}} + L_{\mathrm{back}}}\,,$$

where the individual absolute likelihood L for each event type is formed from normalised probability distributions $P_i(x_i)$ of the discriminating variables x_i for that event type:

$$L = \sigma_{\mathrm{presel}} \times \prod_i^N P_i(x_i)\,,$$

where σ_{presel} is the cross section after the preselection cuts. The discriminating variables used, all of which are based on the candidate $Z \to q\bar{q}$ decay, are: the 2D distribution of $m_{q\bar{q}}$ and m_{rec}; the polar angle of the Z candidate, $|\cos\theta_Z|$; and the modulus of angle of jets from the Z decay relative to its direction after boosting into its rest frame, $|\cos\theta_q|$. The clearest separation between signal and background is obtained from $m_{q\bar{q}}$ and the recoil mass m_{rec}, as shown in Figure 9.

Process	σ/fb	$\varepsilon_{\mathrm{presel}}$	$\varepsilon_{\mathscr{L}>0.65}$	$N_{\mathscr{L}>0.65}$
$q\bar{q}$	25180	0.4 %	0.07 %	8525
$q\bar{q}\ell\nu$	5914	11.2 %	0.20 %	5767
$q\bar{q}q\bar{q}$	5847	3.8 %	0.49 %	14142
$q\bar{q}\ell\ell$	1704	1.5 %	0.22 %	1961
$q\bar{q}\nu\bar{\nu}$	325	0.6 %	0.04 %	60
$H\nu_e\bar{\nu}_e$	52	2.5 %	0.23 %	60
$HZ; Z \to q\bar{q}$	93	42.0 %	22.6 %	10568

Table 7: Summary of the $(H \to \mathrm{vis.})(Z \to q\bar{q})$ event selection at $\sqrt{s} = 350\,\mathrm{GeV}$, giving the raw cross sections, preselection efficiency, overall selection efficiency for a likelihood cut of $\mathscr{L} > 0.65$ and the expected numbers of events passing the event selection for an integrated luminosity of $500\,\mathrm{fb}^{-1}$.

The signal is clearly peaked at $m_{q\bar{q}} \sim m_Z$ and $m_{\mathrm{rec}} \sim m_H$. The use of 2D mass distributions accounts for the most significant correlations between the likelihood variables.

In this high-statistics limit, the fractional error on the number of signal events (where the Higgs decays to visible final states), s_{vis}, given a background b is

$$\frac{\Delta s_{\mathrm{vis}}}{s_{\mathrm{vis}}} = \frac{\sqrt{s_{\mathrm{vis}} + b}}{s_{\mathrm{vis}}}\,,$$

and this is minimised with the selection requirement $\mathscr{L} > 0.65$. The selection efficiencies and expected numbers of events for the signal dominated region, $\mathscr{L} > 0.65$, are listed in Table 7, corresponding to a fractional error on the number of signal events of 1.9 %. By fitting the *shape* of the likelihood distribution to signal and background contributions, this uncertainty is reduced to

$$\frac{\Delta s_{\mathrm{vis}}}{s_{\mathrm{vis}}} = 1.7\,\%\,.$$

5.1.4 Model Independent HZ Cross Section

By combining the two analyses for HZ production where $Z \to q\bar{q}$ and the Higgs decays either to invisible final states (see Section 5.1.2) or to visible final states (see Section 5.1.3), it is possible to determine the absolute cross section for $e^+e^- \to HZ$ in an essentially model-independent manner:

$$\sigma(HZ) = \frac{\sigma_{\mathrm{vis}} + \sigma_{\mathrm{invis}}}{BR(Z \to q\bar{q})}\,.$$

Here a slightly modified version of the invisible Higgs analysis is employed. With the exception of the cuts on y_{23} and y_{34}, the invisible Higgs analysis employs the same preselection as for the visible Higgs analysis and a likelihood multivariate discriminant is used.

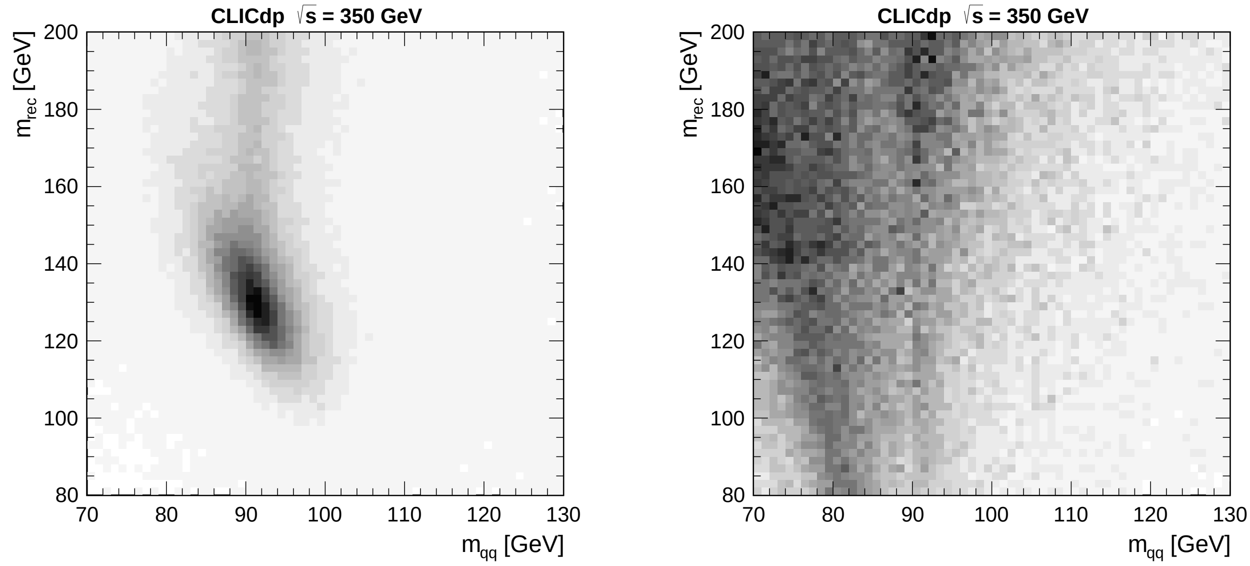

Fig. 9: The distributions of $m_{\mathrm{q\bar{q}}}$ versus m_{rec} for events passing the $\mathrm{H}(\mathrm{Z}\to\mathrm{q\bar{q}})$: (left) HZ signal and (right) all non-H background processes.

Since the fractional uncertainties (relative to the total cross section) on the visible and invisible cross sections are 1.7 % and 0.6 % respectively, the fractional uncertainty on the total cross section will be (at most) the quadrature sum of the two fractional uncertainties, namely 1.8 %. This measurement is only truly model-independent if the overall selection efficiencies are independent of the Higgs decay mode. For all final state topologies, the combined (visible + invisible) selection efficiency lies is the range $19-26\,\%$ regardless of the Higgs decay mode, covering a very wide range of event topologies. To assess the level of model independence, the Higgs decay modes in the MC samples are modified and the total (visible + invisible) cross section is extracted assuming the SM Higgs branching ratio. Table 8 shows the resulting biases in the extracted total cross section for the case when a $BR(\mathrm{H}\to X)\to BR(\mathrm{H}\to X)+0.05$. Even for these very large modifications of the Higgs branching ratios over a wide range of final-state topologies, the resulting biases in the extracted total HZ cross section is less than 1 % (compared to the 1.8 % statistical uncertainty). However, such large deviations would have significant observable effects on the exclusive Higgs branching ratio analyses (at the LHC and CLIC) and it is concluded that the analysis can be considered to give an effectively model-independent measurement of the $\mathrm{H}(\mathrm{Z}\to\mathrm{q\bar{q}})$ cross section (unless there are very large BSM effects on the Higgs branching ratios which would already be apparent).

Combining the model-independent measurements of the HZ cross section from $\mathrm{Z}\to\ell^+\ell^-$ and $\mathrm{Z}\to\mathrm{q\bar{q}}$ gives an absolute measurement of the HZ cross section with a precision of:

$$\frac{\Delta\sigma(\mathrm{HZ})}{\sigma(\mathrm{HZ})} = 1.65\,\%\,,$$

and, consequently, the absolute coupling of the H boson to the Z boson is determined to:

$$\frac{\Delta g_{\mathrm{HZZ}}}{g_{\mathrm{HZZ}}} = 0.8\,\%\,.$$

Decay mode	$\Delta(BR)$	$\sigma^{\mathrm{vis}}+\sigma^{\mathrm{invis}}$ Bias
$\mathrm{H}\to\mathrm{invis}$	+5 %	−0.01 %
$\mathrm{H}\to\mathrm{q\bar{q}}$	+5 %	+0.05 %
$\mathrm{H}\to\mathrm{WW}^*$	+5 %	−0.18 %
$\mathrm{H}\to\mathrm{ZZ}^*$	+5 %	−0.30 %
$\mathrm{H}\to\tau^+\tau^-$	+5 %	+0.60 %
$\mathrm{H}\to\gamma\gamma$	+5 %	+0.79 %
$\mathrm{H}\to\mathrm{Z}\gamma$	+5 %	−0.74 %
$\mathrm{H}\to\mathrm{WW}^*\to\mathrm{q\bar{q}q\bar{q}}$	+5 %	−0.49 %
$\mathrm{H}\to\mathrm{WW}^*\to\mathrm{q\bar{q}}\ell\nu$	+5 %	+0.10 %
$\mathrm{H}\to\mathrm{WW}^*\to\tau\nu\tau\nu$	+5 %	−0.98 %

Table 8: Biases in the extracted $\mathrm{H}(\mathrm{Z}\to\mathrm{q\bar{q}})$ cross section if the Higgs branching ratio to a specific final state is increased by 5 %, i.e. $BR(\mathrm{H}\to X)\to BR(\mathrm{H}\to X)+0.05$.

5.2 Exclusive Higgs Branching Ratio Measurements at $\sqrt{s}=350\,\mathrm{GeV}$

The previous section focussed on inclusive measurements of the $\mathrm{e}^+\mathrm{e}^-\to\mathrm{HZ}$ production cross section, which provide a model-independent determination of the coupling at the HZZ vertex. In contrast, measurements of Higgs production and decay to exclusive final states, provides a determination of the product $\sigma(\mathrm{HZ}) \times BR(\mathrm{H} \to X)$, where X is a particular final state. This section focuses on the exclusive measurements of the Higgs decay branching ratios at $\sqrt{s} = 350\,\mathrm{GeV}$. Higgs boson decays to $\mathrm{b\bar{b}}$, $\mathrm{c\bar{c}}$ and gg are studied in Section 5.2.1. The measurement of $\mathrm{H} \to \tau^+\tau^-$ decays is described in Section 5.2.2, and the $\mathrm{H} \to \mathrm{WW}^*$ decay mode is described in Section 5.2.3.

5.2.1 *Measurement of the* $H \to b\bar{b}, c\bar{c}, gg$ *Branching Ratios*

As can be seen from Table 1, at $\sqrt{s} = 350\,\mathrm{GeV}$ the $\mathrm{e^+e^-} \to \mathrm{HZ}$ Higgsstrahlung cross section is approximately four times greater than the $\mathrm{e^+e^-} \to \mathrm{H\nu_e\bar{\nu}_e}$ WW-fusion cross section for unpolarised beams (or approximately a factor 2.5 with -80 % electron beam polarisation). For Higgsstrahlung, the signature for $\mathrm{H} \to \mathrm{b\bar{b}}, \mathrm{c\bar{c}}, \mathrm{gg}$ decays depends on the Z decay mode, resulting in three distinct final state topologies, $jjjj$, $jj\ell\ell$, and $jj\nu\nu$, where j represents a quark/gluon jet from the Z or H decay. It should be noted that the $jj\nu\nu$ final state contains approximately equal contributions from Higgsstrahlung and WW-fusion, although the event kinematics are very different.

To maximise the statistical power of the $\mathrm{H} \to \mathrm{b\bar{b}}, \mathrm{c\bar{c}}, \mathrm{gg}$ branching ratio measurements, all topologies are considered: four jets, two jets plus two leptons, and two jets plus missing momentum (from the unobserved neutrinos). A candidate $\mathrm{Z} \to \ell^+\ell^-$ decay is identified as a pair of oppositely charged identified leptons (electrons or muons) with energy above 10 GeV and and isolation requirement that there should be less then 20 GeV of energy from other particles within a cone with a half-angle 10° around each lepton direction. In the case of multiple possibilities, the $\ell^+\ell^-$ pair with the closest invariant mass to the Z mass is tagged as the Z candidate. Having removed the $\mathrm{Z} \to \ell^+\ell^-$ candidate, the remaining particles are clustered into two jets with the Durham jet algorithm to form the H candidate. Final states with hadronically decaying Z bosons are identified by clustering the event into four jets. For each event, the most probable Z and H candidates are selected by choosing the jet combination that minimises

$$\chi^2 = (m_{ij} - m_{\mathrm{H}})^2/\sigma_{ij}^2 + (m_{kl} - m_{\mathrm{Z}})/\sigma_{kl}^2 ,$$

where σ_{ij} is the estimated invariant mass resolution for that jet pair. In the case of the $\mathrm{b\bar{b}}\nu\bar{\nu}$ final state, either from HZ with $\mathrm{Z} \to \nu\bar{\nu}$ or from $\mathrm{H}\nu\bar{\nu}$, the event is clustered into two jets, forming the H candidate.

All events are then classified using gradient boosted BDTs using reconstructed kinematic variables from each of the above three event topology hypotheses. The variables used include jet energies, event shape variables (such as thrust and sphericity) and the masses of H and Z candidates. In total four separate BDT classifiers are used, one for each of the four signal final states ($\mathrm{He^+e^-}$, $\mathrm{H\mu^+\mu^-}$, $\mathrm{Hq\bar{q}}$ and $\mathrm{H\nu\bar{\nu}}$), irrespective of the nature of the hadronic Higgs decay mode. The non-Higgs background channels, dominated by the four-fermion final states $\mathrm{q\bar{q}}\nu\bar{\nu}$, $\mathrm{q\bar{q}}\ell\nu$, $\mathrm{q\bar{q}}\ell\ell$ and $\mathrm{q\bar{q}q\bar{q}}$ as well as non-di-jet Higgs decay modes are taken as background for all classifiers. In addition, the three other signal modes are included in the background for a given classifier. The training is performed with a dedicated training sample, simultaneously training all four classifiers. At this point no flavour-tag information is used.

Each event is evaluated with all four classifiers. An event is only accepted if *exactly one* of the signal classifiers is above a positive threshold and *all* the other classifiers are below a corresponding negative threshold. The event is then tagged as a candidate for the corresponding signal process. If none of the classifiers passes the selection threshold, the event is considered as background and is rejected from the analysis. Table 9 summarises the classification of all events into the four signal categories, with event numbers based on an integrated luminosity of $500\,\mathrm{fb}^{-1}$.

The $\mathrm{H}\nu\bar{\nu}$ final state has contributions from both Higgsstrahlung and WW-fusion events, while the other three final states with $\mathrm{Z} \to \mathrm{e^+e^-}, \mu^+\mu^-, \mathrm{q\bar{q}}$ only have Higgs contributions from HZ production (the tight requirement that the $\mathrm{e^+e^-}$ invariant mass is consistent with the Z-boson mass effectively removes the contribution from the ZZ-fusion process $\mathrm{e^+e^-} \to \mathrm{He^+e^-}$). The second stage in the analysis is to measure the contributions of the hadronic Higgs decays into the $\mathrm{H} \to \mathrm{b\bar{b}}$, $\mathrm{H} \to \mathrm{c\bar{c}}$ and $\mathrm{H} \to \mathrm{gg}$ exclusive final states, as well as to determine the ratio of Higgsstrahlung and WW-fusion events in the $\mathrm{H}\nu\bar{\nu}$ final state. The jets forming the Higgs candidate are classified with the LCFIPlus [31] flavour-tagging package, where each of the two jets is assigned a b-likeness and a c-likeness. The resulting two-dimensional distributions of the different classifiers are shown in Figure 10, where separation between the different event categories can be seen. However, none of these classifiers alone provides a perfect separation of the different final states. A two-dimensional template fit is performed to simultaneously extract the contributions from $\mathrm{H} \to \mathrm{b\bar{b}}$, $\mathrm{H} \to \mathrm{c\bar{c}}$, $\mathrm{H} \to \mathrm{gg}$ in the b-likeness and a c-likeness variables. For this fit, the $\mathrm{H} \to$ other and the non-Higgs backgrounds are taken as external inputs, assumed to be determined in other analyses.

The $\mathrm{H}\nu\bar{\nu}$ final state, which has roughly equal contributions from the $\mathrm{e^+e^-} \to \mathrm{HZ}$ and the WW-fusion process, has to be treated differently. Here the p_{T} distribution of the Higgs bosons, as shown in Figure 11, is substantially different for Higgsstrahlung and WW-fusion processes (as is expected

Process	σ/fb	$\varepsilon_{\mathrm{BDT}}$, classified as				N_{BDT}, classified as			
		$\mathrm{H}\nu\bar{\nu}$	$\mathrm{He^+e^-}$	$\mathrm{H}\mu^+\mu^-$	$\mathrm{Hq\bar{q}}$	$\mathrm{H}\nu\bar{\nu}$	$\mathrm{He^+e^-}$	$\mathrm{H}\mu^+\mu^-$	$\mathrm{Hq\bar{q}}$
$\mathrm{e^+e^-} \to \mathrm{H}\nu\bar{\nu}$	X	X %	X %	X %	X %	X	X	X	X
$\mathrm{e^+e^-} \to \mathrm{He^+e^-}$	X	X %	X %	X %	X %	X	X	X	X
$\mathrm{e^+e^-} \to \mathrm{H}\mu^+\mu^-$	X	X %	X %	X %	X %	X	X	X	X
$\mathrm{e^+e^-} \to \mathrm{Hq\bar{q}}$	X	X %	X %	X %	X %	X	X	X	X
$\mathrm{e^+e^-} \to \mathrm{q\bar{q}}\nu\bar{\nu}$	X	X %	X %	X %	X %	X	X	X	X
$\mathrm{e^+e^-} \to \mathrm{q\bar{q}}\ell\nu$	X	X %	X %	X %	X %	X	X	X	X
$\mathrm{e^+e^-} \to \mathrm{q\bar{q}}\ell\ell$	X	X %	X %	X %	X %	X	X	X	X
$\mathrm{e^+e^-} \to \mathrm{q\bar{q}q\bar{q}}$	X	X %	X %	X %	X %	X	X	X	X
$\mathrm{e^+e^-} \to \mathrm{q\bar{q}}$	X	X %	X %	X %	X %	X	X	X	X

Table 9: Summary of the expected numbers of events for the different Higgs and non-Higgs final states passing the hadronic Higgs decay signal selection for 500 fb^{-1} at $\sqrt{s} = 350\,\mathrm{GeV}$ (unpolarised beams). *Numbers outdated – analysis ongoing.*

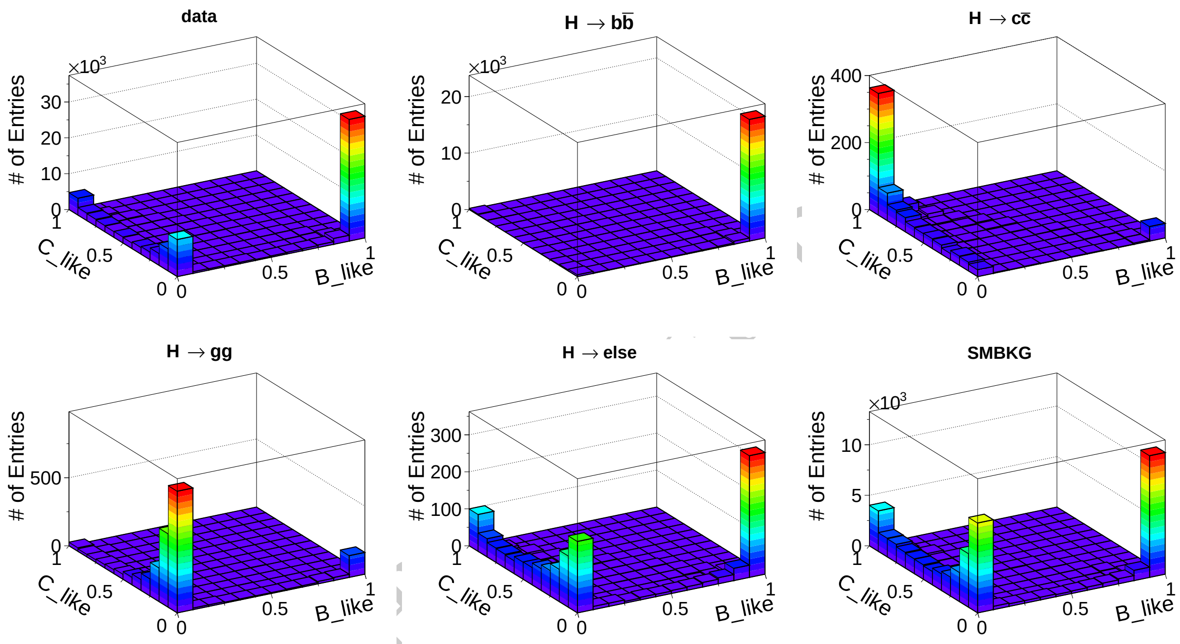

Fig. 10: The distribution of the b-likeness and c-likeness for simulated data as well as for the different event classes of $\mathrm{H} \to \mathrm{b\bar{b}}$, $\mathrm{H} \to \mathrm{c\bar{c}}$ and $\mathrm{H} \to \mathrm{gg}$ and for background from other Higgs decays and non-Higgs SM background.

for s- and t-channel processes). In addition to the contributions from $\mathrm{H} \to \mathrm{b\bar{b}}$, $\mathrm{H} \to \mathrm{c\bar{c}}$, $\mathrm{H} \to \mathrm{gg}$, $\mathrm{H} \to$ other and the non-Higgs background, the relative contributions for the two Higgs production modes can be determined by fitting templates to the p_{T} distribution with the relative fraction of the contributions from Higgsstrahlung and WW-fusion left as the only free parameter for events with a high b-likeness which can be selected with high purity. The $\sigma \times BR$ measurements for the two Higgs production modes and the three investigated hadronic decay modes of the Higgs are thus determined via the relative contribution of the two production modes to the overall measured $\mathrm{H}\nu\bar{\nu}$ signal. For the final extraction of $\sigma \times BR$ this statistical separation of the two contributions is combined with the measured number of $\mathrm{H} \to \mathrm{b\bar{b}}$, $\mathrm{H} \to \mathrm{c\bar{c}}$ and $\mathrm{H} \to \mathrm{gg}$ decays in the $\mathrm{H}\nu\bar{\nu}$ event sample, as discussed above.

The results of the above analysis are summarised in Table 10, giving the statistical uncertainties of the various $\sigma \times BR$ measurements. For the $\mathrm{H} \to \mathrm{c\bar{c}}$ and $\mathrm{H} \to \mathrm{gg}$ the combination of Higgsstrahlung and WW-fusion is extracted from the fit. The table also gives the expected uncertainty for the measurement of the fraction of WW-fusion events in $\mathrm{H}\nu\bar{\nu}$ with $\mathrm{H} \to \mathrm{b\bar{b}}$ events. This fraction is 0.48 with all selection cuts in the analysis, while the overall ratio of WW-fusion and Higgsstrahlung events, irrespective of the Z decay mode, is 0.224. From these measurements, the statistical uncertainties for the branching ratios in Higgsstrahlung and WW-

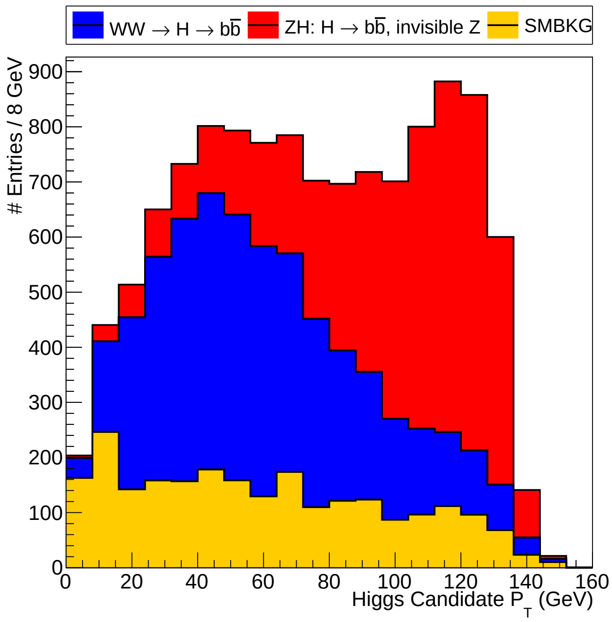

Fig. 11: The distribution of the Higgs candidate p_T for events selected as $H\nu\bar{\nu}$ with high b-likeness in the simulated H boson sample, showing the contributions from Higgsstrahlung and WW-fusion processes as well as the non-Higgs background as stacked distributions.

fusion are determined separately also for $H \to c\bar{c}$ and $H \to gg$. Since the parameters in this analysis are determined in a combined extraction from overlapping contributions, the results are correlated. The correlations are summarised in ... *(still needs to be done...)*. These correlations are taken into account when using the results in combined global fits to extract the Higgs couplings.

Still need to update plots and finalise numbers.

5.2.2 Measurement of the $H \to \tau^+\tau^-$ Branching Ratio

Because of the neutrino(s) produced in τ decays, the signature for $H \to \tau^+\tau^-$ is less distinct than that for other decay modes. The invariant mass of the visible decay products of the $\tau^+\tau^-$ system will be less than m_H, and it is not possible to identify $H \to \tau^+\tau^-$ decays from the WW-fusion process or from Higgsstrahlung events where $Z \to \nu\bar{\nu}$. For this reason, the product of $\sigma(HZ) \times BR(H \to \tau^+\tau^-)$ is only determined for the case of hadronic Z decays. Here the experimental signature is two hadronic jets from $Z \to q\bar{q}$ and two isolated low-multiplicity narrow "jets" from the two tau decays. Candidate τ leptons are identified using the TauFinder algorithm [40], which is a seeded-cone based jet-clustering algorithm. The algorithm was optimised to distinguish the tau lepton decay products from hadronic gluon or quark jets.

Measurement	Statistical uncertainty Higgsstrahlung	WW-fusion
$\sigma(H+X) \times BR(H \to b\bar{b})$	0.75%	1.4%
$\sigma(H+X) \times BR(H \to c\bar{c})$	5.8%	
$\sigma(H+X) \times BR(H \to gg)$	3.6%	
Derived results		
$\sigma(H+X) \times BR(H \to c\bar{c})$	X	X
$\sigma(H+X) \times BR(H \to gg)$	X	X
Separation of Higgsstrahlung and WW-fusion		
$\frac{\sigma(WW-\text{fusion}) \times BR(H \to b\bar{b})}{\sigma(HZ) \times BR(H \to b\bar{b}, Z \to \nu\bar{\nu}) + \sigma(WW-\text{fusion}) \times BR(H \to b\bar{b})}$		*xx*

Table 10: Summary of statistical uncertainties for $H \to b\bar{b}$, $H \to c\bar{c}$ and $H \to gg$ at $\sqrt{s} = 350\,\text{GeV}$ derived from the template fit, corresponding to an integrated luminosity of $500\,\text{fb}^{-1}$. The separated uncertainties for $H \to c\bar{c}$ and $H \to gg$ are determined by by taking into account the fraction of WW-fusion events in the $H\nu\bar{\nu}$ final state for the WW-fusion results. The uncertainty of the fraction of WW-fusion events in the $H\nu\bar{\nu}$ final state is also given. Results from ongoing analysis, still without the inclusion of one background channel — full analysis will likely result in a slight deterioration of results.

Tau cones are seeded from single tracks (p_T >5 GeV). The seeds are used to define narrow cones of 0.05 radian half-angle. The cones are required to contain either one or three charged particles (from one- and three-prong tau decays) and further rejection of background from hadronic jets is implemented using cuts on isolation-related variables. Tau cones which contain identified electrons or muons are rejected and only the hadronic one- and three-prong τ decays are retained. The τ identification efficiency for hadronic tau decays is found to be 73 % and the fake rate to mistake a quark for a τ is 5%. The fake rate is relatively high, but is acceptable in this study as the background from final states with quarks can be suppressed using global event properties.

Events with two identified hadronic tau candidates (with opposite net charge) are considered as $H \to \tau^+\tau^-$ decays. Further separation of the signal and background events is achieved using a BDT classifier based on the properties of the tau candidates and global event properties. The seventeen input discriminating variables are: the total p_T of the full event; the event thrust; the thrust and oblateness of the $\tau^+\tau^-$ system; the thrust and oblateness of the quark system; the sum of the transverse momenta of both τ candidates and of the quark jets; the cosines of the polar angle of both τ candidates; the invariant mass of the $\tau^+\tau^-$ system; the invariant mass of the quark system; the angle between the two τ candidates; the angle between the two quark jets; the polar angle of the missing momentum vector; the azimuthal angle between the two τ candidates; the azimuthal angle between the two

Process	σ/fb	$\varepsilon_{\text{presel}}$	ε_{BDT}	N_{BDT}
$e^+e^- \to HZ; H \to \tau^+\tau^-, Z \to q\bar{q}$	5.8	X %	X %	312
$e^+e^- \to HZ; H \to X, Z \to \tau^+\tau^-$	4.6	X %	X %	9
$e^+e^- \to qq\tau\tau$(non-Higgs)	70	X %	X %	117
$e^+e^- \to qq\tau\tau\nu\nu$	1.6	X %	X %	4
$e^+e^- \to qqqq$	5900	X %	X %	21

Table 11: Cross sections and numbers of preselected and selected events with BDT > 0.08 (see Figure 12) for $e^+e^- \to HZ(H \to \tau^+\tau^-, Z \to q\bar{q})$ signal events and the dominant backgrounds at $\sqrt{s} = 350$ GeV assuming an integrated luminosity of 500 fb^{-1}. The contribution from background processes with photons in the initial state is negligible after the event selection.

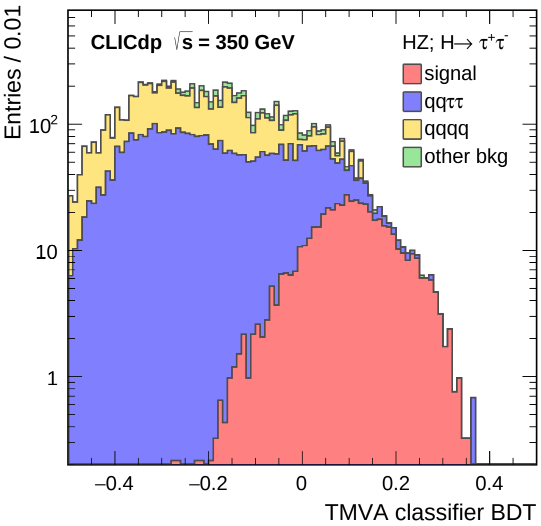

Fig. 12: BDT values for the signal and the main backgrounds for the $H \to \tau^+\tau^-$ event selection at $\sqrt{s}$ =350 GeV.

quark jets; and the visible energy in the event. The resulting BDT distribution for the signal and the main backgrounds is shown in Figure 12. The cross sections and numbers of selected events for the cut on the BDT output maximising the significance for the signal an the dominant background processes are shown in Table 11. A template fit to the BDT output distributions leads to:

$$\Delta[\sigma(HZ) \times BR(H \to \tau^+\tau^-)] = 6.2\,\% .$$

5.2.3 Measurement of the $H \to WW^*$ Branching Ratio

In the event of the Higgs boson decay to a pair of W bosons, only the fully hadronic decay, $H \to WW^* \to q\bar{q}q\bar{q}$ allows the reconstruction of the Higgs invariant mass. Two main

Process	σ/fb	$\varepsilon_{\text{presel}}$	ε_{BDT}	N_{BDT}
$e^+e^- \to HZ;$ $H \to WW^*; Z \to e^+e^-$	0.45	48 %	28 %	63
$e^+e^- \to HZ;$ $H \to X; Z \to \ell^+\ell^-$	4.1	6.0 %	X %	X
$e^+e^- \to q\bar{q}\ell^+\ell^-$	1700	0.25 %	X %	X
$e^+e^- \to q\bar{q}\ell\bar{\nu}$	5900	0.0012 %	X %	X
$e^+e^- \to t\bar{t}$	450	0.012 %	X %	X
$e^+e^- \to WWZ$	10	0.3 %	X %	X
$e^+e^- \to HZ;$ $H \to WW^*; Z \to \mu^+\mu^-$	0.45	87 %	55 %	125
$e^+e^- \to HZ;$ $H \to X; Z \to \ell^+\ell^-$	4.1	78 %	X %	X
$e^+e^- \to q\bar{q}\ell^+\ell^-$	1700	2.0 %	X %	X
$e^+e^- \to q\bar{q}\ell\bar{\nu}$	5900	0.14 %	X %	X
$e^+e^- \to t\bar{t}$	450	0.44 %	X %	X
$e^+e^- \to WWZ$	10	2.9 %	X %	X
$e^+e^- \to HZ;$ $H \to WW^*; Z \to q\bar{q}$	9.2	71 %	29 %	1328
$e^+e^- \to HZ;$ $H \to X; Z \to q\bar{q}$	84	16.5 %	X %	X
$e^+e^- \to q\bar{q}q\bar{q}$	5850	18 %	X %	X
$e^+e^- \to t\bar{t}$	450	19 %	X %	X
$e^+e^- \to WWZ$	10	20 %	X %	X

Table 12: Preselection and selection efficiencies for the ZH signal and most important background processes of the $H \to WW^*$ analysis in all three considered Z decay channels. Numbers of events correspond to 500 fb^{-1} at $\sqrt{s} = 350$ GeV.

types of final states were studied depending on the Z boson decay mode. The semi-leptonic final state consists of four jets from the Higgs decay and two leptons from the Z decay, while the fully hadronic six jet final state results from hadronic decays of both the Higgs and the Z boson.

The first step in the analysis is the search for isolated leptons from the leptonic Z decay. Events containing exactly two isolated leptons are selected as candidates for the semi-leptonic final state, while events with no isolated leptons are selected as candidates for the fully hadronic final state. Events with the number of isolated leptons different than zero or two are not analysed further. The semi-leptonic candidate events are then forced into a four-jet topology, while candidates for the fully hadronic state are forced into a six-jet topology. In addition, all events are forced into a two-jet topology to determine the likelihood values $L^{\text{jet}\,1/2}(b)$, $L^{\text{jet}\,1/2}(c)$ that the jets originate from b or, respectively, c quarks using the LCFIVertex package [41].

For the semi-leptonic event candidates the following preselection criteria are applied: The di-lepton invariant mass is required to be loosely consistent with the Z mass, 80 GeV $< m_{Z\,cand.} < 100$ GeV, the invariant mass $m_{W\,cand.}$ of the pair of jets with the invariant mass closest to m_{W} is required to be loosely consistent with the m_{W}, $45\,\mathrm{GeV} < m_{\mathrm{W}cand.} < 95\,\mathrm{GeV}$, and the invariant mass of the four-jet system consistent with m_{H}, $100\,\mathrm{GeV} < m_{\mathrm{H}cand.} < 140\,\mathrm{GeV}$. The visible energy is required to be in the range $100\,\mathrm{GeV} < E_{\mathrm{vis}} < 300\,\mathrm{GeV}$, the track energy of both isolated leptons is required to be below 150 GeV, and the transverse momentum of the system of four jets, $p_{\mathrm{T}}(\mathrm{H}_{cand.})$, higher than 20 GeV. The event is required to be consistent with a four-jet topology, $\log_{10}(y_{34}) < 4.0$ and $-\log_{10}(y_{23}) < 2.5$. Events in which at least one of jets has a b-tag probability greater than 0.9 are rejected.

After preselection, a BDT classifier is used to separate the signal from the backgrounds. Only the $\mathrm{e}^+\mathrm{e}^- \to \mathrm{q}\overline{\mathrm{q}}\ell^+\ell^-$ process and other Higgs decays were included as backgrounds in the analysis of the semi-leptonic final state. The following discriminating variables are used: $m_{\mathrm{Z}cand.}$, $m_{\mathrm{W}cand.}$, $m_{\mathrm{H}cand.}$, N_{PFO}, $-\log_{10}(y_{12})$, $\log_{10}(y_{23})$, $-\log_{10}(y_{34})$, the event thrust and the polar angle θ_ℓ of one of the two leptons, randomly selected (Comparison of signal and BG distributions of $\theta_{\mathrm{Z}cand.}$ looks better than for the θ_ℓ. Checking whether the numerical results are also improved). The BDT cut value was selected to maximise the significance. The selection efficiencies and expected number of events for the signal and the most important background channels are summarised in Table 12. The statistical uncertainty of the $\sigma(\mathrm{HZ}) \times BR(\mathrm{H} \to \mathrm{WW}^* \to \mathrm{q}\overline{\mathrm{q}}\mathrm{q}\overline{\mathrm{q}})$ measured in the $\mathrm{Z} \to \mathrm{e}^+\mathrm{e}^-$ and the $\mathrm{Z} \to \mu^+\mu^-$ channels is 17.7% and 13.1% respectively for the electron and the muon Z decay channels.

For the fully hadronic final state, the six jets are subdivided into pairs constituting candidates for the Z, W, and the Higgs boson decay by minimisation of the χ^2 function:

$$\chi^2 = \frac{(m_{ij}^2 - m_{\mathrm{W}}^2)}{\sigma_{\mathrm{W}}^2} + \frac{(m_{kl}^2 - m_{\mathrm{Z}}^2)}{\sigma_{\mathrm{Z}}^2} + \frac{(m_{ijmn}^2 - m_{\mathrm{H}}^2)}{\sigma_{\mathrm{H}}^2} \quad (2)$$

Here σ_{W}, and σ_{H} are the widths of the W and H mass peaks in the semi-leptonic channel, and σ_{Z} the width of the Z mass peak on the sample with both W bosons decaying leptonically, and Z decaying hadronically.

After pairing the jets in this way, the following preselection criteria are applied: $m_{\mathrm{Z}cand.} > 40\,\mathrm{GeV}$, $p_{\mathrm{T}}(\mathrm{H}_{cand.}) > 60\,\mathrm{GeV}$, $N_{\mathrm{PFO}} > 50$, $-\log_{10}(y_{12}) < 2.0$, $-\log_{10}(y_{23}) < 2.6$, $-\log_{10}(y_{34}) < 3.0$, $-\log_{10}(y_{45}) < 3.5$, $-\log_{10}(y_{56}) < 4.0$, $E_{\mathrm{vis}} > 250\,\mathrm{GeV}$, $L^{\mathrm{jet2}}(\mathrm{b}) < 0.90$.

After preselection, a BDT classification is performed to separate signal from background. Only three types of background have significant cross section after the preselection: $\mathrm{e}^+\mathrm{e}^- \to \mathrm{q}\overline{\mathrm{q}}\mathrm{q}\overline{\mathrm{q}}$, $\mathrm{e}^+\mathrm{e}^- \to \mathrm{t}\overline{\mathrm{t}}$ and other Higgs decays. The following discriminating variables are used: $m_{\mathrm{Z}cand.}$, $m_{\mathrm{W}cand.}$, $m_{\mathrm{W}^*cand.}$, $m_{\mathrm{H}cand.}$, N_{PFO}, $-\log_{10}(y_{12})$, $\log_{10}(y_{23})$, $-\log_{10}(y_{34})$, $-\log_{10}(y_{45})$, $\log_{10}(y_{56})$, $-\log_{10}(y_{67})$, $p_{\mathrm{T}}(\mathrm{H}_{cand.})$, total visible energy of the event E_{vis}, thrust, sphericity, aplanarity, the angle between the jets constituting the W candidate, the angle between the jets constituting the Z candidate, and likelihood values from b- and c-tagging algorithms applied to the six-jet topology. The BDT cut value was selected to maximise the significance. The selection efficiencies and expected number of events for the signal and the most important background channels are summarised in Table 12. The statistical uncertainty of the $\sigma(\mathrm{HZ}) \times BR(\mathrm{H} \to \mathrm{WW}^* \to \mathrm{q}\overline{\mathrm{q}}\mathrm{q}\overline{\mathrm{q}})$ measured in the hadronic Z decay channel is 5.9%.

Results for the statistical uncertainty on the cross section times branching ratio of the decay $\mathrm{H} \to \mathrm{WW}^*$ are given in Table 13.

$\mathrm{H} \to \mathrm{WW}^* \to \mathrm{q}\overline{\mathrm{q}}\mathrm{q}\overline{\mathrm{q}}$	$\mathrm{Z} \to \mathrm{e}^+\mathrm{e}^-$	$\mathrm{Z} \to \mu^+\mu^-$	$\mathrm{Z} \to \mathrm{q}\overline{\mathrm{q}}$
$\sigma \times BR$	0.453 fb	0.454 fb	9.16
Signal efficiency	27.9 %	55.0 %	29.0 %
Signal events after selection	63	125	1328
Statistical uncertainty	17.7 %	13.1 %	5.9 %

Table 13: The statistical uncertainties on the cross section times branching ratio of the decay $\mathrm{H} \to \mathrm{WW}^*$, given for the three types of final states. An integrated luminosity of $500\,\mathrm{fb}^{-1}$ is assumed.

6 WW-fusion at $\sqrt{s} > 1\,\mathrm{TeV}$

This section presents all relevant measurements of the Higgs decays from the WW-fusion process at CLIC with centre-of-mass energies of 1.4 TeV and 3 TeV. The Higgs self-coupling measurement, which is also accessed in WW-fusion production, is discussed in Section 9. The cross section of the Higgs production via the vector boson fusion process $\mathrm{e}^+\mathrm{e}^- \to \mathrm{H}\nu_{\mathrm{e}}\overline{\nu}_{\mathrm{e}}$ scales with $\log(s)$ and becomes the dominating Higgs production process in $\mathrm{e}^+\mathrm{e}^-$ collisions with $\sqrt{s} > 500\,\mathrm{GeV}$. The respective cross sections for $\mathrm{e}^+\mathrm{e}^- \to \mathrm{H}\nu_{\mathrm{e}}\overline{\nu}_{\mathrm{e}}$ at $\sqrt{s} = 350\,\mathrm{GeV}$, 1.4 TeV and 3 TeV are approximately 93 fb, 244 fb and 415 fb. The relatively large cross sections at the higher energies allow the Higgs decay modes to be probed with high statistical precision and provide access to rarer Higgs decays, such as $\mathrm{H} \to \mu^+\mu^-$.

Since WW-fusion $\mathrm{e}^+\mathrm{e}^- \to \mathrm{H}\nu_{\mathrm{e}}\overline{\nu}_{\mathrm{e}}$ proceeds through the t-channel, the Higgs boson is typically boosted along the beam direction and the presence of neutrinos in the final state results in significant missing p_{T}. Because of the missing transverse and longitudinal momentum, the experimental signatures for $\mathrm{H}\nu_{\mathrm{e}}\overline{\nu}_{\mathrm{e}}$ production are relatively well separated from most SM backgrounds. At $\sqrt{s} = 350\,\mathrm{GeV}$, the main SM background processes are two- and four-fermion production, $\mathrm{e^+e^-} \to 2f$ and $\mathrm{e^+e^-} \to 4f$. At higher energies beamstrahlung becomes increasingly important, related to the real and quasi-real beamstrahlung photons. The first effect is the presence of backgrounds from $\gamma\gamma$ and $\gamma\mathrm{e}^\pm$ hard interactions, resulting in additional background processes. The second effect is the pile-up of relatively soft $\gamma\gamma \to$ hadrons events with the primary interaction, although this background of relatively low-p_T particles is largely mitigated through the timing cuts and jet finding strategy outlined in Section 4.

6.1 $\mathrm{H} \to \mathrm{b\bar{b}}, \mathrm{c\bar{c}}, \mathrm{gg}$

To be incorporated when finalised.

6.2 $\mathrm{H} \to \tau^+\tau^-$

The sensitivity for the measurement of $\sigma(\mathrm{e^+e^-} \to \mathrm{H}\nu_\mathrm{e}\bar{\nu}_\mathrm{e}) \times BR(\mathrm{H} \to \tau^+\tau^-)$ at CLIC was studied using the CLIC_ILD detector model and centre-of-mass energies of 1.4 TeV and 3 TeV. The experimental signature is two relatively high energy τ leptons plus missing energy. For a SM Higgs with a mass of 126 GeV, $BR(\mathrm{H} \to \tau^+\tau^-) = 6.15\,\%$, resulting in an effective signal cross section of 15.1 fb at $\sqrt{s} = 1.4\,\mathrm{TeV}$ and 25.5 fb at $\sqrt{s} = 3\,\mathrm{TeV}$.

The experimental signature is two relatively high-momenta narrow 'jets' from the two tau decays and significant missing transverse and longitudinal momenta. The analysis is restricted to hadronic τ decays, which are identified using the TauFinder algorithm, as described in Section 5.2.2. The TauFinder algorithm parameters were tuned using the $\mathrm{H} \to \tau^+\tau^-$ signal events and $\mathrm{e^+e^-} \to \mathrm{q\bar{q}}\nu\bar{\nu}$ background events. The working point has a τ selection efficiency of 70% (60%) with a quark jet fake rate of 7% (9%) at $\sqrt{s} = 1.4\,\mathrm{TeV}$ ($\sqrt{s} = 3\,\mathrm{TeV}$). All relevant SM backgrounds are taken into account, including $\gamma\gamma$ and $\gamma\mathrm{e}^\pm$ collisions. The most significant backgrounds are $\mathrm{e^+e^-} \to \tau^+\tau^-\nu\bar{\nu}$, $\mathrm{e}\gamma \to \tau^+\tau^-\mathrm{e}$ and $\gamma\gamma \to \tau^+\tau^-\nu\bar{\nu}$. The latter two processes become increasingly important at higher $\sqrt{s}$, due to the increasing number of beamstrahlung photons.

The event preselection requires two identified τ leptons, both of which must be within the polar angle range $15^\circ < \theta(\tau) < 165^\circ$ and have $p_\mathrm{T}(\tau) > 25\,\mathrm{GeV}$. To reject back-to-back or nearby tau leptons, the angle between the two tau candidates must satisfy $29^\circ < \Delta\theta(\tau\tau) < 177^\circ$. The visible invariant mass $m(\tau\tau)$ and the visible transverse mass $m_\mathrm{T}(\tau\tau)$ of the two tau candidates must satisfy $45\,\mathrm{GeV} < m(\tau\tau) < 130\,\mathrm{GeV}$ and $m_\mathrm{T}(\tau\tau) < 20\,\mathrm{GeV}$. Finally the event thrust must be less than 0.99.

Process	σ/fb	$\varepsilon_\mathrm{presel}$	ε_BDT	N_BDT
$\mathrm{e^+e^-} \to \mathrm{H}\nu_\mathrm{e}\bar{\nu}_\mathrm{e}; \mathrm{H} \to \tau^+\tau^-$	15.0	9.3%	38.9%	814
$\mathrm{e^+e^-} \to \tau^+\tau^-\nu\bar{\nu}$	38.5	5.0%	18.0%	528
$\mathrm{e}^\pm\gamma \to \tau^+\tau^-\mathrm{e}^\pm$	2580	1.9%	0.075%	45
$\gamma\gamma \to \tau^+\tau^-(\nu\bar{\nu}\text{ or }\ell^-\ell^+)$	128.1	2.7%	2.25%	79

Table 14: Preselection and selection efficiencies for the signal and most important background processes in the $\mathrm{H} \to \tau^+\tau^-$ analysis. Numbers of events correspond to $1.5\,\mathrm{ab}^{-1}$ at $\sqrt{s} = 1.4\,\mathrm{TeV}$. The cross sections for the backgrounds include cuts on the kinematic properties of the tau lepton pair applied on generator level. The preselection efficiencies include the reconstruction of two hardonic tau lepton decays per event.

Process	σ/fb	$\varepsilon_\mathrm{presel}$	ε_BDT	N_BDT
$\mathrm{e^+e^-} \to \mathrm{H}\nu_\mathrm{e}\bar{\nu}_\mathrm{e}; \mathrm{H} \to \tau^+\tau^-$	25.5	9.2%	23.2%	787
$\mathrm{e^+e^-} \to \tau^+\tau^-\nu\bar{\nu}$	39.2	8.3%	11.1%	498
$\mathrm{e}^\pm\gamma \to \tau^+\tau^-\mathrm{e}^\pm$	2770	2.8%	0.26%	246
$\gamma\gamma \to \tau^+\tau^-(\nu\bar{\nu}\text{ or }\ell^-\ell^+)$	218	2.8%	0.14%	9

Table 15: Preselection and selection efficiencies for the signal and most important background processes in the $\mathrm{H} \to \tau^+\tau^-$ analysis. Numbers of events correspond to $2\,\mathrm{ab}^{-1}$ at $\sqrt{s} = 3\,\mathrm{TeV}$. The cross sections for the backgrounds include cuts on the kinematic properties of the tau lepton pair applied on generator level. The preselection efficiencies include the reconstruction of two hardonic tau lepton decays per event.

Events passing the preselection are classified as either signal or SM background using a BDT classifier. The kinematic variables used in the classifier are $m(\tau\tau)$, $m_\mathrm{T}(\tau\tau)$, event shape variables (such as thrust and oblateness), the missing p_T, the polar angle of the missing momentum vector $|\cos\theta_\mathrm{miss}|$ and the total reconstructed energy excluding the Higgs candidate. The event selection for the signal and the most relevant background processes is summarised in Table 14 for $\sqrt{s} = 1.4\,\mathrm{TeV}$ and in Table 15 for $\sqrt{s} = 3\,\mathrm{TeV}$. Rather than applying a simple cut, the full BDT shape information is utilised in a template fit. The resulting statistical uncertainties for $1.5\,\mathrm{ab}^{-1}$ at $\sqrt{s} = 1.4\,\mathrm{TeV}$ and $2.0\,\mathrm{ab}^{-1}$ at $\sqrt{s} = 3\,\mathrm{TeV}$ are:

$$\Delta[\sigma \times BR(\mathrm{H} \to \tau^+\tau^-)] = 4.2\,\% \text{ at } 1.4\,\mathrm{TeV},$$
$$\Delta[\sigma \times BR(\mathrm{H} \to \tau^+\tau^-)] = 4.4\,\% \text{ at } 3\,\mathrm{TeV}.$$

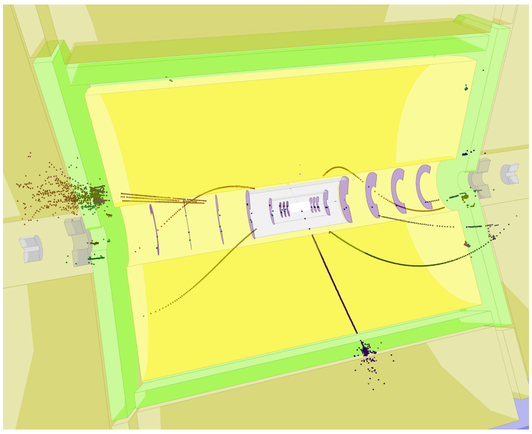

Fig. 13: Event display of a $\mathrm{H} \rightarrow \tau^+\tau^-$ at event at $\sqrt{s} = 1.4\,\mathrm{TeV}$. A 1-prong tau decay is visible in the central part of the detector. The other tau lepton decays to three charged particles and is reconstructed in the forward direction. In addition, a few soft particles from beam-induced backgrounds are visible.

Process	σ/fb	$\varepsilon_{\mathrm{presel}}$	$\varepsilon_{\mathscr{L}>0.35}$	$N_{\mathscr{L}>0.35}$
$\mathrm{e^+e^-} \rightarrow \mathrm{q\bar{q}}\nu\bar{\nu}$	788.0	4.6 %	0.2 %	2225
$\mathrm{e^+e^-} \rightarrow \mathrm{q\bar{q}q\bar{q}}\ell\nu$	115.3	0.1 %	<0.1 %	43
$\mathrm{e^+e^-} \rightarrow \mathrm{q\bar{q}q\bar{q}}\nu\bar{\nu}$	24.7	0.8 %	0.4 %	130
$\gamma\mathrm{e^+}(\gamma\mathrm{e^-}) \rightarrow \mathrm{q\bar{q}q\bar{q}}\nu$	254.3	1.8 %	0.4 %	1389
$\mathrm{H}\nu_e\bar{\nu}_e$	244.1	14.61 %	3.0 %	11101
$\mathrm{H} \rightarrow \mathrm{WW^*} \rightarrow \mathrm{q\bar{q}q\bar{q}}$		32.4 %	18.1 %	7518
$\mathrm{H} \rightarrow \mathrm{WW^*} \rightarrow \mathrm{q\bar{q}}\ell\nu$		4.4 %	0.6 %	253
$\mathrm{H} \rightarrow \mathrm{b\bar{b}}$		1.9 %	0.4 %	774
$\mathrm{H} \rightarrow \mathrm{c\bar{c}}$		8.1 %	2.1 %	209
$\mathrm{H} \rightarrow \mathrm{gg}$		19.1 %	7.1 %	1736
$\mathrm{H} \rightarrow \mathrm{ZZ}$		12.0 %	5.0 %	556
$\mathrm{H} \rightarrow$ other		0.7 %	0.2 %	55

Table 16: Summary of the $\mathrm{H} \rightarrow \mathrm{WW^*}$ event selection at $\sqrt{s} = 1.4\,\mathrm{TeV}$, giving the raw cross sections, preselection efficiency, overall selection efficiency for a likelihood cut of $\mathscr{L} > 0.35$ and the expected numbers of events passing the event selection for an integrated luminosity of $1.5\,\mathrm{ab}^{-1}$.

6.3 $\mathrm{H} \rightarrow \mathrm{WW^*}$

The signature for $\mathrm{H} \rightarrow \mathrm{WW^*}$ decays in $\mathrm{e^+e^-} \rightarrow \mathrm{H}\nu_e\bar{\nu}_e$ is less clearly defined than for $\mathrm{H} \rightarrow \mathrm{q\bar{q}}$. There is still missing p_T from the $\nu_e\bar{\nu}_e$ system, but the final-state topology will depend on the WW decay modes. However, the invariant mass of the Higgs boson in $\mathrm{H} \rightarrow \mathrm{WW^*}$ decays can be reconstructed for fully-hadronic decays alone, $\mathrm{WW} \rightarrow \mathrm{q\bar{q}q\bar{q}}$. Since $m_\mathrm{H} < 2m_\mathrm{W}$, one of the W-bosons will be off mass-shell. Consequently the experimental signature for $\mathrm{H}\nu_e\bar{\nu}_e$ production with $\mathrm{H} \rightarrow \mathrm{WW^*} \rightarrow \mathrm{q\bar{q}q\bar{q}}$ is a four-jet final state with missing p_T and a total invariant mass consistent with the Higgs mass, where one pair of jets has a mass consistent with m_W. There are two main sources of potential backgrounds. The first being other Higgs decays, in particular $\mathrm{H} \rightarrow \mathrm{b\bar{b}}$, $\mathrm{H} \rightarrow \mathrm{c\bar{c}}$ and $\mathrm{H} \rightarrow \mathrm{gg}$, which produce hadronic final states with an invariant mass consistent with the Higgs mass; here QCD radiation in the parton shower can lead to a four-jet topology. The second main source of potential background comes from $\mathrm{e^+e^-} \rightarrow \mathrm{q\bar{q}}\nu\bar{\nu}$ and $\gamma\mathrm{e^\pm} \rightarrow \mathrm{q\bar{q}q\bar{q}}\nu$.

The $\mathrm{H} \rightarrow \mathrm{WW^*}$ event selection has been studied at $\sqrt{s} = 1.4\,\mathrm{TeV}$. It proceeds in two separate stages: a set of preselection cuts designed to reduce the backgrounds from large cross section processes such as $\mathrm{e^+e^-} \rightarrow \mathrm{q\bar{q}}$ and $\mathrm{e^+e^-} \rightarrow \mathrm{q\bar{q}q\bar{q}}$; followed by a likelihood-based multivariate event selection. The preselection variables are formed by forcing each event into four jets using the Durham jet finder. Of the three possible jet associations with candidate W bosons, (12)(34), (13)(24) or (14)(23), the one giving a di-jet invariant mass closest to m_W is selected. The preselection cuts require: $\log_{10}(y_{23}) > -2.75$ and $\log_{10}(y_{34}) > -3.5$; visible energy, $125\,\mathrm{GeV} < E_\mathrm{vis} < 600\,\mathrm{GeV}$; missing transverse momentum, $p_\mathrm{T} > 65\,\mathrm{GeV}$; $\cos\theta_\mathrm{miss} < 0.99$; one candidate on-shell W boson, $50\,\mathrm{GeV} < m_\mathrm{W1} < 95\,\mathrm{GeV}$; one off-shell W boson, $m_\mathrm{W2} < 65\,\mathrm{GeV}$; total invariant mass consistent with a Higgs decay, $90\,\mathrm{GeV} < m_\mathrm{H} < 150\,\mathrm{GeV}$; and the absence of a high-energy electron or muon, $E_\mathrm{lept} < 30\,\mathrm{GeV}$. In addition, in order to reject $\mathrm{H} \rightarrow \mathrm{b\bar{b}}$ decays, the event is forced into a two-jet topology and flavour-tagging is applied to the two jets. Events where one (or both) jets have a b-tag probability, b_1 or b_2 of greater than 0.95 are rejected as part of the preselection. The cross sections and preselection efficiencies for the signal and main background processes are listed in Table 16. After the preselection, the main backgrounds are $\mathrm{e^+e^-} \rightarrow \mathrm{q\bar{q}}\nu\bar{\nu}$, $\gamma\mathrm{e^\pm} \rightarrow \mathrm{q\bar{q}q\bar{q}}\nu$ and other Higgs decay modes, predominantly $\mathrm{H} \rightarrow \mathrm{b\bar{b}}$ and $\mathrm{H} \rightarrow \mathrm{gg}$.

A relative likelihood selection is used to classify all events passing the preselection cuts. Five event categories are considered $\mathrm{H} \rightarrow \mathrm{WW^*}$ signal; $\mathrm{H} \rightarrow \mathrm{b\bar{b}}$; $\mathrm{H} \rightarrow \mathrm{gg}$; $\mathrm{e^+e^-} \rightarrow \mathrm{q\bar{q}}\nu\bar{\nu}$ and $\gamma\mathrm{e^\pm} \rightarrow \mathrm{q\bar{q}q\bar{q}}\nu$. The relative likelihood of an event being signal is defined as

$$\mathscr{L} = \frac{L(\mathrm{H} \rightarrow \mathrm{WW^*})}{L(\mathrm{H} \rightarrow \mathrm{WW^*}) + L_1 + L_2 + L_3 + L_4},$$

where the L_i represents the likelihood for the four background categories above. The absolute likelihood L for each event type is formed from normalised probability distributions $P_i(x_i)$ of the N likelihood discriminating variables x_i for that event type. For example, the distribution of the reconstructed Higgs mass for all events passing the preselection is shown in Figure 14, where it can be seen that good separation between signal and background is achievable. The

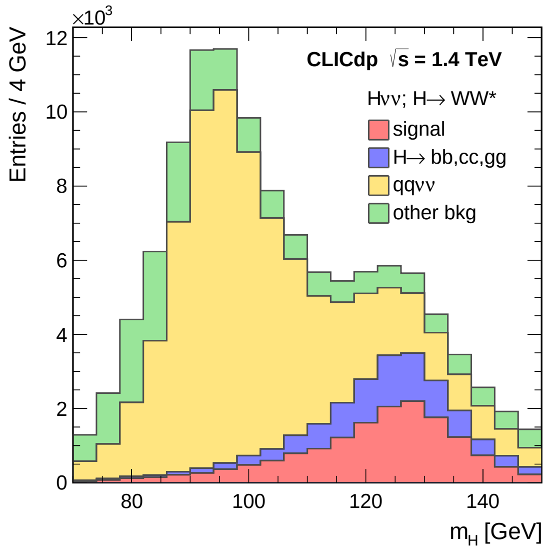

Fig. 14: The reconstructed Higgs mass distribution for events passing the preselected cuts. The numbers of entries correspond to the SM expectation for $1.5\,\mathrm{ab}^{-1}$ of data at $\sqrt{s} = 1.4\,\mathrm{TeV}$.

discriminating variables are: the 2D distribution of reconstructed invariant masses m_{H} and m_{W}; the 2D distribution of jet-finding y-cut values y_{23}, y_{34}; and 2D distribution of b-tag probabilities b_1 and b_2. The use of 2D distributions accounts for the most significant correlations between the likelihood variables. The selection efficiencies and expected numbers of events for the signal dominated region, $\mathscr{L} > 0.35$, are listed in Table 16.

The expected precision on $BR(\mathrm{H} \to \mathrm{WW}^*)$ is extracted from a fit to the likelihood distribution. Given the non-negligible backgrounds from other Higgs decays, it is necessary to simultaneously fit the different components. A χ^2 fit to the expected $\mathscr{L}$ distribution is performed by scaling independently five components: the $\mathrm{H} \to \mathrm{WW}^*$ signal; the $\mathrm{H} \to \mathrm{b\bar{b}}$, $\mathrm{H} \to \mathrm{c\bar{c}}$ and $\mathrm{H} \to \mathrm{gg}$ backgrounds; and all other backgrounds (dominated by $\mathrm{q\bar{q}}\nu\bar{\nu}$ and $\mathrm{q\bar{q}q\bar{q}}\nu$). The constraints on the $\mathrm{H} \to \mathrm{b\bar{b}}$, $\mathrm{H} \to \mathrm{c\bar{c}}$ and $\mathrm{H} \to \mathrm{gg}$ branching ratios, as described in Section 6.1, are implemented by modifying the χ^2 function to include penalty terms,

$$\chi^2 \to \chi^2 + \frac{(s_{\mathrm{b\bar{b}}}-1)^2}{\sigma^2_{\mathrm{b\bar{b}}}} + \frac{(s_{\mathrm{c\bar{c}}}-1)^2}{\sigma^2_{\mathrm{c\bar{c}}}} + \frac{(s_{\mathrm{gg}}-1)^2}{\sigma^2_{\mathrm{gg}}} + \frac{(s_{\mathrm{ZZ}^*}-1)^2}{\sigma^2_{\mathrm{ZZ}^*}} + \frac{(b-1)^2}{\sigma^2_b}\,.$$

Here, for example, s_{gg} is the amount by which the $\mathrm{H} \to \mathrm{gg}$ complement is scaled in the fit and σ_{gg} is the expected statistical error on $BR(\mathrm{H} \to \mathrm{gg})$ from the analysis of Section 6.1. The background from $\mathrm{H} \to \mathrm{ZZ}^*$ scales with the $\mathrm{H} \to \mathrm{WW}^*$ signal as $g^2_{\mathrm{HZZ}}/g^2_{\mathrm{HWW}}$, which is determined to 1.0 % (number to be updated when other results finalised) from the measured ratio of $\sigma(\mathrm{HZ} \to \mathrm{b\bar{b}})$ to $\sigma(\mathrm{H}\nu_e\bar{\nu}_e \to \mathrm{b\bar{b}}\nu_e\bar{\nu}_e)$. The systematic uncertainty in the non-H background, denoted by b, is taken to be 1 %. The resulting statistical uncertainty on the $\mathrm{H} \to \mathrm{WW}^*$ branching ratio is

$$\Delta[\sigma(\mathrm{H}\nu_e\bar{\nu}_e) \times BR(\mathrm{H} \to \mathrm{WW}^*)] = 1.5\,\%\,.$$

Process	σ/fb	$\varepsilon_{\mathrm{presel}}$	$\varepsilon_{\mathrm{BDT}}$	N_{BDT}
$\mathrm{e^+e^-} \to \mathrm{H}\nu_e\bar{\nu}_e; \mathrm{H} \to \mathrm{ZZ}^* \to \mathrm{q\bar{q}}\ell\ell$	X	X %	X %	X
...				

Table 17: Preselection and selection efficiencies for the signal and most important background processes in the $\mathrm{H} \to \mathrm{ZZ}^*$ analysis. Numbers of events correspond to $1.5\,\mathrm{ab}^{-1}$ at $\sqrt{s} = 1.4\,\mathrm{TeV}$. Not yet referenced in text.

6.4 $\mathrm{H} \to \mathrm{ZZ}^*$

In the $\mathrm{e^+e^-} \to \mathrm{H}\nu_e\bar{\nu}_e$ process, $\mathrm{H} \to \mathrm{ZZ}^*$ decays can be cleanly identified in the fully hadronic ($\mathrm{ZZ}^* \to \mathrm{q\bar{q}q\bar{q}}$) and semi-leptonic ($\mathrm{ZZ}^* \to \mathrm{qq}\ell\ell$) final states. In both cases the experimental signature is four final-state fermions (jets or charged leptons) with a total invariant mass consistent with m_{H}, the mass of one pair of fermions consistent with m_{Z} and missing momentum from the $\nu_e\bar{\nu}_e$ system. The event selection has been studied at $\sqrt{s} = 1.4\,\mathrm{TeV}$ using the CLIC_ILD detector model. Because of the small SM branching ratio for $\mathrm{H} \to \mathrm{ZZ}^*$, the expected cross sections are small: 3.45 fb for $\mathrm{ZZ}^* \to \mathrm{q\bar{q}q\bar{q}}$ and 0.995 fb for $\mathrm{ZZ}^* \to \mathrm{qq}\ell\ell$. Because of the large background from $\mathrm{H} \to \mathrm{WW}^* \to \mathrm{q\bar{q}q\bar{q}}$, only the $\mathrm{ZZ}^* \to \mathrm{qq}\ell\ell$ final state is considered here.

The analysis is performed in several steps. In the first step a search for isolated leptons is performed. For electrons and muons, individual PFO are required to pass an optimised two-dimensional cut on track energy E_{track} vs. cone energy E_{cone}, where E_{cone} represents the sum of energies of other PFO within 5.7° around the PFO under consideration. In addition, an impact parameter smaller than 0.02 mm is required. With these criteria, 87 % of electrons and muons from Z decays are correctly identified. The muons are distinguished from the electrons without overlap using the ratio of energy deposits in ECAL and HCAL. The τ leptons are identified using the TauFinder algorithm described in Section 5.2.2, with the requirement $p_{\mathrm{T}} > 10\,\mathrm{GeV}$ for the seed and $p_{\mathrm{T}} > 4\,\mathrm{GeV}$ for all other tracks within the search cone of 8.6° half-angle. The invariant mass of the combined four-vector of all tracks within the search cone is required to be smaller than 2 GeV. In addition, it is required that less than 5 PFO are found in the *isolation ring* between 8.6° and 20° around the seed, and the total energy of all PFO in the isolation ring is smaller than 3 GeV. The efficiency for reconstructing τ pairs from Z decays with this algorithm is 37 %.

After separating the isolated leptons, the remaining PFO in the event are forced into a two-jet topology. The LCFIVERTEX package is then used to determine the likelihood values $L^{\mathrm{jet}\,1/2}(\mathrm{b}), L^{\mathrm{jet}\,1/2}(\mathrm{c})$ that the jets originate from b or, respectively, c quark.

Events containing exactly two isolated charged leptons are classified as either background or signal using a BDT classifier trained on 17 discriminating variables, m_{H}, m_{Z}, m_{Z^*}, $-\log(y_{34})$, $-\log(y_{23})$, $-\log(y_{12})$, $L^{\mathrm{jet1}}(\mathrm{b})$, $L^{\mathrm{jet2}}(\mathrm{b})$, $L^{\mathrm{jet1}}(\mathrm{c})$, $L^{\mathrm{jet2}}(\mathrm{c})$, E_{vis}, $p_{\mathrm{T},miss}$, θ_{H}, $m_{\ell\ell}$, $m_{\mathrm{q\bar{q}}}$, $(E_{\mathrm{vis}} - E_{\mathrm{H}})$, N_{PFO}. The BDT cut value was selected to maximise the significance, giving an efficiency of 30.4 % for the signal. The overall reduction of background is shown in Figure 15.

Results of the statistical uncertainty on the cross section times branching ratio of the decay $\mathrm{H} \to \mathrm{ZZ}^* \to \mathrm{qq}\ell\ell$ are given in Table 18.

	$\mathrm{H} \to \mathrm{ZZ}^* \to \mathrm{qq}\ell\ell$
Signal cross section	0.995 fb
Signal efficiency	30.4 %
Signal events after final selection	454
Statistical uncertainty $\sigma \times BR$	5.6 %

Table 18: The statistical uncertainty on the cross section times branching ratio of the decay $\mathrm{H} \to \mathrm{ZZ}^* \to \mathrm{qq}\ell\ell$. An integrated luminosity of 1.5 ab^{-1} is assumed.

6.5 $\mathrm{H} \to \gamma\gamma$

The measurement of the $\mathrm{H} \to \gamma\gamma$ decay played a central role in the discovery of the Higgs boson at the LHC [42, 43]. In the SM, this decay is induced via loop diagrams, dominated by heavy charged particles, mostly W bosons and t quarks. For BSM scenarios, other heavy charged particles can appear in the loops, modifying the expected effective $\mathrm{H} \to \gamma\gamma$ branching ratio. The sensitivity for the measurement of $BR(\mathrm{H} \to \gamma\gamma)$ at CLIC has been studied using the CLIC_SiD detector model for $\sqrt{s} = 1.4\,\mathrm{TeV}$ and an integrated luminosity of 1.5 ab^{-1}. The SM branching ratio for $m_{\mathrm{H}} = 126\,\mathrm{GeV}$ is 0.23% which results in approximately 840 signal events. The experimental signature for $\mathrm{e}^+\mathrm{e}^- \to (\mathrm{H} \to \gamma\gamma)\nu_{\mathrm{e}}\bar{\nu}_{\mathrm{e}}$ is two high p_{T} photons with $m(\gamma\gamma) \sim m_{\mathrm{H}}$ and missing momentum from the $\nu_{\mathrm{e}}\bar{\nu}_{\mathrm{e}}$ system. All relevant SM background processes with one or two photons in the final state have been considered. In addition to the photons from the hard interaction, the MC samples include additional ISR and FSR photons.

Process	σ/fb	$\varepsilon_{\mathrm{presel}}$	$\varepsilon_{\mathrm{BDT}}$	N_{BDT}
$\mathrm{e}^+\mathrm{e}^- \to \mathrm{H}\nu_{\mathrm{e}}\bar{\nu}_{\mathrm{e}}, \mathrm{H} \to \gamma\gamma$	0.56	84.9 %	40.4 %	337
$\mathrm{e}^+\mathrm{e}^- \to \nu\bar{\nu}\gamma$	29.5	34.2 %	2.5 %	1110
$\mathrm{e}^+\mathrm{e}^- \to \nu\bar{\nu}\gamma\gamma$	17.3	31.0 %	2.6 %	688
$\mathrm{e}^+\mathrm{e}^- \to \gamma\gamma$	27.2	19.8 %	0.14 %	55
$\mathrm{e}^+\mathrm{e}^- \to \mathrm{e}^+\mathrm{e}^-\gamma$	289.0	9.2 %	0.06 %	265
$\mathrm{e}^+\mathrm{e}^- \to \mathrm{e}^+\mathrm{e}^-\gamma\gamma$	12.6	5.2 %	0.01 %	2
$\mathrm{e}^+\mathrm{e}^- \to \mathrm{q\bar{q}}\gamma$	67.0	0.8 %	0.0 %	0
$\mathrm{e}^+\mathrm{e}^- \to \mathrm{q\bar{q}}\gamma\gamma$	16.6	1.4 %	0.01 %	2

Table 19: Signal and relevant background processes used in the $\mathrm{H} \to \gamma\gamma$ analysis. Additional photons from ISR and FSR are present in each sample. Numbers of events correspond to 1.5 ab^{-1} at $\sqrt{s} = 1.4\,\mathrm{TeV}$. Not yet referenced in text.

The following preselection cuts are applied to restrict the analysis to relevant events. At least two reconstructed photons each with energy $E_\gamma > 15\,\mathrm{GeV}$ and $p_{\mathrm{T}} > 10\,\mathrm{GeV}$ are required. The two highest energy photons passing these requirements are used to form the H candidate and the preselection requires an invariant mass consistent with m_{H}, $115\,\mathrm{GeV} < m(\gamma\gamma) < 140\,\mathrm{GeV}$, and the highest energy photon in the event is required to have $p_{\mathrm{T}} > 40\,\mathrm{GeV}$. In addition, to remove contributions from FSR, both photons are required to be isolated with no reconstructed particle with $p_{\mathrm{T}} > 5\,\mathrm{GeV}$ within a cone of half-angle 500 mrad centred on the photon. Furthermore, the remaining reconstructed energy after excluding the Higgs candidate has to be below 250 GeV. The selected cross sections for the signal and the main backgrounds after the preselection cuts are listed in Table 19. At this stage in the event selection the background dominates.

The signal and background events are classified using a BDT. In total, 13 variables are used to distinguish the signal from the backgrounds including the mass of the Higgs candidate shown in Figure 16, the energy, transverse momenta and polar angles of the Higgs candidate and the two individual photons, the remaining reconstructed energy excluding the Higgs candidate. For the optimal BDT cut, the total signal selection efficiency is 40.4%, corresponding to approximately 340 selected signal events in 1.5 ab^{-1}. The selected cross sections for signal and the main backgrounds are listed in Table 19, leading to a statistical uncertainty of

$$\Delta[\sigma(\mathrm{e}^+\mathrm{e}^- \to \mathrm{H}\nu_{\mathrm{e}}\bar{\nu}_{\mathrm{e}}) \times BR(\mathrm{H} \to \gamma\gamma)] = 14.7\,\%\,.$$

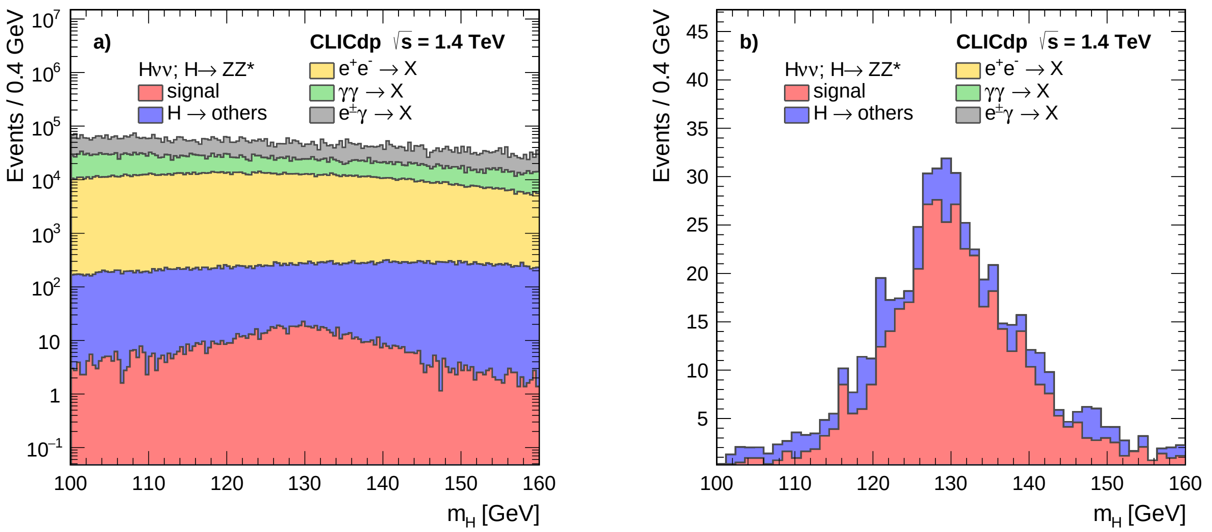

Fig. 15: The distribution of the reconstructed Higgs mass of $\mathrm{H} \to \mathrm{ZZ}^* \to \mathrm{q}\bar{\mathrm{q}}\ell^+\ell^-$ events and the different backgrounds. a) after the preselection stage, and b) after the full event selection including a cut on the BDT classifier.

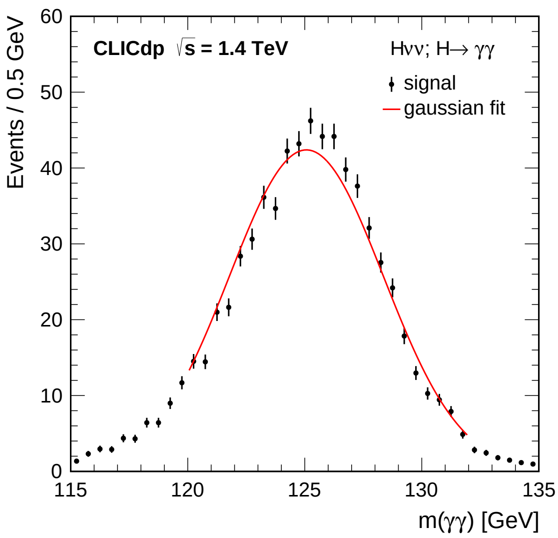

Fig. 16: Invariant mass distribution of $\mathrm{H} \to \gamma\gamma$ events after the preselection requirements for $1.5\,\mathrm{ab}^{-1}$ at $\sqrt{s} = 1.4\,\mathrm{TeV}$. The statistical uncertainties shown correspond to the uncertainties of the simulated sample and are not scaled to a specific integrated luminosity. The fit indicates the average mass resolution in the signal sample with σ = 3.3 GeV. The backgrounds are flat and exceed the signal peak by more than three orders of magnitude after the preselection.

6.6 $\mathrm{H} \to \mathrm{Z}\gamma$

As was the case for $\mathrm{H} \to \gamma\gamma$, at lowest order, the SM decay $\mathrm{H} \to \mathrm{Z}\gamma$ is induced by loops of heavy charged particles. Contributions from BSM particles would lead to deviations from the SM expectation for $BR(\mathrm{H} \to \mathrm{Z}\gamma)$. For $m_{\mathrm{H}} = 126\,\mathrm{GeV}$, the decay $\mathrm{H} \to \mathrm{Z}\gamma$ is expected to have a branching ratio of $BR(\mathrm{H} \to \mathrm{Z}\gamma) = 0.16\%$. The potential to measure $\sigma(\mathrm{e}^+\mathrm{e}^- \to \mathrm{H}\nu_{\mathrm{e}}\bar{\nu}_{\mathrm{e}}) \times BR(\mathrm{H} \to \mathrm{Z}\gamma)$ at CLIC has been studied at $\sqrt{s} = 1.4\,\mathrm{TeV}$ with the CLIC_SiD detector model, where 585 $\mathrm{H} \to \mathrm{Z}\gamma$ events would be expected in $1.5\,\mathrm{ab}^{-1}$ of data. For the purpose of the event selection, only $\mathrm{Z} \to \mathrm{q}\bar{\mathrm{q}}$ and $\mathrm{Z} \to \ell^+\ell^-$ (with $\ell = \mathrm{e}, \mu$) are useful, giving small event samples of 409 $\mathrm{q}\bar{\mathrm{q}}\gamma$, 21 $\mathrm{e}^+\mathrm{e}^-\gamma$ and 21 $\mu^+\mu^-\gamma$ events from $\mathrm{H} \to \mathrm{Z}\gamma$ in $1.5\,\mathrm{ab}^{-1}$ at $\sqrt{s} = 1.4\,\mathrm{TeV}$.

The visible final states of the signal channels $\mathrm{q}\bar{\mathrm{q}}\gamma$ or $\ell^+\ell^-\gamma$ are also produced in several background processes, some of which have much larger cross sections than the signal. In addition to background with photons from the hard process, $\mathrm{e}^+\mathrm{e}^- \to \mathrm{q}\bar{\mathrm{q}}$ or $\mathrm{e}^+\mathrm{e}^- \to \ell^+\ell^-$ events with a FSR or ISR photon can mimic the signal.

The $\mathrm{H} \to \mathrm{Z}\gamma$ event selection requires at least one identified high-p_{T} photon and either two electrons, muons or quarks consistent with a Z decay. The highest energy reconstructed photon in the event is identified. Events are then considered as either $\mathrm{e}^+\mathrm{e}^-\gamma$, $\mu^+\mu^-\gamma$ or $\mathrm{q}\bar{\mathrm{q}}\gamma$ candidates. In the case where a $\mathrm{e}^+\mathrm{e}^-$ or $\mu^+\mu^-$ pair is found, photons nearly collinear with the lepton trajectories (within 0.3°) are combined with the leptons under the assumption that these photons originate from bremsstrahlung. If neither a $\mathrm{e}^+\mathrm{e}^-$ nor a $\mu^+\mu^-$ pair is found, all reconstructed particles except for the photon of highest energy are clustered into two jets assuming that the Z decayed into two quarks, using a jet radius of $R = 1.2$. In all cases, the selected Z decay candidate and the highest energy photon are combined to form the H candidate.

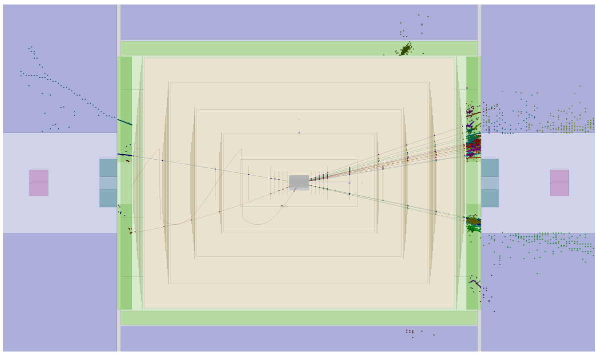

Fig. 17: Display of an $\mathrm{H} \to \mathrm{Z}\gamma \to \mathrm{q}\bar{\mathrm{q}}\gamma$ event at 1.4 TeV. Both jets are visible in the forward directions. The photon creates a cluster in the central part of the electromagnetic calorimeter.

In order to reduce the number of background process events, two selection steps are performed. First, preselection cuts are applied: the Higgs candidate daughter photon and jets, electrons, or muons are only accepted if they have an energy of $E > 20\,\mathrm{GeV}$ and $p_\mathrm{T} > 15\,\mathrm{GeV}$. In the $\mathrm{q}\bar{\mathrm{q}}\gamma$ channel, only jets with at least 5 particles are considered in order to suppress hadronic τ decays. In addition, the reconstructed Z and H masses in the event are required to be consistent with a $\mathrm{H} \to \mathrm{Z}\gamma$ decay. The second step in the event selection is three BDT selections (one for each signal final state). The input variables are the properties of the reconstructed H, Z, and γ such as mass, energy, momentum, and polar angle, event shapes such as sphericity and aplanarity, as well as missing energy distributions and particle multiplicity distributions.

For the optimal BDT cuts statistical significances of 2.2, 0.54 and 0.78 are found for the $\mathrm{q}\bar{\mathrm{q}}\gamma$, $\mathrm{e}^+\mathrm{e}^-\gamma$ and $\mu^+\mu^-\gamma$ channels respectively. The signal selection efficiencies and contributions from the most important backgrounds are summarised in Table 20. When the results from all three channels are combined, the achieved statistical precision is

$$\Delta[\sigma(\mathrm{e}^+\mathrm{e}^- \to \mathrm{H}\nu_\mathrm{e}\bar{\nu}_\mathrm{e}) \times BR(\mathrm{H} \to \mathrm{Z}\gamma)] = 42\,\%,$$

for unpolarised $\mathrm{e}^+\mathrm{e}^-$ collisions at $\sqrt{s} = 1.4\,\mathrm{TeV}$ and $1.5\,\mathrm{ab}^{-1}$ of data. With electron and/or positron polarisation the statistical precision can be increased, for example with 80 % electron polarisation, $\Delta[\sigma(\mathrm{e}^+\mathrm{e}^- \to \mathrm{H}\nu_\mathrm{e}\bar{\nu}_\mathrm{e}) \times BR(\mathrm{H} \to \mathrm{Z}\gamma)] \approx 31\,\%$. Further gains are expected from going to higher centre-of-mass energies, for example, the Higgs production cross section at $\sqrt{s} = 3\,\mathrm{TeV}$ is 70 % higher than at 1.4 TeV.

Process	σ/fb	$\varepsilon_\mathrm{presel}$	ε_BDT	N_BDT
$\mathrm{e}^+\mathrm{e}^- \to \mathrm{H}\nu_\mathrm{e}\bar{\nu}_\mathrm{e}$;				
$\mathrm{H} \to \mathrm{Z}\gamma; \mathrm{Z} \to \mathrm{q}\bar{\mathrm{q}}$	0.27	45.1 %	18.2 %	75
$\mathrm{H} \to \mathrm{Z}\gamma; \mathrm{Z} \to \mathrm{e}^+\mathrm{e}^-$	0.014	38.3 %	17.3 %	4
$\mathrm{H} \to \mathrm{Z}\gamma; \mathrm{Z} \to \mu^+\mu^-$	0.014	53.7 %	24.5 %	5
$\mathrm{e}^+\mathrm{e}^- \to \nu\bar{\nu}\mathrm{q}\bar{\mathrm{q}}\gamma$	37.3	12.3 %	0.9 %	504
$\mathrm{e}^+\mathrm{e}^- \to \nu\bar{\nu}\mathrm{q}\bar{\mathrm{q}}$	121.8	8.4 %	0.2 %	463
$^*\mathrm{e}^\pm\gamma \to \mathrm{e}^\pm\mathrm{q}\bar{\mathrm{q}}$	977.8	2.4 %	< 0.1 %	70
$\mathrm{e}^+\mathrm{e}^- \to \nu\bar{\nu}\ell^+\ell^-\gamma$	9.6	2.8 %	0.2 %	29
$\mathrm{e}^+\mathrm{e}^- \to \nu\bar{\nu}\ell^+\ell^-$	23.3	1.5 %	0.1 %	25
$^*\mathrm{e}^\pm\gamma \to \mathrm{e}^\pm\ell^+\ell^-$	1942.1	0.5 %	$\ll$ 0.1 %	16

Table 20: Signal efficiencies for the $\mathrm{H} \to \mathrm{Z}\gamma$ selection and the main background processes for the $\mathrm{q}\bar{\mathrm{q}}\gamma$ and $\ell^+\ell^-\gamma$ final states for an integrated luminosity of $1.5\,\mathrm{ab}^{-1}$. The expected numbers for the $\mathrm{e}^\pm\gamma$ processes account for the luminosity spectrum for beamstrahlung and quasi-real photons. Background processes contributing less than 10 events are not shown. The total numbers of background events in the $\mathrm{q}\bar{\mathrm{q}}\gamma$, $\mathrm{e}^+\mathrm{e}^-\gamma$ and $\mu^+\mu^-\gamma$ final states are 1072, 41 and 39 respectively.

6.7 $\mathrm{H} \to \mu^+\mu^-$

The measurement of the rare $\mathrm{H} \to \mu^+\mu^-$ decay is challenging due to the very low SM branching ratio, which is of order 2×10^{-4}. In the $\mathrm{e}^+\mathrm{e}^- \to \mathrm{H}\nu_\mathrm{e}\bar{\nu}_\mathrm{e}$ production, the signature for $\mathrm{H} \to \mu^+\mu^-$ decay is a $\mu^+\mu^-$ pair with invariant mass consistent with m_H and missing momentum. The efficient rejection of background relies on the excellent detector momentum resolution, which directly influences the width of the reconstructed di-muon invariant mass peak. Signal and background events were simulated at $\sqrt{s} = 1.4\,\mathrm{TeV}$ and $3\,\mathrm{TeV}$ using the CLIC_ILD and CLIC_SiD detector models respectively. An electron beam polarisation of $-80\,\%$ was assumed. Both analyses were performed independently. They follow the same strategy but differ in some of the observables that are used in the event selection.

The final state of interest are two muons plus missing energy from the neutrinos. The most important background processes are those that include $\mu^+\mu^-\nu\bar{\nu}$ in the final state, as shown in Table 21 for 1.4 TeV and in Table 22 for 3 TeV. A significant fraction of these kind of events are also produced from interactions involving beamstrahlung photons. Another important background is $\mathrm{e}^+\mathrm{e}^- \to \mathrm{e}^+\mathrm{e}^-\mu^+\mu^-$, where both electrons are usually emitted at very low polar angles and thus might not be detected. Tagging of these low angle electrons in the very forward calorimeters—LumiCal and BeamCal—is essential to keep this background under control.

The event selection requires two reconstructed, oppositely charged muons with a di-muon invariant mass within the relevant mass region of 105 – 145 GeV. Events with one or more detected high-energy electrons ($E > 200$ GeV at 1.4 TeV, $E > 250$ GeV at 3 TeV) in the very forward calorimeters are vetoed. This introduces the possibility to veto signal events if they coincide with Bhabha scattering events. The $e^+e^- \to e^+e^-$ cross section is sufficiently high that the probability of such a coincidence within 20 bunch crossings (10 ns) is about 7% in both analyses. The cuts on the minimum energy and the minimum polar angle for vetoing forward electrons need to be chosen carefully. $e^+e^- \to e^+e^-$ events need to be rejected efficiently while a low probability for coincidence with Bhabha scattering events needs to be maintained.

The 3 TeV analysis includes some additional preselection cuts to remove phase space regions that do not include any signal events. These cuts are a maximum energy of 100 GeV for any reconstructed non-muon object and a maximum energy of 20 GeV for reconstructed electrons in the central parts of the detector. The sum of the transverse momenta of the two muons, $p_T(\mu^-)+p_T(\mu^+)$, is required to be above 50 GeV and the transverse momentum of the di-muon system should be above 25 GeV.

The final event selection uses a BDT classifier using various kinematic variables excluding the invariant mass of the di-muon system. The 1.4 TeV analysis uses visible energy of the event after removal of the di-muon system E_{vis}, transverse momentum of the di-muon system $p_T(\mu\mu)$, sum of the transverse momenta of the two muons $p_T(\mu^-)+p_T(\mu^+)$, the polar angle of the di-muon system $\theta_{\mu\mu}$, the boost of the di-muon system, $\beta_{\mu\mu}$, and the cosine of the helicity angle $\cos\theta^*$. The 3 TeV analysis uses the energy of the hardest non-muon object instead of the total visible energy and also includes the energy, transverse momentum, polar angle and azimuthal angle of both individual muons. This event selection reduces background from four-fermion processes by several orders of magnitude, whilst maintaining an overall signal selection efficiency of $\varepsilon = 30.5\%$ and $\varepsilon = 26.3\%$ at 1.4 TeV and 3 TeV respectively.

The number of signal events is extracted from the reconstructed invariant mass distribution after the event selection, as shown in Figure 18. Using a large MC sample, the signal and background shapes are extracted. The signal can for example be described by a Gaussian distribution with asymmetric exponential tails. The combined background is parameterised as the sum of an exponential and a constant function. To assess the expected statistical precision, a large number of trial samples are generated from the expected signal and background reconstructed mass distributions and then fitted to signal and background components. The expected relative uncertainty on the $\sigma(e^+e^- \to H\nu_e\bar{\nu}_e) \times BR(H \to \mu^+\mu^-)$ is 26.6%, corresponding to a significance of 3.7, at 1.4 TeV, and 19.2%, corresponding to a significance of 5.2, at 3 TeV

Process	σ/fb	ε_{presel}	ε_{BDT}	N_{BDT}
$e^+e^- \to H\nu_e\bar{\nu}_e; H \to \mu^+\mu^-$	0.094	82.5 %	30.5 %	43
$e^+e^- \to \nu_e\bar{\nu}_e\mu^+\mu^-$	232	1.1 %	0.30 %	1030
$e^\pm\gamma \to e^\pm\nu_\mu\bar{\nu}_\mu\mu^+\mu^-$	35	8.5 %	0.11 %	57
$\gamma\gamma \to \nu_\mu\bar{\nu}_\mu\mu^+\mu^-$	162	10.6 %	0.23 %	560

Table 21: List of the main backgrounds in the $H \to \mu^+\mu^-$ analysis at $\sqrt{s} = 1.4$ TeV with the corresponding cross sections. Other processes, including $e^+e^- \to \mu^+\mu^-$ and $e^\pm\gamma \to e^\pm\mu^+\mu^-$, contribute a total of less than 10 events to the final selection.

Process	σ/fb	ε_{presel}	ε_{BDT}	N_{BDT}
$e^+e^- \to H\nu_e\bar{\nu}_e; H \to \mu^+\mu^-$	0.16	64%	26%	84
$e^+e^- \to \nu_e\bar{\nu}_e\mu^+\mu^-$	6.6	33%	14%	1797
$e^\pm\gamma \to e^\pm\mu^+\mu^-$	1210	6.9%	0.011%	262
$\gamma\gamma \to \nu_\mu\bar{\nu}_\mu\mu^+\mu^-$	413	4.3%	0.021%	176

Table 22: List of the most important background processes in the $H \to \mu^+\mu^-$ analysis at $\sqrt{s} = 3$ TeV with the corresponding cross sections. All other processes contribute of the order of 10 events to the final event selection. The cross sections are calculated for events with invariant mass of the di-muon system between 100 GeV and 140 GeV.

7 ZZ-fusion

Higgs boson production through the t-channel fusion of two Z bosons, $e^+e^- \to He^+e^-$, is analogous to the WW-fusion process but gives access to complementary Higgs boson couplings. At $\sqrt{s} = 1.4$ TeV, ZZ-fusion is the sub-leading Higgs production process, with a cross section of around 25 fb, which is 10 % of that for the WW-fusion process. The physics potential of the ZZ-fusion process has been investigated at $\sqrt{s} = 1.4$ TeV using the CLIC_ILD detector.

The characteristic signature of the ZZ-fusion process is two scattered beam electrons reconstructed in the forward regions of the detector, plus the Higgs boson decay products. Here, the scattered beam electrons are required to be fully reconstructed, and the final state $H \to b\bar{b}$ is considered.

Events are clustered into a four-jet topology using a k_T exclusive clustering algorithm with $R = 1.0$. For a well-reconstructed signal event, two of the resulting 'jets' are expected to be the reconstructed electrons, and the remaining two jets from the Higgs decay to $b\bar{b}$. The event selection requires two

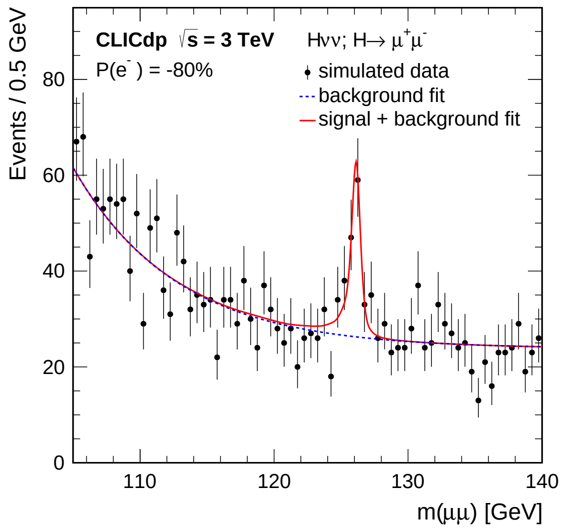

Fig. 18: Reconstructed di-muon invariant mass distribution after the event selection in the analysis of the $\mathrm{H} \to \mu^+\mu^-$ decay, for an integrated luminosity of $2\,\mathrm{ab}^{-1}$ at $\sqrt{s} = 3\,\mathrm{TeV}$, assuming 80% electron polarisation.

oppositely-charged electron candidates, separated by $|\Delta\eta| > 1$, each with $E > 100\,\mathrm{GeV}$. This preselection preserves 27 % of the $\mathrm{e^+e^-} \to \mathrm{He^+e^-} \to \mathrm{b\bar{b}e^+e^-}$ signal (3.6 fb), with the lost events almost entirely due to the scattered electrons falling outside the detector acceptance, as shown in Figure 19. After the preselection, the SM background consists mainly of events that have two real electrons and a $\mathrm{q\bar{q}}$ pair, either from the continuum or from the decay of Z bosons. Although the preselection suppresses 98 % of the $\mathrm{e^+e^-} \to \mathrm{q\bar{q}e^+e^-}$ background, the accepted cross section is 48 fb, which is thirteen times larger than that for the remaining signal. A further requirement that one of the two jets associated with the Higgs decay has a b-tag value > 0.4 preserves 80 % of the remaining signal and rejects 80 % of the remaining background.

A relative likelihood classifier $\mathscr{L}_1$, which treats ZZ-fusion events with $\mathrm{H} \to \mathrm{b\bar{b}}$ as signal and $\mathrm{H} \to \mathrm{WW}^*$ and $\mathrm{H} \to \mathrm{ZZ}^*$ as background, is used to reduce contributions from other Higgs decays. Seven variables are used to construct the likelihood: the jet clustering variable y_{45}; the invariant mass of the two jets associated with the Higgs decay; the visible mass of the event with the scattered beam electrons removed; the higher of the b-tag values of the two jets associated with the Higgs decay; the c-tag value corresponding to the same jet; and the b-c-separation returned by the tagger, for both Higgs decay jets. Requiring a high signal likelihood, $\mathscr{L}_1 > 0.8$, reduces the $\mathrm{H} \to \mathrm{b\bar{b}}$ signal to 2.0 fb but leaves only 0.06 fb of contributions from other Higgs decays, while also reducing the non-Higgs backgrounds to 3.1 fb.

Finally, to separate the signal from all backgrounds, a further relative likelihood classifier $\mathscr{L}_2$ is constructed using four variables that provide separation power between signal and background: the opening between the reconstructed electrons ΔR; the recoil mass of the event determined from the momenta of the reconstructed electrons, m_{rec}; the jet clustering variable y_{34}; and the invariant mass of the two jets associated with the Higgs decay.

The resulting likelihood is shown in shown in Figure 20 and gives good separation between signal and background. The likelihood distribution is fitted by signal and background components (where the normalisation is allowed to vary), giving

$$\Delta[\sigma(\mathrm{He^+e^-}) \times BR(\mathrm{H} \to \mathrm{b\bar{b}})] = 1.8\,\%$$

for $1.5\,\mathrm{ab}^{-1}$ at $\sqrt{s} = 1.4\,\mathrm{TeV}$.

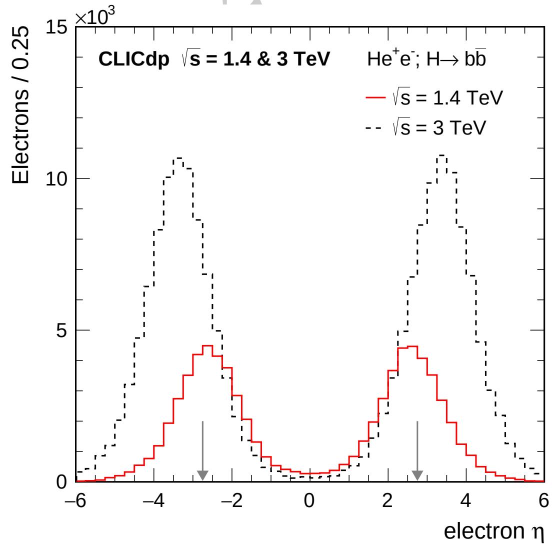

Fig. 19: Electron η for $\mathrm{e^+e^-} \to \mathrm{He^+e^-}$ events at $\sqrt{s} = 1.4\,\mathrm{TeV}$ and 3 TeV, for $1.5\,\mathrm{ab}^{-1}$ and $2\,\mathrm{ab}^{-1}$ of data, respectively. The vertical arrows show the detector acceptance.

8 Top Yukawa Coupling

At an $\mathrm{e^+e^-}$ collider the top Yukawa coupling, y_t, can be determined from the production rate in the process where a Higgs boson is produced in association with a top quark pair, $\mathrm{e^+e^-} \to \mathrm{t\bar{t}H}$. The top quarks decay almost exclusively by $\mathrm{t} \to \mathrm{bW}$. The signal event topology thus depends on the nature of the W and Higgs boson decays. Here $\mathrm{H} \to \mathrm{b\bar{b}}$ decays are studied for two $\mathrm{t\bar{t}H}$ decay channels:

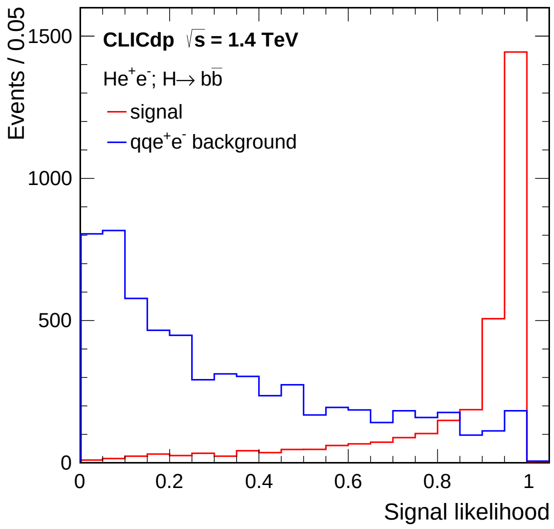

Fig. 20: Likelihood for $\mathrm{H} \to \mathrm{b\bar{b}}$ selection, normalised to $1.5\,\mathrm{ab}^{-1}$ of data.

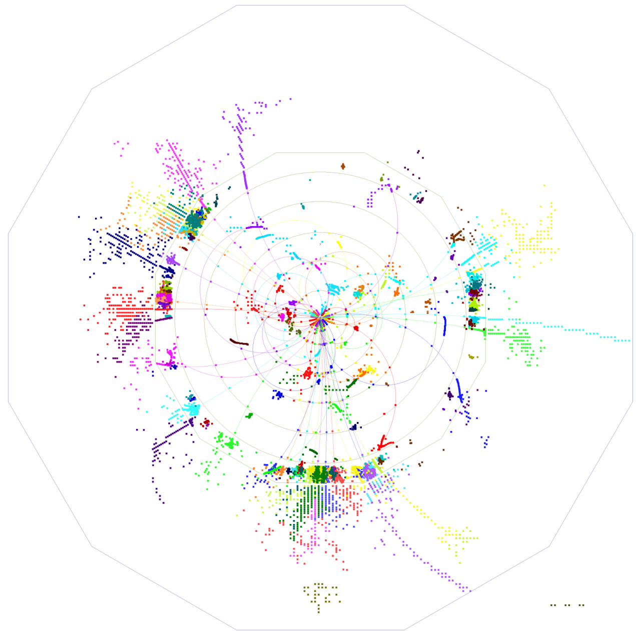

Fig. 21: A $\mathrm{t\bar{t}H} \to \mathrm{b\bar{b}b\bar{b}q\bar{q}}\tau^-\bar{\nu}_\tau$ event at $\sqrt{s} = 1.4\,\mathrm{TeV}$. The tau lepton decays hadronically.

– the fully-hadronic channel (where both W bosons decay hadronically), giving a $\mathrm{t\bar{t}H}$ final state of eight jets, including four b jets;
– the semi-leptonic channel (where one W boson decays leptonically), giving a $\mathrm{t\bar{t}H}$ final state of six jets (four b jets), one lepton and one neutrino,

The two channels are distinguished by first searching for isolated leptons (muons and electrons with an energy of at least 15 GeV and tau candidates from TauFinder containing a track with $p_\mathrm{T} > 10\,\mathrm{GeV}$). If zero leptons are found, the event is classified as fully-hadronic. If one lepton is found, the event is classified as semi-leptonic. Events in which more than one lepton are found are not analysed further. The k_t algorithm is used to cluster the particles of each event into a specific number of jets, with some particles being associated with the beam jets. Events classified as fully-hadronic are clustered into eight jets. In semi-leptonic events, the lepton is removed and the remaining particles are clustered into six jets. A semi-leptonic event is shown in Figure 21. The particles clustered into the beam jets are removed from the event and the particles included in the remaining six or eight jets are then re-clustered using the $\mathrm{e}^+\mathrm{e}^-$-Durham algorithm in LcfiPlus, which performs flavour-tagging for each jet, and prevents particles from displaced vertices being split between two or more jets. The jets are combined to form candidate primary particles in such a way so as to minimise a χ^2 function expressing the consistency of the reconstructed di- and tri-jet invariant masses with the $\mathrm{t\bar{t}}(\mathrm{H} \to \mathrm{b\bar{b}})$ hypothesis. For example, in the case of the semi-leptonic channel, the jet assignment with the minimum of

$$\chi^2 = \frac{(m_{12} - m_\mathrm{W})^2}{\sigma_\mathrm{W}^2} + \frac{(m_{123} - m_\mathrm{t})^2}{\sigma_\mathrm{t}^2} + \frac{(m_{45} - m_\mathrm{H})^2}{\sigma_\mathrm{H}^2},$$

gives the W, top and Higgs candidates.

Having forced each event into one of the two signal-like topologies, multivariate BDT classifiers (one for fully-hadronic events and one for semi-leptonic events) are used to separate signal and background. The discriminating variables include: kinematic quantities such as the reconstructed Higgs mass, the visible energy in the jets and the missing p_T; angular variables such as the angles between the Higgs decay products in the rest frame of the Higgs candidate with respect to its flight direction and the angle between the momenta of the top and Higgs candidates; event variables such as thrust, sphericity and the number of particles in the event; and flavour-tag variables for the four most likely b-jets. As an example, the BDT response distributions for the fully-hadronic channel are shown in Figure 22 The selection is chosen to maximise the signal significance. The expected numbers of selected events for $1.5\,\mathrm{ab}^{-1}$ of $\sqrt{s} = 1.4\,\mathrm{TeV}$ data are listed in Table 23. The $\mathrm{t\bar{t}H}$ cross section can be measured with an accuracy of 12.31 % in the semi-leptonic channel and 11.36 % in the hadronic channel. The combined precision of the two channels is 8.35 %.

To translate the measurement of the $\mathrm{t\bar{t}H}$ cross section into a measurement of the top Yukawa coupling, a correction is applied to take into account the other diagrams contributing to

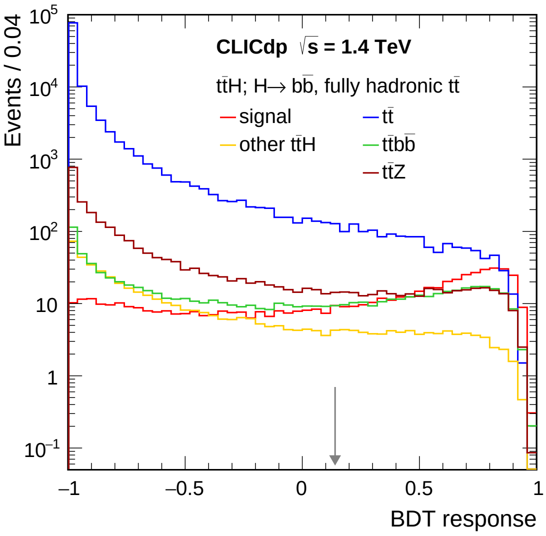

Fig. 22: BDT response distributions for the fully-hadronic channel, shown for the $t\bar{t}H$ signal and largest background processes. The value of the cut, which provides the highest significance, is indicated by the arrow.

Process	Events in $1.5\,ab^{-1}$	Selected as HAD	SL
$e^+e^- \to t\bar{t}H$, 6 jet, $H \to b\bar{b}$	647	357	9
$e^+e^- \to t\bar{t}H$, 4 jet, $H \to b\bar{b}$	623	62	233
$e^+e^- \to t\bar{t}H$, 2 jet, $H \to b\bar{b}$	150	1	20
$e^+e^- \to t\bar{t}H$, 6 jet, $H \not\to b\bar{b}$	473	38	8
$e^+e^- \to t\bar{t}H$, 4 jet, $H \not\to b\bar{b}$	455	5	19
$e^+e^- \to t\bar{t}H$, 2 jet, $H \not\to b\bar{b}$	110	0	1
$e^+e^- \to t\bar{t}b\bar{b}$, 6 jet	824	287	8
$e^+e^- \to t\bar{t}b\bar{b}$, 4 jet	794	44	175
$e^+e^- \to t\bar{t}b\bar{b}$, 2 jet	191	1	14
$e^+e^- \to t\bar{t}Z$, 6 jet	2,843	316	12
$e^+e^- \to t\bar{t}Z$, 4 jet	2,738	49	170
$e^+e^- \to t\bar{t}Z$, 2 jet	659	1	13
$e^+e^- \to t\bar{t}$	203,700	1,399	523
$e^+e^- \to qqqq\ell\nu$ (non-$t\bar{t}$)	68,300	11	70
$e^+e^- \to qqqq$	2.0×10^6	195	0

Table 23: Expected numbers of signal and background events in the fully-hadronic (HAD) and semi-leptonic (SL) channels for $1.5\,ab^{-1}$ at $\sqrt{s} = 1.4$ TeV. The columns show the total numbers of events before selection and the numbers of events passing the fully-hadronic and semi-leptonic BDT selections. The contributions from other investigated background processes were found to be negligible.

the $e^+e^- \to t\bar{t}H$ cross section, but which are not sensitive to the top Yukawa coupling, such as the case where the H boson is radiated off the intermediate Z boson in $e^+e^- \to t\bar{t}$. To evaluate the (relatively small) degradation in sensitivity, the WHIZARD program is used to calculate the cross section for the inclusive process $e^+e^- \to t\bar{t}H$ as a function of the value of the top Yukawa coupling. The factor required to translate the measured cross section uncertainty into a coupling uncertainty is determined from the slope of the cross section at the SM value of the top Yukawa coupling, and is found to be:

$$\frac{\Delta y_t}{y_t} = 0.53 \frac{\Delta \sigma}{\sigma}.$$

Thus, the expected precision on the top Yukawa coupling is

$$\frac{\Delta y_t}{y_t} = 4.43\,\%,$$

for $1.5\,ab^{-1}$ of data at $\sqrt{s} = 1.4$ TeV without beam polarisation. This value improves to better than 4.0 % for the same amount of data collected using the $P(e^-) = -80\,\%$ polarisation configuration. Since the cross section for the $t\bar{t}H$ cross section falls with increasing $\sqrt{s}$ (see Figure 2), the precision at 3 TeV is not expected to be better than the result presented here.

9 Double Higgs Production

In e^+e^- collisions at $\sqrt{s} > 1$ TeV, double Higgs production, $e^+e^- \to HH\nu_e\bar{\nu}_e$, can occur through the processes shown in Figure 23. Despite the small cross section (0.15 fb and 0.59 fb for CLIC operated at $\sqrt{s} = 1.4$ TeV and 3 TeV respectively), measurements of the double Higgs production rate can be used to place limits on the Higgs boson trilinear self-coupling parameter λ, that determines the shape of the fundamental Higgs potential. BSM physics scenarios can introduce deviations of λ from its SM value of up to tens of percent [44]. In addition, double Higgs production provides the potential to extract the quartic HHWW coupling, through the top right Feynman diagram of Figure 23.

The dominant signature for $e^+e^- \to HH\nu_e\bar{\nu}_e$ production occurs when both Higgs bosons decay to b quarks, resulting in an event signature of four b-jets and missing momentum. Consequently, events are first clustered into four jets using a jet size of $R = 0.7$, which was found to minimise the overlap between reconstructed vector bosons in the $e^+e^- \to q\bar{q}q\bar{q}\nu\bar{\nu}$ process. Having forced the event into the four-jet topology, Higgs boson candidates are formed by combining the reconstructed jets into two jet pairs. In each event there are three possible jet-pairings to Higgs bosons. The

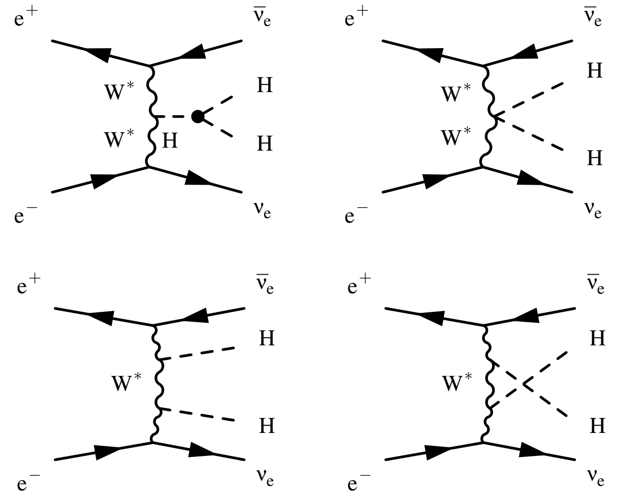

Fig. 23: Leading-order processes that produce two Higgs bosons and missing energy at a CLIC collider operating at $\sqrt{s} = 1.4\,\text{TeV}$ and $\sqrt{s} = 3\,\text{TeV}$. Only the top left diagram is sensitive to the trilinear Higgs self-coupling. The top right diagram is sensitive to the quartic coupling g_{HHWW}. All four diagrams are included in the generated $e^+e^- \to \text{HH}\nu_e\bar{\nu}_e$ signal samples.

most likely is selected by dividing the events into two hemispheres using the sign of the angle between the jet momentum vector and the event thrust axis. If exactly two jets are found in each hemisphere, the jets in the two hemispheres form the two Higgs candidates. Otherwise the pairing which minimises

$$\Delta^2 = (m_{ij} - m_{\text{H}})^2 + (m_{kl} - m_{\text{H}})^2, \quad (3)$$

is chosen, where m_{ij} is the invariant mass of ij^{th} jet pair.

Signal and background events are separated using a neural network technique that exploits different event features including: the jet flavour-tagging information; the number of isolated leptons (electrons, muons and taus); as well as kinematic distributions of the four jets and the two reconstructed Higgs bosons. All Higgs boson decays are considered as signal in the training of the neural network classifier. The optimal neural network cut results in signal efficiencies of XX % and YY % at $\sqrt{s} = 1.4\,\text{TeV}$ and $3\,\text{TeV}$ respectively. Table 24 lists the expected numbers of selected events from $e^+e^- \to \text{HH}\nu_e\bar{\nu}_e$ and the largest background processes.

The double Higgs production cross section is sensitive to the trilinear Higgs self-coupling λ. Since diagrams not involving λ also contribute to the $e^+e^- \to \text{HH}\nu_e\bar{\nu}_e$, their effect must be taken into account. The relation between the relative uncertainty on the cross section and the relative uncertainty of the Higgs trilinear coupling can be approximated as

$$\frac{\Delta\lambda}{\lambda} \approx \kappa \cdot \frac{\Delta\sigma_{\text{HH}\nu\bar{\nu}}}{\sigma_{\text{HH}\nu\bar{\nu}}}.$$

Process	# of selected events	
	$\sqrt{s} = 1.4\,\text{TeV}$	$\sqrt{s} = 3\,\text{TeV}$
$e^+e^- \to \text{HH}\nu_e\bar{\nu}_e$	X	Y
$e^+e^- \to$	X	Y

Table 24: Expected numbers of signal and background events passing the $e^+e^- \to \text{HH}\nu_e\bar{\nu}_e$ event selection for $1.5\,\text{ab}^{-1}$ at $\sqrt{s} = 1.4\,\text{TeV}$ and $2.0\,\text{ab}^{-1}$ at $\sqrt{s} = 3\,\text{TeV}$.

The value of κ can be determined from the WHIZARD generator by parameterising the $e^+e^- \to \text{HH}\nu_e\bar{\nu}_e$ cross section as a function of the input value for λ, as indicated in Figure 24. The fact that the slope is negative indicates that the main dependence on λ enters through interference with other SM diagrams. The value of κ is determined from the gradient of the cross section dependence as a function of λ, evaluated at its SM value, giving $\kappa = 1.22$ and $\kappa = 1.47$ at $1.4\,\text{TeV}$ and $3\,\text{TeV}$ respectively. However, this method does not account for the possibility that the event selection might preferentially favour some diagrams over others, and hence change the analysis sensitivity to λ.

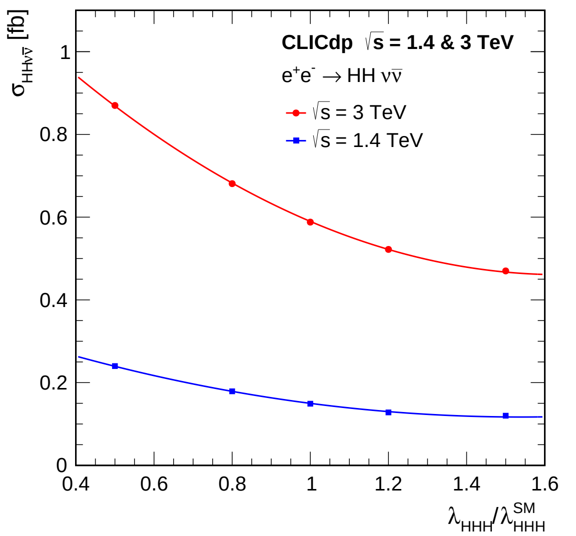

Fig. 24: Cross section for the $e^+e^- \to \text{HH}\nu_e\bar{\nu}_e$ process as a function of the ratio $\lambda/\lambda^{\text{SM}}$ at $\sqrt{s} = 1.4\,\text{TeV}$ and $\sqrt{s} = 3\,\text{TeV}$.

An alternative technique is to fit the output neural network distribution with a combination of templates from signal $e^+e^- \to \text{HH}\nu_e\bar{\nu}_e$ MC samples generated with various values of λ, in addition to the other SM background processes. This method has the advantage that it correctly accounts for the possibility that the event selection favours some diagrams over others. The template method is used to extract the experiment sensitivity to λ, while the cross section dependence described above is used as a cross check. In the case of zero beam polarisation, the template fit method gives

$$\Delta\lambda/\lambda = 32\,\% \text{ at } \sqrt{s} = 1.4\,\text{TeV},$$
$$\Delta\lambda/\lambda = 16\,\% \text{ at } \sqrt{s} = 3\,\text{TeV}.$$

Because the process involving the trilinear Higgs coupling involves t-channel WW-fusion, it can be enhanced by operating with polarised beams. For the case of $P(\mathrm{e}^+) = -80\,\%$:

$$\Delta\lambda/\lambda = 24\,\% \text{ at } \sqrt{s} = 1.4\,\text{TeV},$$
$$\Delta\lambda/\lambda = 12\,\% \text{ at } \sqrt{s} = 3\,\text{TeV}.$$

10 Higgs Mass

To be included.

11 Combined Fits

The results discussed in the preceding sections are summarised in Table 25 and Table 26. From the σ and $\sigma \times BR$ measurements given in the table the Higgs coupling parameters and total width are extracted by a global fit as described below. Here, a $-80\,\%$ electron polarisation is assumed for the 1.4 TeV and the 3 TeV stages. The increase in cross section is taken into account by multiplying the event rates with a factor of 1.8 (see Table 3), resulting in a reduction of the uncertainties by a factor of $\sqrt{1.8}$. This approach is conservative since it assumes that all backgrounds including those from s-channel processes,which do not receive the same enhancement by polarisation, scale with the same factor.

Since the physical observables (σ or $\sigma \times BR$) typically depend on several coupling parameters and on the total width, these parameters are extracted with a combined fit of all measurements. To provide a first indication of the overall impact of the CLIC physics programme, simple fits considering only the statistical uncertainties of the measurements are performed. Two types of fits are used: A *model-independent* fit making minimal theoretical assumptions, and a *model-dependent* fit following the strategies used for the interpretation of LHC Higgs results.

Both fits are based on a χ^2 minimisation using the MINUIT package [45]. The global χ^2 is constructed from the sum of individual χ^2 values for each independent measurement and its respective statistical uncertainty. These measurements, presented in detail in the preceding sections, are either a total cross section σ in the case of the measurement of $\mathrm{e^+e^-} \to \mathrm{ZH}$ via the recoil mass technique or cross section $\times$ branching ratio $\sigma \times BR$ for specific Higgs production modes and decays. To obtain the expected sensitivity for CLIC it is assumed that for all measurements the value expected in the SM has been measured, so only the statistical uncertainties of each measurement are used in the χ^2 calculation. The χ^2 for one individual measurement is then given by

$$\chi_i^2 = \frac{(C_i/C_i^{\mathrm{SM}} - 1)^2}{\Delta F_i^2}, \tag{4}$$

where C_i is fitted value of the relevant combination of relevant Higgs couplings (and total width) describing the particular measurement, C_i^{SM} is the SM expectation, and ΔF_i is the statistical uncertainty of the measurement of the considered process. The full χ^2 then is given by

$$\chi^2 = \sum_i \frac{(C_i/C_i^{\mathrm{SM}} - 1)^2}{\Delta F_i^2}. \tag{5}$$

The C_i's depend on the particular measurements and on the type of fit (model-independent or model-dependent), given in detail below. In addition, correlations between measurements are taken into account in cases where they are expected to be large. This applies to the measurements of $\sigma \times BR$ for $\mathrm{H} \to \mathrm{b\bar{b}}, \mathrm{c\bar{c}}, \mathrm{gg}$ in Higgsstrahlung and WW-fusion events, which are extracted in a combined fitting procedure.

11.1 Model-independent Fit

The model-independent fit makes minimal assumptions, such as the zero-width approximation (what does this mean?) to provide the description of the individual measurements in terms of Higgs couplings and of the total width, Γ_{H}. Here, the total cross section of $\mathrm{e^+e^-} \to \mathrm{ZH}$ depends on

$$C_{\mathrm{HZ}} = g_{\mathrm{HZZ}}^2, \tag{6}$$

while for specific final states such as $\mathrm{e^+e^-} \to \mathrm{ZH}, \mathrm{H} \to \mathrm{b\bar{b}}$ and $\mathrm{e^+e^-} \to \mathrm{H\nu_e\bar{\nu}_e}, \mathrm{H} \to \mathrm{b\bar{b}}$,

$$C_{\mathrm{ZH,H\to b\bar{b}}} = \frac{g_{\mathrm{HZZ}}^2 g_{\mathrm{Hbb}}^2}{\Gamma_{\mathrm{H}}} \tag{7}$$

and

$$C_{\mathrm{H\nu_e\bar{\nu}_e,H\to b\bar{b}}} = \frac{g_{\mathrm{HWW}}^2 g_{\mathrm{Hbb}}^2}{\Gamma_{\mathrm{H}}}, \tag{8}$$

respectively. The fit is performed with ten free parameters: g_{HZZ}, g_{HWW}, g_{Hbb}, g_{Hcc}, $g_{\mathrm{H\tau\tau}}$, $g_{\mathrm{H\mu\mu}}$, g_{Htt} and Γ_{H}, as well as the two effective couplings $g_{\mathrm{Hgg}}^\dagger$ and $g_{\mathrm{H\gamma\gamma}}^\dagger$. The latter two parameters are treated in the same way as the physical Higgs couplings in the fit.

Channel	Measurement	Observable	Statistical precision
			350 GeV 500 fb^{-1}
ZH	Recoil mass distribution	m_{H}	120 MeV
ZH	$\sigma(\mathrm{HZ}) \times BR(\mathrm{H} \to \text{invisible})$	Γ_{inv}	0.6 %
ZH	$\mathrm{H} \to \mathrm{b\bar{b}}$ mass distribution	m_{H}	tbd
ZH	$\sigma(\mathrm{HZ}) \times BR(\mathrm{Z} \to \ell^+\ell^-)$	g^2_{HZZ}	4.2 %
ZH	$\sigma(\mathrm{HZ}) \times BR(\mathrm{Z} \to \mathrm{q\bar{q}})$	g^2_{HZZ}	1.8 %
ZH	$\sigma(\mathrm{HZ}) \times BR(\mathrm{H} \to \mathrm{b\bar{b}})$	$g^2_{\mathrm{HZZ}} g^2_{\mathrm{Hbb}} / \Gamma_{\mathrm{H}}$	1 %†
ZH	$\sigma(\mathrm{HZ}) \times BR(\mathrm{H} \to \mathrm{c\bar{c}})$	$g^2_{\mathrm{HZZ}} g^2_{\mathrm{Hcc}} / \Gamma_{\mathrm{H}}$	5 %†
ZH	$\sigma(\mathrm{HZ}) \times BR(\mathrm{H} \to \mathrm{gg})$		6 %†
ZH	$\sigma(\mathrm{HZ}) \times BR(\mathrm{H} \to \tau^+\tau^-)$	$g^2_{\mathrm{HZZ}} g^2_{\mathrm{H\tau\tau}} / \Gamma_{\mathrm{H}}$	6.2 %
ZH	$\sigma(\mathrm{HZ}) \times BR(\mathrm{H} \to \mathrm{WW}^*)$	$g^2_{\mathrm{HZZ}} g^2_{\mathrm{HWW}} / \Gamma_{\mathrm{H}}$	2 %†
ZH	$\sigma(\mathrm{HZ}) \times BR(\mathrm{H} \to \mathrm{ZZ}^*)$	$g^2_{\mathrm{HZZ}} g^2_{\mathrm{HZZ}} / \Gamma_{\mathrm{H}}$	tbd
$\mathrm{H}\nu_e\bar{\nu}_e$	$\sigma(\mathrm{H}\nu_e\bar{\nu}_e) \times BR(\mathrm{H} \to \mathrm{b\bar{b}})$	$g^2_{\mathrm{HWW}} g^2_{\mathrm{Hbb}} / \Gamma_{\mathrm{H}}$	3 %†

Table 25: Summary of the precisions obtainable for the Higgs observables in the first stage of CLIC for an integrated luminosity of 500 fb^{-1} at $\sqrt{s} = 350\,\mathrm{GeV}$, assuming unpolarised beams. For the branching ratios, the measurement precision refers to the expected statistical uncertainty on the product of the relevant cross section and branching ratio; this is *equivalent* to the expected statistical uncertainty of the product of couplings divided by Γ_{H} as indicated in the third column. *Numbers reflect LCWS14 status*

Channel	Measurement	Observable	Statistical precision	
			1.4 TeV 1.5 ab^{-1}	3 TeV 2.0 ab^{-1}
$\mathrm{H}\nu_e\bar{\nu}_e$	$\mathrm{H} \to \mathrm{b\bar{b}}$ mass distribution	m_{H}	40 MeV*	33 MeV*
$\mathrm{H}\nu_e\bar{\nu}_e$	$\sigma(\mathrm{H}\nu_e\bar{\nu}_e) \times BR(\mathrm{H} \to \mathrm{b\bar{b}})$	$g^2_{\mathrm{HWW}} g^2_{\mathrm{Hbb}} / \Gamma_{\mathrm{H}}$	0.3 %	0.2 %
$\mathrm{H}\nu_e\bar{\nu}_e$	$\sigma(\mathrm{H}\nu_e\bar{\nu}_e) \times BR(\mathrm{H} \to \mathrm{c\bar{c}})$	$g^2_{\mathrm{HWW}} g^2_{\mathrm{Hcc}} / \Gamma_{\mathrm{H}}$	2.9 %	2.7 %
$\mathrm{H}\nu_e\bar{\nu}_e$	$\sigma(\mathrm{H}\nu_e\bar{\nu}_e) \times BR(\mathrm{H} \to \mathrm{gg})$		1.8 %	1.8 %
$\mathrm{H}\nu_e\bar{\nu}_e$	$\sigma(\mathrm{H}\nu_e\bar{\nu}_e) \times BR(\mathrm{H} \to \tau^+\tau^-)$	$g^2_{\mathrm{HWW}} g^2_{\mathrm{H\tau\tau}} / \Gamma_{\mathrm{H}}$	4.2 %*	tbd
$\mathrm{H}\nu_e\bar{\nu}_e$	$\sigma(\mathrm{H}\nu_e\bar{\nu}_e) \times BR(\mathrm{H} \to \mu^+\mu^-)$	$g^2_{\mathrm{HWW}} g^2_{\mathrm{H\mu\mu}} / \Gamma_{\mathrm{H}}$	38 %	16 %
$\mathrm{H}\nu_e\bar{\nu}_e$	$\sigma(\mathrm{H}\nu_e\bar{\nu}_e) \times BR(\mathrm{H} \to \gamma\gamma)$		15 %	tbd
$\mathrm{H}\nu_e\bar{\nu}_e$	$\sigma(\mathrm{H}\nu_e\bar{\nu}_e) \times BR(\mathrm{H} \to \mathrm{Z}\gamma)$		42 %	tbd
$\mathrm{H}\nu_e\bar{\nu}_e$	$\sigma(\mathrm{H}\nu_e\bar{\nu}_e) \times BR(\mathrm{H} \to \mathrm{WW}^*)$	$g^4_{\mathrm{HWW}} / \Gamma_{\mathrm{H}}$	1.4 %*	0.9 %*
$\mathrm{H}\nu_e\bar{\nu}_e$	$\sigma(\mathrm{H}\nu_e\bar{\nu}_e) \times BR(\mathrm{H} \to \mathrm{ZZ}^*)$	$g^2_{\mathrm{HWW}} g^2_{\mathrm{HZZ}} / \Gamma_{\mathrm{H}}$	3 %†	2 %†
$\mathrm{He}^+\mathrm{e}^-$	$\sigma(\mathrm{He}^+\mathrm{e}^-) \times BR(\mathrm{H} \to \mathrm{b\bar{b}})$	$g^2_{\mathrm{HZZ}} g^2_{\mathrm{Hbb}} / \Gamma_{\mathrm{H}}$	1 %†	0.7 %†
$\mathrm{t\bar{t}H}$	$\sigma(\mathrm{t\bar{t}H}) \times BR(\mathrm{H} \to \mathrm{b\bar{b}})$	$g^2_{\mathrm{Htt}} g^2_{\mathrm{Hbb}} / \Gamma_{\mathrm{H}}$	8 %	–
$\mathrm{HH}\nu_e\bar{\nu}_e$	$\sigma(\mathrm{HH}\nu_e\bar{\nu}_e)$	g_{HHWW}	7 %*	3 %*
$\mathrm{HH}\nu_e\bar{\nu}_e$	$\sigma(\mathrm{HH}\nu_e\bar{\nu}_e)$	λ	32 %	16 %
$\mathrm{HH}\nu_e\bar{\nu}_e$	with −80% e^- polarisation	λ	24 %	12 %

Table 26: Summary of the precisions obtainable for the Higgs observables in the higher-energy CLIC stages for integrated luminosities of 1.5 ab^{-1} at $\sqrt{s} = 1.4\,\mathrm{TeV}$, and 2.0 ab^{-1} at $\sqrt{s} = 3\,\mathrm{TeV}$. In both cases unpolarised beams have been assumed. The '–' indicates that a measurement is not possible or relevant at this centre-of-mass energy and 'tbd' indicates that no results or estimates are yet available. For the branching ratios, the measurement precision refers to the expected statistical uncertainty on the product of the relevant cross section and branching ratio; this is *equivalent* to the expected statistical uncertainty of the product of couplings divided by Γ_{H}, as indicated in the third column. For the measurements from the $\mathrm{t\bar{t}H}$ and $\mathrm{HH}\nu_e\bar{\nu}_e$ processes, the measurement precisions give the expected statistical uncertainties on the quantity or quantities listed under the observable heading. *Numbers reflect LCWS14 status*

Parameter	Relative precision		
	350 GeV 500 fb^{-1}	1.4 TeV + 1.5 ab^{-1}	3 TeV + 2 ab^{-1}
g_{HZZ}	0.8 %	0.8 %	0.8 %
g_{HWW}	1.8 %	0.9 %	0.9 %
g_{Hbb}	2.0 %	1.0 %	0.9 %
g_{Hcc}	3.2 %	1.4 %	1.1 %
$g_{H\tau\tau}$	3.7 %	1.7 %	1.5 %
$g_{H\mu\mu}$	–	14.1 %	5.6 %
g_{Htt}	–	4.1 %	$\leq$ 4.1 %
$g^{\dagger}_{Hgg}$	3.6 %	1.2 %	1.0 %
$g^{\dagger}_{H\gamma\gamma}$	–	5.7 %	< 5.7 %
Γ_H	5.0 %	3.6 %	3.4 %

Table 27: Results of the model-independent fit. Values marked "−" can not be measured with sufficient precision at the given energy, while values marked "< " have not yet been studied at the given energy, but should result in a considerable improvement of the precision. In the case of g_{Htt}, the 3 TeV case has not yet been studied, but is not expected to result in substantial improvement due to the significantly reduced cross section at high energy. The two effective couplings $g^{\dagger}_{Hgg}$ and $g^{\dagger}_{H\gamma\gamma}$ are also included in the fit. *Numbers reflect LCWS14 status*

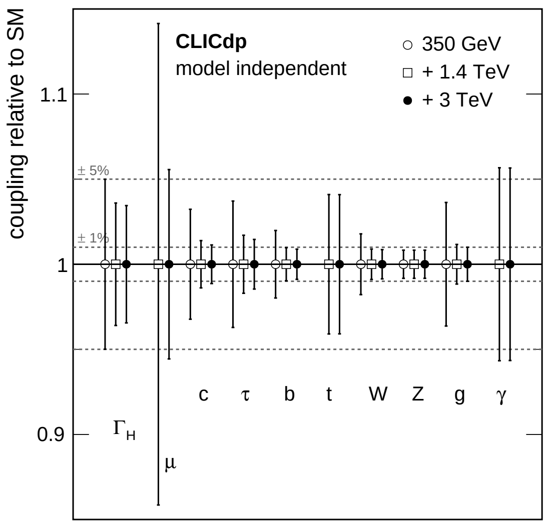

Fig. 25: Illustration of the precision of the Higgs couplings of the three-stage CLIC programme determined in model-independent fits. *Numbers reflect LCWS14 status*

The fit is performed in three stages, taking the statistical uncertainties obtainable from CLIC at the three considered energy stages (350 GeV, 1.4 TeV, 3 TeV) successively into account. Each new stage also includes all measurements of the previous stages. Table 27 summarises the results. They are graphically illustrated in Figure 25. Since the model-independence of the analysis hinges on the absolute measurement of $\sigma(HZ)$ at 350 GeV, which provides the coupling g_{HZZ}, the precision of all other couplings is ultimately limited by this uncertainty.

11.2 Model-dependent Fit

For the model-dependent fit, it is assumed that the Higgs decay properties can be described by nine independent parameters κ_{HZZ}, κ_{HWW}, κ_{Hbb}, κ_{Hcc}, $\kappa_{H\tau\tau}$, $\kappa_{H\mu\mu}$, κ_{Htt}, κ_{Hgg} and $\kappa_{H\gamma\gamma}$. These factors are defined by the ratio of the Higgs partial width divided by the partial width expected in the Standard Model as

$$\kappa_i^2 = \Gamma_i / \Gamma_i^{SM}. \tag{9}$$

In this scenario, the total width is given by the sum of the nine partial widths considered, which is equivalent to assuming no invisible Higgs decays. The variation of the total width from its SM value is thus given by

$$\Gamma_{H,md} = \sum_i \kappa_i^2 \, BR_i, \tag{10}$$

where BR_i is the SM branching fraction for the respective final state and the subscript "md" stands for "model-dependent". To obtain these branching fractions, a fixed value for the Higgs mass has to be imposed. For the purpose of this study, 126 GeV is assumed. The branching ratios are taken from the LHC Higgs cross section working group, ignoring theoretical uncertainties. To exclude effects from numerical rounding errors, the total sum of BR's is normalised to unity.

With these definitions, the C_i's in the χ^2 take the following forms: for the total $e^+e^- \to ZH$ cross section $e^+e^- \to ZH$,

$$C_{ZH} = \kappa^2_{HZZ}; \tag{11}$$

while for specific final states such as $e^+e^- \to ZH$, $H \to b\bar{b}$ and $e^+e^- \to H\nu_e\bar{\nu}_e$, $H \to b\bar{b}$,

$$C_{ZH,H\to b\bar{b}} = \frac{\kappa^2_{HZZ}\,\kappa^2_{Hbb}}{\Gamma_{H,md}} \tag{12}$$

and

$$C_{H\nu_e\bar{\nu}_e,H\to b\bar{b}} = \frac{\kappa^2_{HWW}\,\kappa^2_{Hbb}}{\Gamma_{H,md}}, \tag{13}$$

respectively.

Since at the first energy stage of CLIC no significant measurements of the $H \to \mu^+\mu^-$ and $H \to \gamma\gamma$ decays are possible, the fit is reduced to six free parameters (the coupling to top is also not constrained, but this is without effect on the total width) with an appropriate rescaling of the branching ratios used in the total width for 350 GeV.

Parameter	Relative precision		
	350 GeV 500 fb^{-1}	+ 1.4 TeV + 1.5 ab^{-1}	+ 3 TeV + 2 ab^{-1}
κ_{HZZ}	0.44 %	0.31 %	0.23 %
κ_{HWW}	1.5 %	0.17 %	0.11 %
κ_{Hbb}	1.7 %	0.37 %	0.22 %
κ_{Hcc}	3.1 %	1.1 %	0.75 %
$\kappa_{H\tau\tau}$	3.7 %	1.5 %	1.2 %
$\kappa_{H\mu\mu}$	–	14.1 %	5.5 %
κ_{Htt}	–	4.0 %	$\leq$ 4.0 %
κ_{Hgg}	3.6 %	0.79 %	0.55 %
$\kappa_{H\gamma\gamma}$	–	5.6 %	< 5.6 %
$\Gamma_{H,md,derived}$	1.6 %	0.32 %	0.22 %

Table 28: Results of the model-dependent fit. Values marked "–" can not be measured with sufficient precision at the given energy, while values marked "< " have not yet been studied at the given energy, but should result in a considerable improvement of the precision. In the case of g_{Htt}, the 3 TeV case has not yet been studied, but is not expected to result in substantial improvement due to the significantly reduced cross section at high energy. The uncertainty of the total width is calculated from the fit results following Equation 10, taking the parameter correlations into account. *Numbers reflect LCWS14 status*

As in the model-independent case the fit is performed in three stages, taking the statistical errors of CLIC at the three considered energy stages (350 GeV, 1.4 TeV, 3 TeV) successively into account. Each new stage also includes all measurements of the previous stages. The total width is not a free parameter of the fit. Instead, its uncertainty, based on the assumption given in Equation 10, is calculated from the fit results, taking the full correlation of all parameters into account. Table 28 summarises the results of the fit, and Figure 26 illustrates the evolution of the precision over the full CLIC programme.

11.3 Discussion of Fit Results

The full Higgs physics programme of CLIC, interpreted with a combined fit of the couplings to fermions and gauge bosons

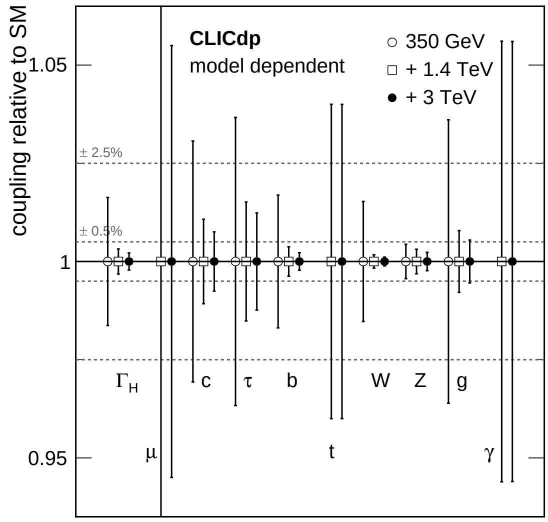

Fig. 26: Illustration of the precision of the Higgs couplings of the three-stage CLIC programme determined in a model-dependent fit, as discussed in the text. *Numbers reflect LCWS14 status*

as well as the total width, and combined with the measurement of the self-coupling, will provide a comprehensive picture of the properties of this newly discovered particle. Figure Figure 27 illustrates the expected uncertainties of the various couplings determined in the model-independent fit as well as the self-coupling as a function of the particle mass. Combined with the quasi model-independent measurement of the total width with a precision of 3.4 %, this illustrates the power of the three-stage CLIC programme. Each of the stages contributes significantly to the total precision, with the first stage at 350 GeV providing the model-independent "anchor" of the coupling to the Z boson as well as a first measurement of the total width and coupling measurements to most fermions and bosons. The higher-energy stages add direct measurements of the coupling to top quarks, to muons and photons as well as overall improvements of the branching ratio measurements and with that of the total widths and all couplings except the one to the Z already measured in the first stage. They also provide a measurement of the self-coupling of the Higgs boson. In a model-dependent analysis, the improvement with increasing energy is even more significant than in the model-independent fit, since the overall limit of all couplings imposed by the model-independent measurement of the ZH recoil process is removed.

12 Summary and Conclusions

A detailed study of the Higgs physics reach of CLIC has been presented in the context of CLIC operating in three en-

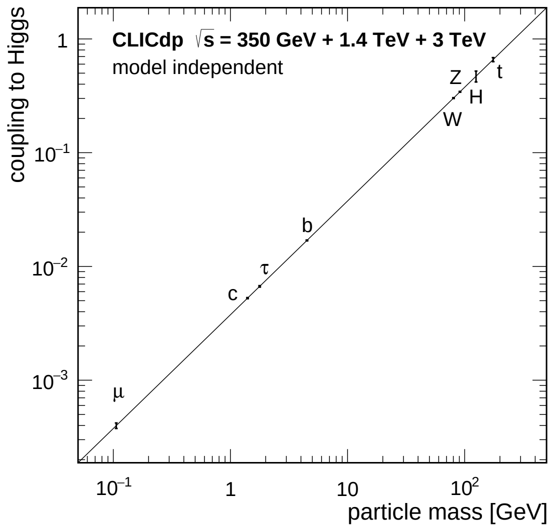

Fig. 27: Illustration of the precision of the model-independent Higgs couplings and of the self-coupling as a function of particle mass. *Numbers reflect LCWS14 status*

ergy stages, $\sqrt{s}$ = 350 GeV, 1.4 TeV and 3 TeV. The initial stage of operation, 500 fb^{-1} at $\sqrt{s} = 350$ GeV, would allow the study of Higgs production from both the $\mathrm{e^+e^- \to HZ}$ and the WW-fusion process. These data would yield precise *model-independent* measurements of the Higgs boson couplings, for example $\Delta(g_{\mathrm{HZZ}}) = \pm 0.8\,\%$, $\Delta(g_{\mathrm{HWW}}) = \pm X\,\%$ and $\Delta(g_{\mathrm{Hbb}}) = \pm Y\,\%$. In addition the branching ratio to invisible decay modes would be constrained to $\Gamma_{\mathrm{invis}}/\Gamma_{\mathrm{H}} < Z$ at 90 % C.L. and the total Higgs width would be measured to $\Delta(\Gamma_{\mathrm{H}}) = \pm X\,\%$. Operation of CLIC at $\sqrt{s} > 1$ TeV provides high-statistics samples of Higgs bosons produced through the WW-fusion process and gives access to rarer processes such as $\mathrm{e^+e^- \to t\bar{t}H}$ and $\mathrm{e^+e^- \to HH\nu_e\bar{\nu}_e}$. Studies of these rare processes would provide measurements of the top Yukawa coupling to ±4.5 % and the Higgs boson self-coupling to ±20 %. Furthermore the full data sample leads to very tight constraints on the Higgs couplings to vector bosons and fermions. For example, in a model-independent treatment, the majority of the accessible couplings are measured to better than X %, and the model-dependent κ parameters are determined with a precision of between 0.1 % – 1 %.

Acknowledgements The authors would like to acknowledge the use of the Oxford Particle Physics Computing Cluster. This work was (partially) supported by: the Comisión Nacional de Investigación Científica y Tecnológica (CONICYT), Chile; the Ministry of Education, Youth and Sports, Czech Republic, under Grant INGO II-LG 14033; the DFG cluster of excellence 'Origin and Structure of the Universe', Germany; the EU AIDA grant; the German - Israel Foundation (GIF); the Israel Science Foundation (ISF); the I-CORE Program, Israel; the Ministry of Education, Science and Technological Development of the Republic of Serbia through the project OI171012; the Secretary of State of Research, Development and Innovation of Spain, under project FPA2011-15330-E; the Gates Foundation, United Kingdom; the STFC, United Kingdom; and the U. S. Department of Energy, Office of Science, Office of Basic Energy Sciences and Office of High Energy Physics under contract DE-AC02-06CH11357.

References

1. A. Collaboration, Phys. Lett. **B716**, 1 (2012)
2. C. Collaboration, Phys. Lett. **B716**, 30 (2012)
3. F. Englert, R. Brout, Phys. Rev. Lett. **13**, 321 (1964)
4. P. Higgs, Phys. Lett. **12**, 132 (1964)
5. P. Higgs, Phys. Rev. Lett. **13**, 508 (1964)
6. G. Guralnik, C. Hagen, T. Kibble, Phys. Rev. Lett. **13**, 585 (1964)
7. P. Higgs, Phys. Rev. **155**, 1156 (1966)
8. T. Kibble, Phys. Rev., volume=
9. M. Aicheler, P. Burrows, M. Draper, T. Garvey, P. Lebrun, K. Peach, N. Phinney, H. Schmickler, D. Schulte, N. Toge (eds.), *A Multi-TeV Linear Collider based on CLIC Technology: CLIC Conceptual Design Report* (CERN). CERN-2012-007, JAI-2012-001, KEK Report 2012-1, PSI-12-01, SLAC-R-985
10. H. Aihara, P. Burrows, Oreglia (eds.), *SiD Letter of Intent* (2009). SLAC-R-989, FERMILAB-LOI-2009-01, FERMILAB-PUB-09-681-E, arXiv:0911.0006
11. T. Behnke, J.E. Brau, P.N. Burrows, J. Fuster, M. Peskin, et al. (eds.), *The International Linear Collider Technical Design Report - Volume 4: Detectors* (2013). ILC-REPORT-2013-040, ANL-HEP-TR-13-20, BNL-100603-2013-IR, IRFU-13-59, CERN-ATS-2013-037, Cockcroft-13-10, CLNS 13/2085, DESY 13-062, FERMILAB TM-2554, IHEP-AC-ILC-2013-001, INFN-13-04/LNF, JAI-2013-001, JINR E9-2013-35, JLAB-R-2013-01, KEK Report 2013-1, KNU/CHEP-ILC-2013-1, LLNL-TR-635539, SLAC-R-1004, ILC-HiGrade-Report-2013-003, arXiv:1306.6329
12. T. Abe, et al., *The International Large Detector: Letter of Intent* (2010). DESY 2009-87, Fermilab-Pub-09-682-E, KEK Report 2009-6, arXiv:1006.3396
13. L. Linssen, A. Miyamoto, M. Stanitzki, H. Weerts (eds.), *Physics and Detectors at CLIC: CLIC Conceptual Design Report* (2012). DOI 10.5170/CERN-2012-003. CERN-2012-003, ANL-HEP-TR-12-01, DESY-12-008, KEK-Report-2011-7, arXiv:1202.5940
14. M. Thomson, Nucl. Instrum. Meth. **A611**, 25 (2009). DOI 10.1016/j.nima.2009.09.009
15. J. Marshall, A. Münnich, M. Thomson, Nucl.Instrum.Meth. **A700**, 153 (2013). DOI 10.1016/j.nima.2012.10.038

16. S. Dittmaier, C. Mariotti, G. Passarino, R. Tanaka, et al., (2012). DOI 10.5170/CERN-2012-002. CERN-2012-002, arXiv:1201.3084
17. S. Dawson, A. Gritsan, H. Logan, J. Quian, C. Tully, R. van Kooten, (2013). arXiv:1310.8361
18. H. Baer, T. Barklow, K. Fujii, Y. Gao, A. Hoang, et al. (eds.), *The International Linear Collider Technical Design Report - Volume 2: Physics* (2013). ILC-REPORT-2013-040; ANL-HEP-TR-13-20; BNL-100603-2013-IR; IRFU-13-59; CERN-ATS-2013-037; Cockcroft-13-10; CLNS 13/2085; DESY 13-062; FERMILAB TM-2554; IHEP-AC-ILC-2013-001; INFN-13-04/LNF; JAI-2013-001; JINR E9-2013-35; JLAB-R-2013-01; KEK Report 2013-1; KNU/CHEP-ILC-2013-1; LLNL-TR-635539; SLAC-R-1004; ILC-HiGrade-Report-2013-003, arXiv:1306.6352
19. S. Agostinelli, et al., Nucl.Instrum.Meth. **A506**, 250 (2003). DOI 10.1016/S0168-9002(03)01368-8
20. J. Allison, K. Amako, J. Apostolakis, H. Araujo, P. Dubois, et al., IEEE Trans.Nucl.Sci. **53**, 270 (2006). DOI 10.1109/TNS.2006.869826
21. W. Kilian, T. Ohl, J. Reuter, Eur.Phys.J. **C71**, 1742 (2011). DOI 10.1140/epjc/s10052-011-1742-y
22. T. Sjostrand, S. Mrenna, P.Z. Skands, JHEP **0605**, 026 (2006). DOI 10.1088/1126-6708/2006/05/026
23. Z. Was, Nucl.Phys.Proc.Suppl. **98**, 96 (2001). DOI 10.1016/S0920-5632(01)01200-2
24. K. Fujii. Physics study libraries. URL http://www-jlc.kek.jp/subg/offl/physsim/
25. P. Mora de Freitas, H. Videau, in *International Workshop on Linear Colliders (LCWS 2002)* (JeJu Island, Korea, 2002), pp. 623–627
26. N. Graf, J. McCormick, AIP Conf.Proc. **867**, 503 (2006). DOI 10.1063/1.2396991
27. F. Gaede, Nucl.Instrum.Meth. **A559**, 177 (2006). DOI 10.1016/j.nima.2005.11.138
28. N.A. Graf, J.Phys.Conf.Ser. **331**, 032012 (2011). DOI 10.1088/1742-6596/331/3/032012
29. J. Marshall, M. Thomson, J.Phys.Conf.Ser. **396**, 022034 (2012). DOI 10.1088/1742-6596/396/2/022034
30. J. Marshall, M. Thomson, in *Proceedings of CHEF2013 - Calorimetry for the High Energy Frontier* (Paris, France, 2013), pp. 305–315. arXiv:1308.4537
31. T. Suehara, T. Tanabe, S. Yamashita, (2011). arXiv:1110.5785 Is this the correct reference?
32. P. Schade, A. Lucaci-Timoce. Description of the signal and background event mixing as implemented in the Marlin processor OverlayTiming (2011). CERN LCD-Note-2011-006
33. M. Cacciari, G.P. Salam, G. Soyez, (2011). arXiv:1111.6097
34. C. Grefe, S. Poss, A. Sailer, A. Tsaregorodtsev, J. Phys.: Conf. Series **513**, 032077 (2014). DOI doi:10.1088/1742-6596/513/3/032077
35. J. Therhaag, AIP Conf.Proc. **1504**, 1013 (2009). DOI 10.1063/1.4771869
36. K.S. Cranmer, Comput.Phys.Commun. **136**, 198 (2001). DOI 10.1016/S0010-4655(00)00243-5
37. K.S. Cranmer, (1999). ALEPH Note 99-144
38. The OPAL Collaboration, (2000). OPAL Physics Note PN426
39. A.L. Read, in *1st Workshop on confidence limits* (CERN, Geneva, Switzerland, 2000), p. 81. DOI 10.5170/CERN-2000-005.81. CERN-OPEN-2000-205
40. A. Münnich. TauFinder: A Reconstruction Algorithm for tau Leptons at Linear Colliders (2010). LCD-Note-2010-009
41. D. Bailey, et al., Nuclear Instruments and Methods in Physics Research A **610**, 573 (2009). DOI 10.1016/j.nima.2009.08.059
42. S. Chatrchyan, et al., Phys.Lett. **B716**, 30 (2012). DOI 10.1016/j.physletb.2012.08.021
43. G. Aad, et al., Phys.Lett. **B716**, 1 (2012). DOI 10.1016/j.physletb.2012.08.020
44. R.S. Gupta, H. Rzehak, J.D. Wells, Phys.Rev. **D88**, 055024 (2013). DOI 10.1103/PhysRevD.88.055024
45. F. James, M. Roos, Computer Physics Communications **10**(6), 343 (1975). DOI http://dx.doi.org/10.1016/0010-4655(75)90039-9. URL http://www.sciencedirect.com/science/article/pii/0010465575900399